Resilient Tall Timber Building Design: Damped-Outrigger System

PRINCIPAL INVESTIGATOR

Dr. Solomon Tesfamariam, P.Eng.

(Professor, UBC Okanagan Campus)

HQP

Sourav Das

(PhD Student, UBC Okanagan Campus)

December 2021

THE UNIVERSITY OF BRITISH COLUMBIA

FACULTY OF APPLIED SCIENCE, SCHOOL OF ENGINEERING

Prepared for

Forestry Innovation Investment Ltd.
1200 - 1130 West Pender Street, Vancouver, BC Canada V6E 4A4

by

Dr. Solomon Tesfamariam

School of Engineering

The University of British Columbia, Okanagan Campus, BC, Canada

3333 University Way, Kelowna, BC Canada V1V 1V7

Disclaimers

This report includes a design for timber structure consisting CLT walls, glulam columns and glulam beams. The timber structure with damped outrigger system is proposed in this report. Shape memory alloy spring is utilized for enhanced dissipation capacity during seismic event. Other ways of conducting the seismic analysis and design are possible, and they may result in different demands on the building. The report has no intention of promoting or endorsing any particular proprietary connection or building system.

The authors have taken reasonable actions and due diligence to ensure the accuracy of the information provided in this report; however, THE AUTHORS, UNIVERSITY OF BRITISH COLUMBIA, OR OTHER CONTRIBUTORS ASSUME NO LIABILITY FOR ANY DIRECT OR INDIRECT DAMAGE, INJURY, LOSS OR EXPENSE THAT MAY BE INCURRED OR SUFFERED AS A RESULT OF THE USE OF THIS REPORT INCLUDING WITHOUT LIMITATION PRODUCTS, BUILDING TECHNIQUES OR PRACTICES. The authors do not guarantee the completeness of the information published in this report. Users of this report agree to use the information in this report (analysis suggestions, design procedures, detailing, etc.) at their own risk. We will not be liable for any errors, inaccuracies, omissions or damages arising from the use of the information presented in this report, nor any action taken in reliance to the presented information. Building science, products and construction practices change and improve over time and rather than relying on this report, it is advisable to: (a) regularly consult up-to-date technical publications on products and practices, (b) seek specific information and professional advice on the use of products mentioned in this report from manufacturers or suppliers of the products and consultants with appropriate qualifications and experience, and (c) review and comply with the specific requirements of the applicable building codes for each construction project.

Acknowledgements

Development of the design guideline in this project was supported through the BC Forestry Innovation Investment's (FII) Wood First Program. The financial support through NSERC Alliance is acknowledged. Under the supervision of Dr. Tesfamariam, one student has contributed to the knowledge presented in this report:

- Sourav Das (Dr. Tesfamariam's PhD student) was actively involved in the design under gravity load, modelling, simulation of shape memory alloy-based damped outrigger for tall timber building and final report writing.

Contents

List of Figures

List of Tables

List of Algorithms

Chapter 1

Introduction

With the introduction of mass timber, such as cross laminated timber (CLT) and glulam timber, tall timber buildings have become a viable option (Boellaard, 2012; Popovski and Gavric, 2016; Ramage et al., 2017; Tesfamariam et al., 2015, 2019). However, with increase in height, slenderness increases, which leads vulnerability to wind and earthquake loads (Tesfamariam et al., 2019; Bezabeh et al., 2021a; 2021b). To mitigate this, different lateral load resisting systems are considered, e.g. shear wall system (e.g. Tesfamariam et al. 2021a), frame system and combination of shear wall - frame system (Fig. 1.1). The lateral load resisting systems for buildings are selected based on the intended functionality, architectural consideration, height of the structure, aspect ratio, intensity of the loading, etc. (Taranath, 2016). In this report, outrigger systems (Fig. 1.2), as a viable solution are presented.

Under lateral dynamic loads, the outrigger systems reduce structural deformation and enhance resistance of tall buildings (Smith and Salim, 1981). In this systems, outrigger beams are connected with columns and shear core. When the structure deforms under lateral loads, the combined system of column and outrigger beam resist rotation of the shear core (Smith and Coull, 1991; Taranath, 2016). This results in reduction of lateral deflection and moments at the base of the shear core. In addition, the axial force induced on the columns connected with outrigger beams, contribute to the moment resistance by increasing effective depth of the system.

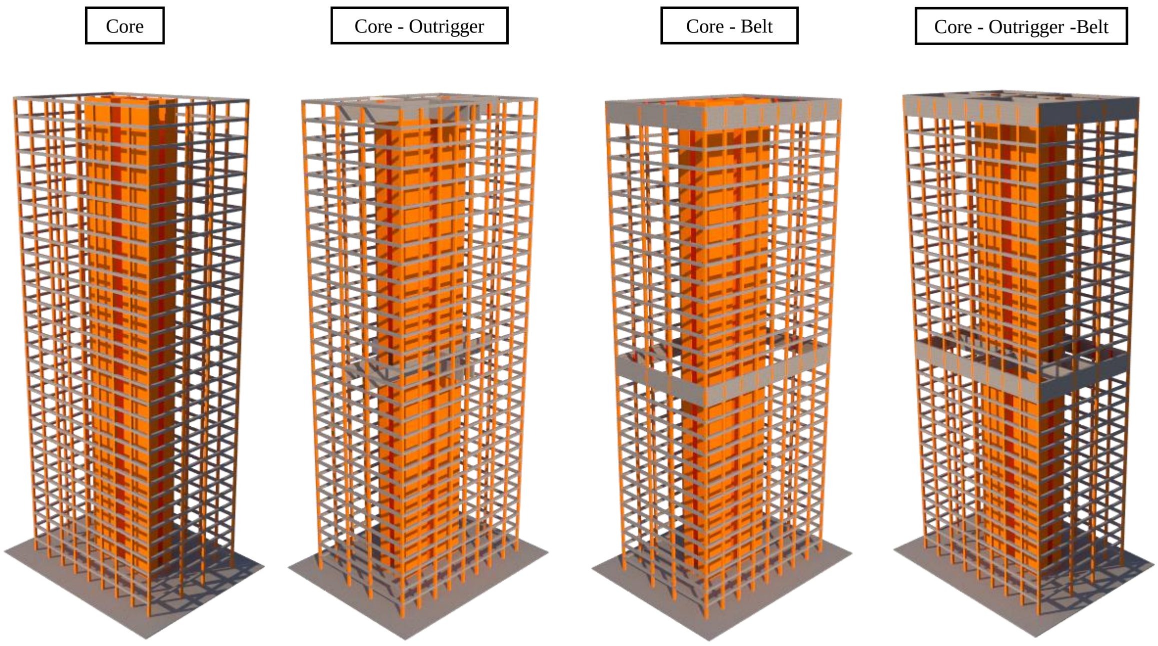

Figure 1.1: Core - outrigger system

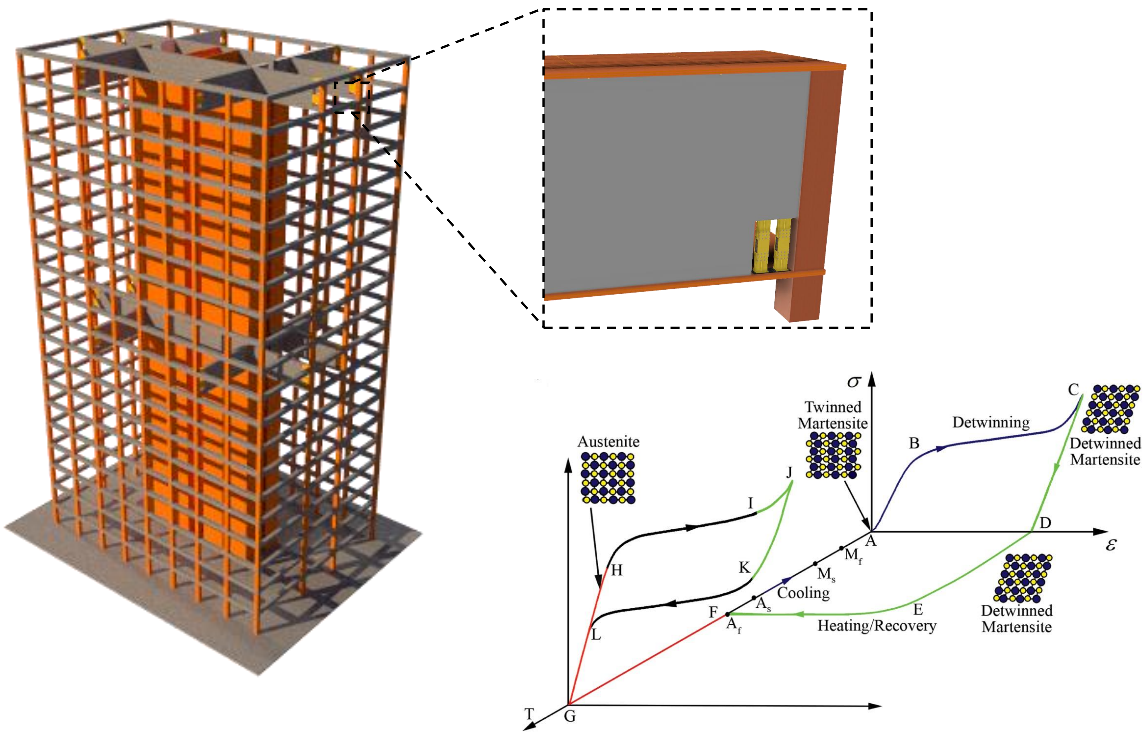

Figure 1.2: Shape memory alloy damper based damped outrigger system

1.1 Motivation, Aim & Research Questions

Wood has become a viable alternative of construction materials in terms of embodied energy and greenhouse gas emission (Werner and Richter, 2007). In this context, the use of mass-timber, such as cross-laminated timber (CLT) and glulam, for the multi-storey building has gained popularity in US and Canada. In general, CLT is a lightweight material, made by gluing the timber panels in alternative directions. Due to this, CLT is used for carrying the gravity loads and lateral load resisting system for the timber building. National Building Code of Canada (NBC, 2015) provided the design guidelines for the up to six-storey light timber building. The NBC 2020 code will increase this limit of CLT building to 12 storeys. With alternate design procedures, the industry has exceeded the 12-storey building limit and high rise buildings are constructed. Finding safe and efficient high-rise timber structural system is an active research area. With this in view, the present study aims to study the performance of timber outrigger structure for mitigating seismic induced vibrations. This system can also be extended to wind load. The objectives are set for the present study as follows-

- Compute the member sizes (i.e. beam, column and core of the structure) under the gravity loads. Beam and column are designed as Glulam and the same for core as CLT panel.

- Develop the theoretical solution of optimal location undamped outrigger for uniform and triangular distributed loads.

- Develop mathematical model for shape memory alloy (SMA)-based damped outrigger for high-rise timber structure using energy-based formulation. The nonlinear spring made of SMA is installed at the junction of outrigger and the column. The idea behind this is to exploit the high strength and re-centering capabilities offered by SMA that improves the energy dissipation of the damped outrigger by producing flag-shaped hysteresis.

- Study the performance of the proposed control strategy for one- and two-outriggers system. Multi-objective meta-heuristic methods are utilized to estimate the Pareto optimal solution by considering two objective functions i.e. maximum floor acceleration and maximum inter-storey drift ratio. Non-dominated sorting genetic algorithm II optimization algorithm is employed to find the optimal location of the outriggers and tuning parameters of SMA.

- Study the performance of the proposed control strategy and carry out a sensitivity analysis to demonstrate the performance envelope for different scenario.

1.2 Organization of Report

This report is presented in a number of chapters. The chapters along with their content are divided as follows

- **Chapter 1** contains introduction of the problem followed by literature review, the motivation, aim & research questions of the problem and organization of the report.
- **Chapter 2** contains a brief description of the vibration control strategies used for the mitigation of dynamic load-induced vibration of the buildings. This chapter also includes the brief description on the recently developed dampers.
- **Chapter 3** contains the details of the gravity load design for the timber buildings.
- **Chapter 4** contains the literature review on damped outrigger systems. In this chapter, the theoretical solution for optimal position of undamped outriggers under uniform and triangular distributed loads are described.
- **Chapter 5** contains the Lagrangian formulation of the outrigger structure.
- **Chapter 6** contains a brief description of multi-objective optimization. The details of meta-heuristic method such as NSGA-II is also presented.
- **Chapter 7** contains the numerical demonstration of the proposed control strategy. It also includes the performance of different configuration of outrigger structure.
- **Chapter 8** concludes the report. The report finally ends with Future works where areas of possible research and investigation is identified.

Chapter 2

Review on Dampers

Over the last few decades, vibration control of high-rise buildings becomes essential due to the slenderness of the structures. As the height of the structures increase, they are more prone to vibrate under dynamic lateral forces such as wind, earthquake, etc. To mitigate these unwanted vibrations, different vibration control strategies are adopted. The damping strategies are mainly classified as conventional systems, seismic isolation systems, and supplemental damping systems.

The conventional systems are designed based on the ductility of structures. In this design procedure, structures are designed in such a way that some members of the structure are allowed to yield and to show the inelastic deformation, while other members are designed as an elastic member. The ductility of the member can be achieved by allowing yielding in tension or inelastic bucking in braces or by providing flexural hinges in beams or at the base of the columns. Another popular method to resist the vibration of structure is the base-isolation technique. This technique is mainly used for reducing seismic-induced vibration. In this method, the isolators are installed in between the foundation and superstructure with the intention of minimal energy transmission to the superstructure. There are many base isolators available in the literature, implemented in buildings and bridges. Among them, laminated rubber bearing, New-Zealand rubber bearing, lead rubber bearing, friction bearing, etc. are commonly used. A large number of analytical and experimental works have been carried out by different researchers (Fan et al., 1991; Matsagar and Jangid, 2004; Jangid, 2010) to investigate the effectiveness of lead rubber bearing for resisting structural vibration under earthquake. The performance of the laminated rubber bearing under near-fault ground motion is investigated by Jangid and Kelly (2001) and Alhan and Gavin (2004). In these studies, the optimal value of the damping ratio of the isolator which plays a key role to design a base isolation system is estimated by minimizing the superstructure responses. Khaloo et al. (2020) investigated the performance of the bonded and unbonded steel-reinforced elastomeric bearing. Dao et al. (2020) developed the statistical equation for predicting nonlinear time history displacement of passive isolation systems. In this section, a brief overview of base isolation techniques is presented. Apart from this, supplemental damping systems are becoming popular among researchers. This kind of damping technology is introduced into the structures for the dissipation of energy induced by the dynamic external loading. The supplemental damping systems can be classified into three categories, i.e. passive, active and semi-active systems (Lago et al., 2018). A brief overview of these three control strategies is presented below.

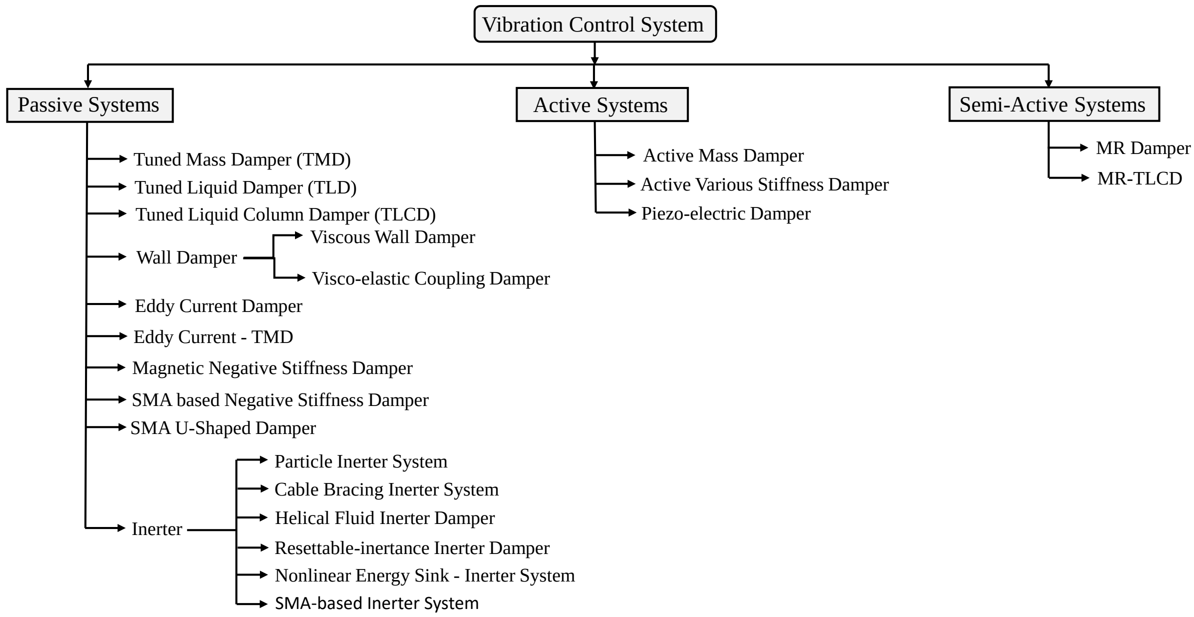

Figure 2.1: Vibration control systems for buildings

2.1 Passive vibration control strategy

In general, passive vibration control systems do not require any external power source, monitoring system, sensors, or actuators. After installation of these kinds of dampers, the properties of the damper are not changed and it operates as per its design. Normally, passive damping systems are considered to be economical and robust. However, the robustness of this kind of dampers is becoming questionable as the dynamic forces are uncertain and the passive damping system does not provide any guarantee to show the same performance against any external excitation. With this in view, a passive damping system is generally classified into three categories i.e. displacement-activated, velocity-activated, and motion-activated. Metallic dampers, friction dampers, self-centering dampers, and viscoelastic dampers are some of the popular displacement-activated devices. By the relative displacement between the contact point which is connected with structures, the seismic energy is absorbed partially. Metallic dampers (Aghlara and Tahir, 2018) can absorb the energy induced by dynamic forces through hysteretic behavior when they deform into the post-elastic range. A friction damper (Mualla and Belev, 2002) uses the friction caused by the sliding between two surfaces to dissipate the energy. Velocity-activated dampers dissipate the energy using the relative velocity of the junction between the dampers and the structure. Viscous (Lee and Taylor, 2001) and visco-elastic dampers (Tsai and Lee, 1993) are some of the most popular velocity-activated dampers. These kinds of dampers depend on the velocity of the structural system and frequency of the motion so that it can work out of the phase and maximum force from the dampers can be offered into the structure depending upon the peak deformation of the structure. Lastly, the motion-activated dampers, which are commonly used for vibration mitigation of tall structures, are tuned mass damper (TMD) (Chakraborty and Roy, 2011), tuned liquid damper (TLD) (Fujino et al., 1992; Sun et al., 1992), tuned liquid column damper (TLCD) (Wu et al., 2005), etc. These kinds of dampers are designed with respect to the fundamental period of the structure.

2.2 Active vibration control strategy

The active system (Ikeda, 2009; Yang et al., 2017) provides the control force to the structure depending upon the current states (i.e. displacement, velocity, or acceleration) of the structure. To measure the states of the system, sensors are generally provided into the structure. Once the current states are estimated, the active system determines the required control force and provides it into the structure at the next time step. Therefore, a time lag is normally found, and thus, to install an active system into the structure, time-delay analysis should be carried out (Mirafzal et al., 2016; Sinou and Chomette, 2021). The active system can be controlled in real-time using an external power source. However, there is a disadvantage of using an active system, that is, during a severe earthquake, the power source may be lost and as a result, the active system stops its functioning. That's why active systems are not preferred to mitigate the vibration in civil engineering structures.

2.3 Semi-active vibration control strategy

Unlike active systems, a semi-active system uses fewer external power sources to activate its system. These kinds of damping systems do not provide the control force into the structure, rather they modify the structural properties such as damping of the system. Magneto-Rheological (MR) damper (Cho et al., 2005; Guo et al., 2006) is one of the most popular semi-active damping systems.

2.4 Hybrid vibration control strategy

In the recent decade, the hybrid control strategy (Saito et al., 2001; Lin et al., 2007; Tso et al., 2013; Li et al., 2021) has gained popularity among researchers as it consists of a combination of active and passive control systems. In this control strategy, the vibration is mitigated in a real-time manner by using sensors placed into the structures. The advantage of using this control strategy is that if the power supply might be lost, the control system does not stop its functioning as the passive device still works. They also modify the structural behavior which ensures the safety and serviceability of a structure.

2.5 Review on damping technologies

In this section, a brief introduction of existing and the current emerging damping technologies are presented, which are shown in Fig. 2.1. This study is mainly focused on passive and semi-active damping technologies.

2.5.1 Tuned mass damper

Tuned mass damper (TMD) (Kaynia et al., 1981) is one of the oldest motion-activated passive damping technology, used to control the sway motion of high-rise buildings against a variety of extreme events such as wind and earthquake. Generally, it is installed at top of the structure. A TMD consists of a mass that is connected with the floor by a spring and a viscous damper. Before installing TMD into the structure, TMD is tuned with respect to the fundamental time period of the main structure so that by vibrating TMD, it can offer a resisting force opposite to the structural motion to keep storey responses minimal. The performance of the TMD depends on the mass ratio (i.e. ratio of TMD mass to total structural weight), tuning frequency ratio (i.e. frequency of the TMD to fundamental frequency of the structure, which is generally considered to be 1), and the damping ratio of the TMD which signifies the dissipation capability of the energy (Hoang et al., 2008). An example, in Taipei 101 skyscraper in Taiwan (Kourakis, 2007), a pendulum-tuned mass damper is placed which is till now the largest and heaviest TMD. The diameter of the TMD is 18 feet, made of steel with 660 metric ton weight, and suspended the pendulum TMD by eight cables from the upper stories of the tower.

2.5.2 Tuned liquid damper

A tuned liquid damper (TLD) is also a motion-activated passive damper which is consisted of a rigid tank, placed at the top of the structure. The tank is partially filled with a liquid (typically water) and dissipates the energy due to external excitation using sloshing of water inside the tank. Due to sloshing of water, damping is introduced and due to damping, vibration is minimized. Like TMD, TLD is also tuned with the fundamental period of the structure by selecting the proper length of the tank and depth of the liquid. The performance of the TLD for the vibration mitigation is investigated by many researchers (Fujii et al., 1990; Wakahara et al., 1992; Welt and Modi, 1992a; 1992b; Chang and Gu, 1999; Shankar and Balendra, 2002; Li et al., 2012c). It is reported that by sloshing of water, damping in TLD arises maximum up to 0.5% (Fediw et al., 1995). To enhance the damping in TLD, various types of screens or flow damping devices are used inside the TLD (Konar and Ghosh, 2021). Overall, TLD has proven an efficient passive damping device to mitigate dynamic excitation-induced vibration.

2.5.3 Tuned liquid column damper

Tuned liquid column damper (TLCD) is one of the common motion-activated passive damper, similar to TLD, where a U-shaped container is used instead of a rigid tank.

The basic principle is the energy transfer from the main structure to TLCD. Generally, TLCD comprises a rigid piping system, which is installed with the structure, preferably at the top storey. TLCD is partially filled with a liquid, preferably water. Due to the oscillating motion of the liquid through the orifice used in the U-shaped container, inherent damping is introduced which helps to dissipate the energy induced by external forces. As the damping produced by TLCD depends on the head-loss coefficient for the orifice and the velocity of the oscillating liquid, TLCD should be designed before installation (Balendra et al., 1995; Gao et al., 1997; Yalla and Kareem, 2000). In recent decades, various techniques have been implemented to improve the damping in TLCD such as by using the high viscous liquid, variable orifice and different shapes of liquid container (Das and Choudhury, 2017). The performance of different shapes of TLCD such as U-shaped, V-shaped, spherical cross-section area, etc. has been investigated by researchers (Chen and Georgakis, 2015). Gao et al. (1997) showed the enhanced performance of V-shaped TLCD compared to U-shaped for mitigating wind-induced vibration. Recently, steel balls are used instead of the orifice in the TLCD (named as tuned liquid column ball damper) (Al-Saif et al., 2011; Gur et al., 2015). Overall, TLCD has proven its efficiency to suppress the wind and earthquake-induced vibration for the tall structure.

2.5.4 Magneto-rheological TLCD

Magneto-rheological tuned liquid column damper (MRTLCD) is a special kind of semi-active motion-activated device, used to control wind and earthquake-induced vibration for high-rise buildings. It is similar to TLCD, only magneto-rheological smart material is used instead of water. In presence of an electric or magnetic field, the magnetic particles suspended in the viscous fluid in the damper change their properties, resulting in the viscosity of the fluid is altered, and thus damping in MRTLCD is increased. The performance of MRTLCD for suppressing the wind and earthquake-induced vibration for the structures are found in Wang et al. (2005).

2.5.5 Wall dampers

This type of damper provides the damping into the primary structure when relative displacement between two floors occurs, and due to this, the shearing effect in the dampers occurs. There are two configurations of wall dampers, i.e. (a) Viscous wall damper and (b) Visco-elastic wall damper.

Viscous wall damper

A viscous wall damper (Lu et al., 2008; Hejazi et al., 2016) generally consists of a narrow tank filled with highly viscous fluid and a vane made of steel. The damper is connected with the bottom storey and the vane is attached with the top storey which is submerged into the viscous fluid . Due to external excitation, when storey displacement occurs, the top of the vane moves relative to the tank and shears the viscous fluid by which the supplementary damping is added with the primary structure.

Visco-elastic coupling damper

Visco-elastic coupling damper (Christopoulos and Montgomery, 2013; Pant et al., 2019) consists of visco-elastic material layers which are placed in between the steel plates. Each consecutive steel layer is extended out to the opposite side which is used to anchor into the structural walls. This kind of damper is generally used as an alternative to coupling beams. During the deformation of the building laterally or torsionally due to external dynamic loads, the walls are deformed relative to one another, resulting in differential vertical displacement within the coupling elements deforming the visco-elastic material layers in shear and thus provides displacement and velocity-dependent forces.

2.5.6 Eddy current damper

Eddy current damper (Sodano et al., 2005) has been gained popularity in recent decades. It utilizes the eddy current when it is exposed to a varying magnetic field. Eddy current damper is composed of an outer tube, used as a conductor, and an array of axially magnetized ring-shaped permanent magnets which are separated by iron pole pieces as a mover. Due to the relative motion of the field source and the conductor, this eddy current flows through the device. In presence of the magnetic field, an external magnetic field is produced by which repulsive force is inducted into the system which is proportional to the relative velocity of the field and the conductor (Ebrahimi et al., 2009). Also, due to electromagnetic force, the damping is induced into the structural system and results in a reduction of the amplitude of the structural responses.

2.5.7 Eddy current - tuned mass damper

Eddy current-tuned mass damper (EC-TMD) is a special kind of variant of eddy current damper, proposed by Lian et al. (2018). In this system, an eddy current damper is coupled with a tuned mass damper. This enhanced system utilizes the advantages of an eddy current damper, which improves the tuned mass damper's performance. Due to relative velocity between the copper plate and permanent magnets, eddy current-induced, and as a result, a repulsive force is generated by which the overall damping of the system is enhanced. It is also noted that the damping properties of EC-TMD can be altered by changing the material properties or by changing the strength of the permanent magnets.

2.5.8 Magnetic negative stiffness damper

Magnetic negative stiffness damper (MNSD) is one of the emerging damping technology, proposed by Shi and Zhu (2015). It consists of several permanent magnets which are arranged in a conductive pipe. It combines the advantages of the negative stiffness damper and the eddy current damper. The negative stiffness produced in this type of damper can be controlled by placing the permanent magnets in a different arrangement. Shi and Zhu (2015) proposed two different configurations of MNSDs. In general, MNSD is composed of static and moving magnets which are separated by a fixing spacer and a shaft on which these magnets can move. The entire arrangement is placed within a conductive pipe. Out of these two types of magnets, static magnets are fixed and moving magnets can move on the shaft. To prevent the collision between these two types of magnets while moving, a spacer is used. Two static and one moving magnets with the same pole orientations are used. During equilibrium, the distance from moving magnets to other static magnets is kept as same so that net force due to the interaction between magnets becomes zero. Due to external force, when moving magnet shifts from its equilibrium position, a force is induced opposition to the motion of the moving magnets to keep its original equilibrium state, thus negative stiffness is induced in MNSD. The nonlinear interaction force between two magnets can be increased by decreasing the distance between static and moving magnets.

The arrangement of design B of MNSD is slightly different from design A. In the previous case, the static magnets are placed inside the conductive pipe. In this case, a magnetic ring and magnetic cylinder are used. The moving magnets are placed inside the pipe, the same as design A. At the equilibrium, both moving and permanent magnets are placed concentrically. When the inner magnet shifts from its equilibrium position, the repelling force is induced between these two magnets which are counterbalanced by the external force. Like previous, in this case, the generated repelling force is also opposite to the direction of the motion of the magnets, thus negative stiffness behavior is found. The mathematical formulation of force-deformation hysteresis of MNSD is proposed by Liu and Lui (2020). As it is a new damping technology proposed by few researchers, it needs further experimental and numerical investigations.

2.5.9 SMA-based negative stiffness damper

Self-centering negative stiffness damper (SCNSD) is a special kind of self-centering device (i.e. zero residual displacements) which is composed of superelastic shape memory alloy (SMA) and pre-pressed springs, arranged in parallel to enhance the damping property of the system. Liu et al. (2018) proposed this novel self-centering device. In this device, SMA wire mainly contributes to the self-centering behavior and energy dissipation mechanism. On the other hand, two pre-pressed springs are used to capture the negative stiffness behavior and also contribute to damping enhancement. The arrangement of SCNSD is that the upper, middle, and lower portions of the SMA wire are fixed which is connected with a piston. The pre-pressed springs are arranged in the perpendicular direction of the arrangement. During the movement of the piston either upwards or downward, SMA offers the superelastic force opposite to the direction of motion while the pre-pressed springs provide the force to bring back the central connector at its equilibrium position, thus negative stiffness is induced.

2.5.10 SMA U-shaped damper

SMA U-shaped damper is a novel self-centering damper, proposed by Wang and Zhu (2018). This kind of special damper is mainly used for energy dissipation between the walls. It is composed of two straight portions and one semi-circle part. Those straight portions generally clamped with on the coupled wall or base of the structure through-bolt connections. The flexural deformation on this damper takes place by relative movement between those two straight portions. It is obvious, when the damper experiences the deformation, the radius of curvature is also changed. Due to this, the plasticity concentration at a fixed location can be prevented.

2.5.11 Inerter damper

Despite the advantages of the above-mentioned mass dampers such as TMD, TLD, TLCD, etc., sometimes those kinds of dampers are not feasible practically due to their large mass. They perform better control with a larger mass. Therefore, the larger mass on the structure may lead to adverse effects, resulting in significant vibration. With this in view, inerters are developed as an alternative to mass dampers. The flywheels are used in the inerters instead of providing larger mass where the inertance is significantly larger than its original weight (Smith, 2002). The configuration of inerter is shown in Fig. 2.2. Generally, inerters are lightweight dampers, having two terminals. The inertia force offered by inerter due to the rotating flywheel is proportional to the relative acceleration between two terminals of inerter. Because of that, it transforms the linear displacement into rotational displacement which leads to an increase in its effective mass. Presently, three types of inerter are used, i.e. the rack and pinion inerter (Papageorgiou et al., 2009), the ball screw inerter (Li et al., 2012a,b), and the fluid inerter (De Domenico et al., 2019). In the recent decade, the different versions of inerter have been proposed by many researchers, are discussed briefly in the following subsection.

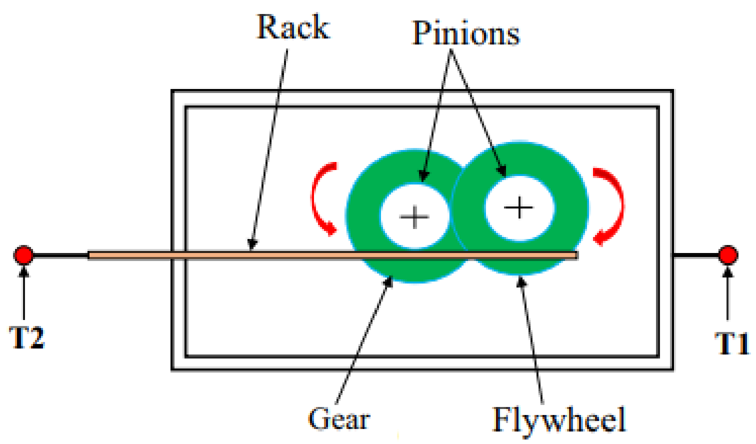

Figure 2.2: Configuration of inerter

Series- parallel inerter system

Zhao et al. (2019a) proposed a novel inerter system for base-isolated structure. In this configuration, the damping and the inerter are arranged in parallel and the combined system is connected with a spring in series. They particularly investigated the performance of the base-isolated structures. For a conventional base isolation system, the isolator experiences excessive deformation. They showed that excessive deformation of the isolators can be reduced using this damping system. Also, the proposed inerter system contributes to the enhancement of the overall damping of the structural system.

Particle inerter system

Zhao et al. (2019b) proposed a particle inerter system. It consists of a spring and tuned inerter damper connected in parallel and this combined system is attached with a container filled with particles in series. Due to the collision of particles, while the structure is under external dynamic action, the vibration energy is dissipated. For this reason, the spring and size of the container should be designed before installation for better performance. The more particles present in the container yield enhancement of energy dissipation.

Cable bracing inerter system

Xie et al. (2019) proposed cable bracing inerter system. It converts translational motion to rotational. It is composed of a pair of bracing cables, a pair of flywheels, and a shaft. The bracing cables are generally pre-tensioned and connected with the structural frame diagonally. When the structure is displaced from its equilibrium position due to external loading, one of those cables is shortened always, thus the shaft starts to rotate. The conductor plate is fixed at the end of the shaft on both ends on which magnets are mounted. Due to this, an electromagnetic field is developed which behaves as an eddy current damper and dissipated the vibrational energy in form of heat.

Helical fluid inerter damper

De Domenico et al. (2019) proposed a helical fluid inerter damper to enhance the performance of a base-isolated structure. The configuration of a helical fluid inerter damper which consists of a moving piston within a cylinder filled with fluid. Due to external force, when the piston rod starts to rotate from one side to another, fluid inside the container is also forced to rotate through the helical coil, thus the inertial force is developed.

Resettable-inertance inerter damper

Garrido et al. (2019) proposed resettable-inertance inerter (RII) which is composed of an inerter that can suddenly be disconnected from the vibrating system by which kinetic energy can be minimized. In general, RII works with the mechanism of reducing the inerter velocity. Also, it can be used as an energy harvesting element where an electric generator is connected with RII which can convert the vibrational energy to electrical energy. This kind of damper has been shown its efficiency in vibration control as well as energy harvesting.

Nonlinear energy sink - inerter system

Javidialesaadi and Wierschem (2019) proposed a novel damper, combination of nonlinear energy sink and inerter for passive vibration control of structures. Through the conversion of relative translational motion to rotational motion, the inerter provides an effective mass to a nonlinear energy sink-based inerter system.

SMA-based inerter system

Jia et al. (2019) proposed an innovative SMA damping inerter. In this arrangement, the SMA element and the inerter are arranged in parallel and the combined system is connected with a linear spring in series. The purpose of using linear spring is to tune the structure while vibrating. In some studies, it is seen that failure of SMA element is prominent under compression. The advantage of this system is that the SMA is always under tension as two terminals of inerter are connected with SMA at both ends. So, while inerter rotates, SMA will always experience tensile force. Also, self-centering properties are found due to SMA which leads to an increase in the fatigue life of the damping system.

Chapter 3

CLT Core Outrigger Building Design

This chapter presents the gravity load design the structural members: beams, columns and shear wall of tall-timber building.

3.1 General description

The plan layout for the tall-timber building is adopted from 42-storey reinforced concrete building reported in (Moehle et al., 2011). The plan dimensions are 32.92 × 32.61 m (Fig. 3.1). In this study, however, the structure is designed for 10-, 15- and 20-storey mass timber. The beams and columns are designed using Glulam section and core wall is designed using CLT. Each storey height is 2.95 m except the first storey (3.81 m).

The core of the building is placed symmetrically at centre of the building. With the aim of better dissipation of energy due to external excitation, the outrigger is used which is connected with core at one end and other end is connected with column (Fig. 3.1). The outriggers are placed symmetrically around the core of the structure. The outrigger lengths from core to the connecting column are 7.31 m and 9.24 m in east-west and north-south direction, respectively. For design purpose, six case study buildings are considered: 10-storey (with and without outrigger), 15-storey (with and without outrigger) and 20-storey (with and without outrigger). The models are built using ETABS software (version 19) for computing the design loads. Initially, structural members are designed without the outriggers. The load bearing structures, i.e. beams and columns, are considered to be Glulam beams and core is made of CLT. Later, with the above architectural plan, outrigger system is considered.

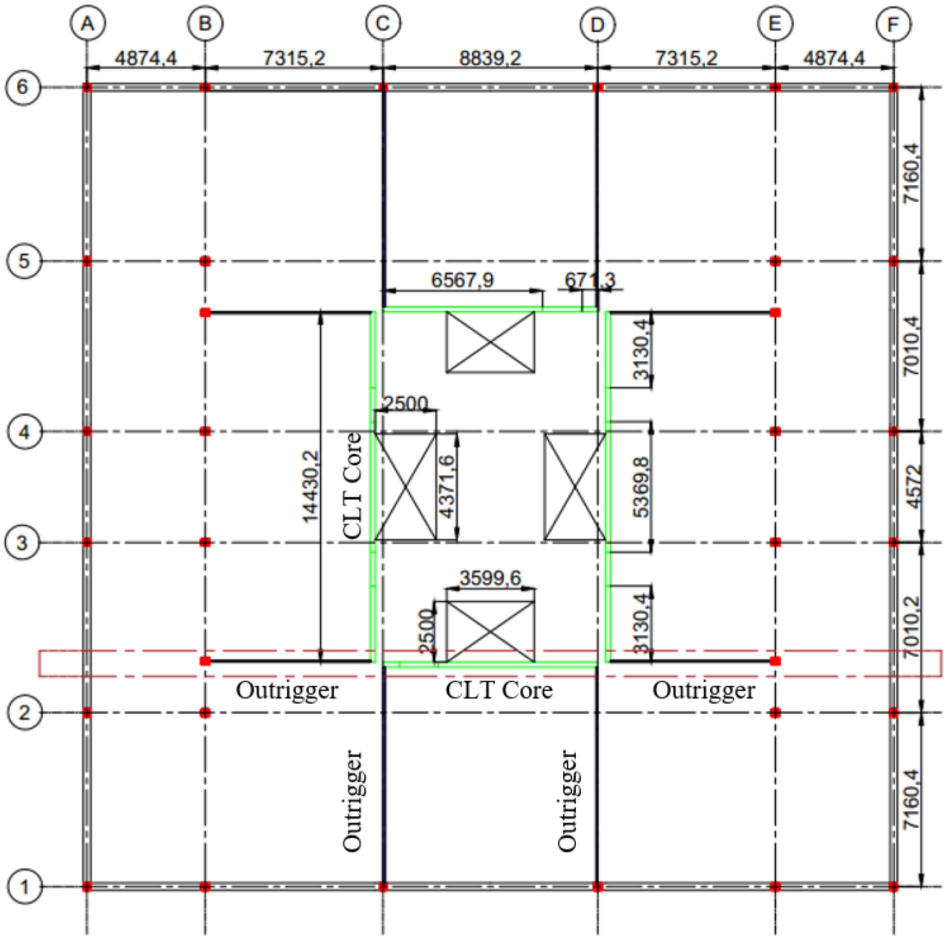

Figure 3.1: Plan dimension of the timber building including outriggers in orthogonal directions

3.2 Load cases and load combinations

Five load combination cases are considered to design the building following National Building Code of Canada (NBC, 2015). The load considered are dead load (D), live load due to use and occupancy (L), load due to snow and rain (S) and earthquake load (E). The members are designed against the maximum load obtained from the combination of the above-mentioned load cases.

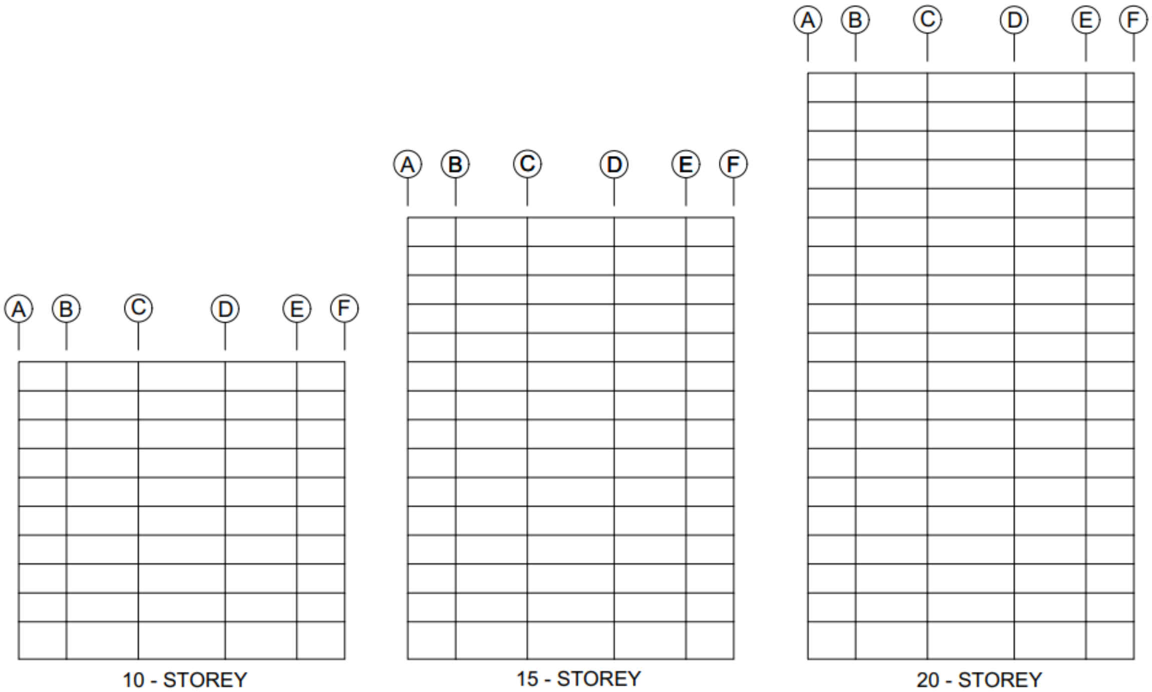

Figure 3.2: Elevation view of 10-, 15- and 20-storey timber buildings

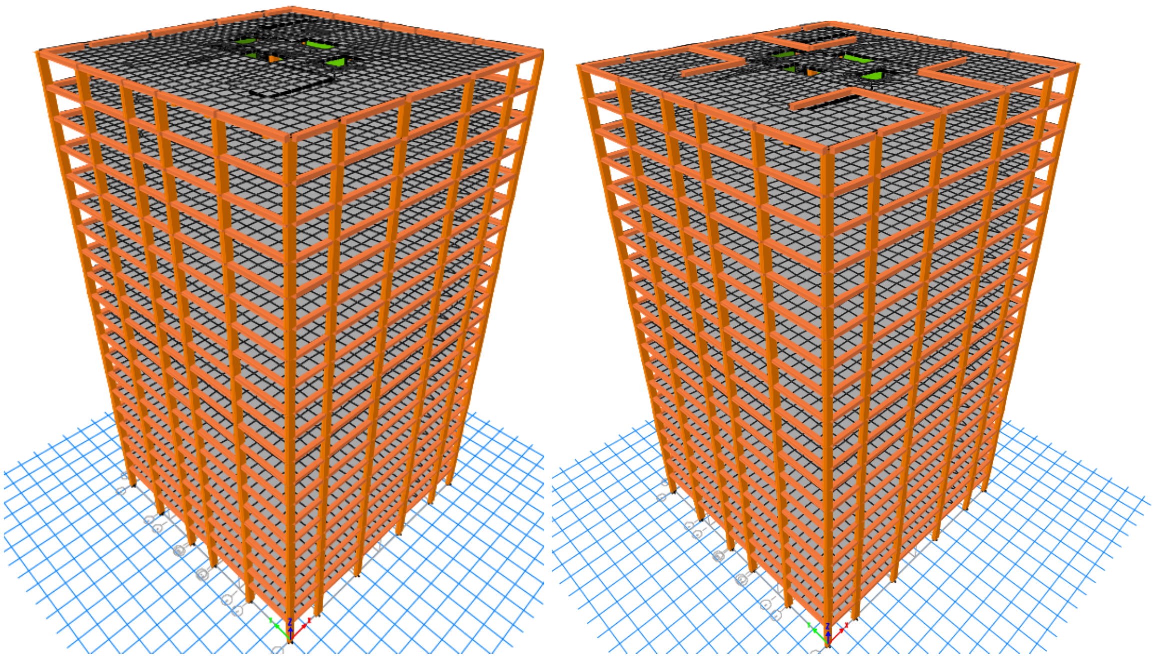

(a) (b)

Figure 3.3: ETABS model: (a) Bare structure; (b) Structure with outrigger

3.2.1 Design loads

In this study, the building is assumed to be located at Vancouver (City Hall), Canada. For this specific site, the parameters related to snow load are taken from National

Building Code of Canada (NBC, 2015).

Structural Design Loading - Gravity Loads:		
Snow load	$S = I_s[S_s(C_b C_w C_s C_a) + S_r]$ where:	
	S_s = Ground snow load	1.8 kPa
	S_r = Rain load	0.2 kPa
	C_b = Basic roof snow factor	0.8
	C_w = Wind exposure factor (for normal condition)	1.0
	C_s = Roof slope factor (for $\alpha \leq 30^o$)	1.0
	C_a = Accumulation factor	1.0
	I_s = Importance factor	1.0
	For strength: S = $1.0 \times [1.8 \times 0.8 \times 1.0 \times 1.0 \times 1.0 + 0.2]$ =	**1.64 kPa**
	For serviceability: S = $0.9 \times [1.8 \times 0.8 \times 1.0 \times 1.0 \times 1.0 + 0.2]$ =	**1.48 kPa**
Live load		**2.0 kPa**
Superimposed dead load		**0.95 kPa**
Self weight of member		Based on assumed section
Structural Design Loading - Lateral Loads:		
Earthquake	S_a (0.2) = 0.8380 S_a (0.5) = 0.7450 S_a (1.0) = 0.5793	

3.2.2 Design load combination

The load combinations are taken from National Building Code of Canada (NBC, 2015), are given by

Table 3.1: Load combinations for ultimate limit state

Case	Load Combination
1	1.4 D
2	1.25 D + 1.5 L + 1.0 S
3	1.25 D + 1.0 L + 1.5 S
4	1.0 D + 1.0 E + 0.5 L + 0.25 S

3.3 Material properties

In this study, beams and columns of the timber high-rise structure are considered as Glulam and the core of the structure is made of CLT. The material properties of Glulam and CLT are taken from CSA (2014) and Canadian CLT handbook (2019 Edition) (Karacabeyli and Gagnon, 2019). The material properties for Glulam beam, Glulam column and CLT core used in this study are given below.

- **Glulam material property for column:**
  - Grade: Douglas Fir-Larch 16c-E
  - Modulus of elasticity (E): 12400 MPa
  - Strength in compression parallel to grain (f_c): 30.2 MPa
  - Strength in tension parallel to grain at gross section (f_{tg}): 15.3 MPa
  - Strength in bending (f_b): 14.0 MPa
  - Longitudinal shear (f_v): 2.0 MPa
- **Glulam material property for beam:**
  - Grade: Douglas Fir-Larch 24f-E
  - Modulus of elasticity (E): 12800 MPa
  - Strength in bending (f_b): 30.6 MPa
  - Longitudinal shear (f_v): 2.0 MPa
- **CLT material property:**
  - Grade: E1
  - f_b: 28.2 MPa (Longitudinal Layer), 7.0 MPa (Transverse Layer)
  - E: 11700 MPa (Longitudinal Layer) , 9000 MPa (Transverse Layer)
  - f_t: 15.4 MPa (Longitudinal Layer) , 3.2 MPa (Transverse Layer)
  - f_c: 19.3 MPa (Longitudinal Layer), 9.0 MPa (Transverse Layer)
  - f_s: 0.5 MPa (Longitudinal Layer), 0.5 MPa (Transverse Layer)
  - f_{cp}: 5.3 MPa (Longitudinal Layer) , 5.3 MPa (Transverse Layer)

3.4 Design details for 20-storey building

3.4.1 Column design

The design values for column are obtained by using ETABS software (version 19) which are given in the table below.

Table 3.2: Maximum design loads in column at first storey

V_f (kN)	$M_{f,x}$ (kN-m)	$M_{f,y}$ (kN-m)	$M_{f,tor}$ (kN-m)	$N_{f,comp}$ (kN)	$N_{f,ten}$ (kN)
101	150	90	0.29	4067	189

Material properties:

Grade for Glulam column is selected as Douglas Fir-Larch 16c-E. The properties of this grade of timber are (Table 7.3 of CSA O86-14) given by

Modulus of elasticity (E) : 12400 MPa

Strength in compression parallel to grain (f_c) : 30.2 MPa

Strength in tension parallel to grain at gross section (f_{tg}) : 15.3 MPa

Strength in bending (f_b) : 14.0 MPa

Longitudinal shear (f_v) : 2.0 MPa

Cross-sectional properties:

Consider, the cross section of D.Fir-L 16c-E Glulam column : 365 mm $\times$ 1064 mm.

Area of the column (A = bd) : 365 $\times$ 1064 = 388360 mm^2

Moment of inertia (I) : $\begin{cases} I_x = \frac{bd^3}{12} = 36.63 \times 10^9 \ mm^4 \\ I_y = \frac{b^3d}{12} = 4.31 \times 10^9 \ mm^4 \end{cases}$

Section modulus (S) : $\begin{cases} S_x = \frac{bd^2}{6} = 6.88 \times 10^7 \ mm^3 \\ S_y = \frac{b^2d}{6} = 2.36 \times 10^7 \ mm^3 \end{cases}$

Design against compression loads:

Unbraced length of column (L) : 3.81 m

As the column is pinned supported at both ends,

Effective length factor (K_e) : 1.0 (from Table A.6.5.6.1 of CSA O86-14)

Effective length (L_e = K_eL) : 3.81 m

Slenderness ratio (C_c) : 3.81/0.365 = 10.44 $<$ 50

According to CSA O86-14 (Cl. 7.5.8.4.2), the factored compressive resistance parallel to grain, $P_r = \phi F_c A K_{Zcg} K_C$.

ϕ : 0.8

f_c : 30.2 MPa

K_D	: 1.0 (from Table 5.3.2.2 of CSA O86-14)
K_H	: 1.0 (Cl. 7.4.2.2 of CSA O86-14)
K_{Sc}	: 1.0 for dry service condition (from Table 7.4.2 of CSA O86-14)
K_{SE}	: 1.0 for dry service condition (from Table 7.4.2 of CSA O86-14)
K_T	: 1.0
$F_c = f_c(K_D K_H K_{Sc} K_T)$	: 30.2 MPa
Z (Volume = Lbd)	: 3.81 × 0.365 × 1.064 = 1.4797 m^3
K_{Zcg} (min{0.68 $(Z)^{-0.13}$,1})	: 0.68 $\times(1.2516)^{-0.13}$ = 0.65
From Cl. 7.5.8.5 of CSA O86-14, the slenderness factor K_C is given by, $K_C = \left[1.0 + \frac{F_c K_{Zcg} C_c^3}{35(0.87E) K_{SE} K_T}\right]^{-1} = \left[1.0 + \frac{30.2\times0.65\times10.44^3}{35\times(0.87\times12400)\times1.0\times1.0}\right]^{-1} = 0.94$	
Therefore, factored compressive resistance is, $P_r = 0.8 \times 30.2 \times 388360 \times 0.65 \times 0.94 = 5726.79$ KN > 4067 KN(Table 3.2)	
Design against tensile loads:	
According to CSA O86-14 (Cl. 7.5.11), the maximum factored tensile force, $T_r = \phi F_{tg} A_g$	
ϕ	: 0.9
f_{tg}	: 15.3 MPa
$F_{tg} = f_{tg}(K_D K_H K_{Sc} K_T)$	: 15.3 MPa
A_g = A	: 388360 mm^2
Therefore, the factored tensile resistance is, $T_r = 0.9 \times 15.3 \times 388360 = 5347.72$ kN > 189 kN(From Table 3.2)	
Design against bending moment:	
According to CSA O86-14 (Cl. 7.5.6.5.1), the factored bending moment resistance, M_r shall be taken as the minimum of M_{r1} or M_{r2}, as follows $M_{r1} = \phi F_b S K_X K_{Zbg}$ $M_{r2} = \phi F_b S K_X K_L$	
X-X axis:	
Φ	: 0.9
$F_b = f_b(K_D K_H K_{Sb} K_T)$	: 14.0 MPa
$S = S_x$	: 6.88×10^7 mm^3
K_X = Curvature factor = 1.0 (Cl. 7.5.6.5.2 of CSA O86-14)	
K_{Zbg} = $\left(\frac{130}{b}\right)^{0.1}\left(\frac{610}{d}\right)^{0.1}\left(\frac{9100}{L}\right)^{0.1}$ = $\left(\frac{130}{365}\right)^{0.1}\left(\frac{610}{1064}\right)^{0.1}\left(\frac{9100}{3810}\right)^{0.1}$ = 0.93	

C_B (=$\sqrt{L_e d/b^2}$) : $\sqrt{1.92 \times 3810 \times 1064/365^2}$ = 7.64 $<$ 10

K_L : 1.0

The factored moment is,

$$M_{r1} = 0.9 \times 14.0 \times 6.88 \times 10^7 \times 1.0 \times 0.93 = 807.63 \text{ kN-m}$$

$$M_{r2} = 0.9 \times 14.0 \times 6.88 \times 10^7 \times 1.0 \times 1 = 866.88 \text{ kN-m}$$

Factored bending moment resistance (M_r) = 807.63 kN-m $>$ 150 kN-m (Table 3.2)

Y-Y axis:

Φ : 0.9

$F_b = f_b(K_D K_H K_{Sb} K_T)$: 14.0 MPa

$S = S_y$: $.36 \times 10^7$ mm^3

K_X = Curvature factor = 1.0 (Cl. 7.5.6.5.2 of CSA O86-14)

K_{Zbg} = $\left(\frac{130}{b}\right)^{0.1}\left(\frac{610}{d}\right)^{0.1}\left(\frac{9100}{L}\right)^{0.1}$ = $\left(\frac{130}{365}\right)^{0.1}\left(\frac{610}{1064}\right)^{0.1}\left(\frac{9100}{3810}\right)^{0.1}$ = 0.93

C_B (=$\sqrt{L_e d/b^2}$) : $\sqrt{1.92 * 3810 * 1064/365^2}$ = 7.64 $<$ 10

K_L : 1.0

The factored moment is,

$$M_{r1} = 0.9 \times 14.0 \times 2.36 \times 10^7 \times 1.0 \times 0.93 = 277.05 \text{ kN-m}$$

$$M_{r2} = 0.9 \times 14.0 \times 2.36 \times 10^7 \times 1.0 \times 1 = 297.36 \text{ kN-m}$$

Factored bending moment resistance (M_r) = 277.05 kN-m $>$ 90 kN-m (Table 3.2)

Design against combined bending moment and axial load:

Members subject to combined bending and compressive or tensile axial loads shall be designed to satisfy the appropriate interaction equation,

$$\left(\frac{P_f}{P_r}\right)^2 + \frac{M_f}{M_r}\left[\frac{1}{1-\frac{P_f}{P_E}}\right] \leq 1$$

$$\frac{T_f}{T_r} + \frac{M_f}{M_r} \leq 1$$

P_f (Compressive load) : 4067 kN

P_r (Compressive resistance) : 5726.8 kN

M_f (Factored bending moment) : $\begin{cases} M_{f,x} = 150 \text{ kN-m} \\ M_{f,y} = 90 \text{ kN-m} \end{cases}$

M_r (Factored bending moment resistance) : $\begin{cases} M_{r,x} = 807.63 \text{ kN-m} \\ M_{r,y} = 277.05 \text{ kN-m} \end{cases}$

T_f (Tensile load) : 189 KN

T_r (Tensile resistance) : 5347.72 KN

P_E = Euler buckling load in the plane of the applied moment,

$$\begin{cases} P_{E,x} = \frac{\pi^2 E_{05} K_{SE} K_T I_x}{L_e^2} = 2.68 \times 10^8 \text{ kN} \\ P_{E,y} = \frac{\pi^2 E_{05} K_{SE} K_T I_y}{L_e^2} = 3.16 \times 10^7 \text{ kN} \end{cases}$$

$$\left(\frac{P_f}{P_r}\right)^2 + \frac{M_{f,x}}{M_{r,x}}\left[\frac{1}{1-\frac{P_f}{P_{E,x}}}\right] + \frac{M_{f,y}}{M_{r,y}}\left[\frac{1}{1-\frac{P_f}{P_{E,y}}}\right]$$

$$= \left(\frac{4067}{5726.8}\right)^2 + \frac{150}{807.63}\left[\frac{1}{1-\frac{4067}{2.68\times10^8}}\right] + \frac{90}{277.05}\left[\frac{1}{1-\frac{4067}{3.16\times10^7}}\right] = 0.99 < 1.0$$

$$\frac{T_f}{T_r} + \frac{M_{f,x}}{M_{r,x}} = \frac{189}{5347.72} + \frac{150}{807.63} = 0.22 < 1.0$$

$$\frac{T_f}{T_r} + \frac{M_{f,y}}{M_{r,y}} = \frac{189}{5347.72} + \frac{90}{277.05} = 0.36 < 1.0$$

Design against shear:

According to CSA O86-14 (Cl. 7.5.7.2), the factored shear resistance, V_r is given by

$$V_r = \phi F_v \frac{2A_g}{3}$$

ϕ	: 0.9
$F_v = f_v(K_D K_H K_{Sv} K_T)$	: 2.0 MPa
A_g = A	: 388360 mm^2

The factored resistance is,

$$V_r = 0.9 \times 2.0 \times \frac{2\times388360}{3} = 466 \text{ kN} > 101 \text{ kN}$$

Final cross-section:

Finally, cross-section of D.Fir-L 16c-E Glulam column : **365 mm** × **1064 mm**.

3.4.2 Beam design

The force in beams are obtained by using ETABS software (version 19). The design values for beam are given below:

Table 3.3: Maximum design loads in beams

V_f (kN)	M_f (kN-m)
51	84

Material properties:

Grade for Glulam column is selected as Douglas Fir-Larch 24f-E. The properties of this grade of timber are (Table 7.3 of CSA O86-14) given by

Modulus of elasticity (E)	: 12800 MPa
Strength in bending (f_b)	: 30.6 MPa
Longitudinal shear (f_v)	: 2.0 MPa

Cross-sectional properties:

Consider, the cross section of D.Fir-L 24f-E Glulam beam : 215 mm $\times$ 342 mm

Area of the column (A = bd) : 215 $\times$ 342 = 73530 mm^2

Moment of inertia (I) : $\begin{cases} I_x = \frac{bd^3}{12} = 716696910\ mm^4 \\ I_y = \frac{b^3d}{12} = 283243688\ mm^4 \end{cases}$

Section modulus (S) : $\begin{cases} S_x = \frac{bd^2}{6} = 4191210\ mm^3 \\ S_y = \frac{b^2d}{6} = 2634825\ mm^3 \end{cases}$

Design against bending moment:

According to CSA O86-14 (Cl. 7.5.6.5.1), the factored bending moment resistance, M_r shall be taken as the minimum of M_{r1} or M_{r2}, as follows

$$M_{r1} = \phi F_b S K_X K_{Zbg} \qquad M_{r2} = \phi F_b S K_X K_L$$

Φ : 0.9

$F_b = f_b(K_D K_H K_{Sb} K_T)$: 30.6 MPa

S : 4191210 mm^3

K_X = Curvature factor = 1.0 (Cl. 7.5.6.5.2 of CSA O86-14)

K_{Zbg} = $\left(\frac{130}{b}\right)^{0.1}\left(\frac{610}{d}\right)^{0.1}\left(\frac{9100}{L}\right)^{0.1}$ = $\left(\frac{130}{215}\right)^{0.1}\left(\frac{610}{342}\right)^{0.1}\left(\frac{9100}{8839.2}\right)^{0.1}$ = 1.01

C_B (=$\sqrt{L_e d/b^2}$) : $\sqrt{1.92 \times 8839.2 \times 342/215^2}$ = 11.21 $>$ 10

C_K (= $\sqrt{0.97 E K_{SE} K_T/F_b}$) : 20.14 $> C_B$

K_L (=1 - (1/3) $\times$ $(C_B/C_K)^4$) : 0.97

The factored moment is,

$$M_{r1} = 0.9 \times 30.6 \times 4191210 \times 1.0 \times 1.01 = 116.58 \text{ kN-m}$$

$$M_{r2} = 0.9 \times 30.6 \times 4191210 \times 1.0 \times 0.97 = 111.74 \text{ kN-m}$$

Factored bending moment resistance (M_r) = 111.74 kN-m $>$ 84.0 kN-m (Table 3.3)

Design against shear:

Volume of the section (Z) = $A \times L_{Beam}$ = 0.215 $\times$ 0.342 $\times$ 8.839 = 0.65 $m^3 <$ 2.0 m^3

So, according to CSA O86-14 (Cl. 7.5.7.2), the factored shear resistance, V_r is given by

$$V_r = \phi F_v \frac{2A_g}{3}$$

ϕ : 0.9

$F_v = f_v(K_D K_H K_{Sv} K_T)$: 2.0 MPa

A_g = A : 73530 mm^2

$$V_r = 0.9 \times 2.0 \times \frac{2\times73530}{3} = 88.24 \text{ kN} > 51 \text{ kN (From Table 3.3)}$$

Final cross-section:

Finally, cross-section of D.Fir-L 24f-E Glulam beam : **215 mm** $\times$ **342 mm**.

3.4.3 CLT core wall design

The forces in cross laminated timber (CLT) core wall are obtained by using ETABS software (version 19) which are given below:

Table 3.4: Maximum design loads in core wall for walls in X-Direction

V_f (kN)	$M_{f,x}$ (kN-m)	$M_{f,y}$ (kN-m)	$M_{f,tor}$ (kN-m)	$N_{f,comp}$ (kN)	$N_{f,ten}$ (kN)
1436	350	15220	72	7945	3859

Table 3.5: Maximum design loads in core wall for walls in Y-Direction

V_f (kN)	$M_{f,x}$ (kN-m)	$M_{f,y}$ (kN-m)	$M_{f,tor}$ (kN-m)	$N_{f,comp}$ (kN)	$N_{f,ten}$ (kN)
807	230	9923	49	5224	3354

Material properties:

Stress grade for CLT wall is selected as E1. The properties of this grade of CLT are,

Property	Longitudinal layer	Transverse layer
f_b	28.2 MPa	7.0 MPa
E	11700 MPa	9000 MPa
f_t	15.4 MPa	3.2 MPa
f_c	19.3 MPa	9.0 MPa
f_s	0.5 MPa	0.5 MPa
f_{cp}	5.3 MPa	5.3 MPa

Design for CLT walls in X-direction:

Cross-section details:

Consider, 7 layers of CLT of each panel thickness of 35 mm (i.e. 4 longitudinal layers and 3 transverse layers)

Total thickness of wall (h) = 7 × 35 = 245 mm

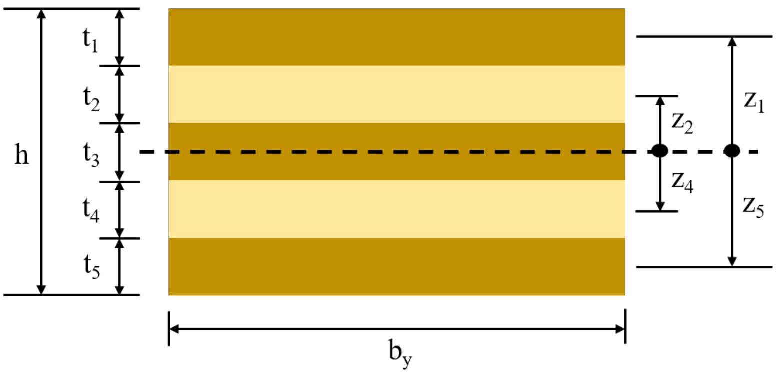

The effective bending stiffness of the panel for the major axis strength axis is given by

$$(EI)_{eff,y} = \sum_{i=1}^{n} E_i \cdot b_y \cdot \frac{t_i^3}{12} + \sum_{i=1}^{n} E_i \cdot b_y \cdot t_i \cdot z_i^2$$

b_y = Width of the panel for the major strength axis = 8839.2 mm

E_i =Modulus of elasticity of laminations in the i-th layer

= 11700 MPa, for laminations in the longitudinal layers

= 9000 MPa, for laminations in the transverse layers

n = Number of layers in the panel = 7

t_i = Thickness of laminations in the i-th layer = 35 mm

z_i = Distance between the center point of the i-th layer and the neutral axis

So, the effective bending stiffness is,

$$\begin{aligned}(EI)_{eff,y} = {} & 8839.2 \times \frac{(35)^3}{12} \times (4 \times 11700 + 3 \times 9000) + \\ & 11700 \times 8839.2 \times 35 \times \left\{\left(\frac{245}{2} - \frac{35}{2}\right)^2 + \left(\frac{245}{2} - 35 - 35 - \frac{35}{2}\right)^2\right\} \times 2 + \\ & 9000 \times 8839.2 \times 35 \times \left\{\left(\frac{245}{2} - 35 - \frac{35}{2}\right)^2\right\} \times 2 \\ = {} & 81.29 \times 10^{12} \text{ N-mm}^2\end{aligned}$$

Design against compressive loads:

The effective thickness, effective cross-sectional area and the effective out-of-plane moment of inertia are obtained as,

$h_{eff}(= \sum_{i=1}^{(n+1)/2} t_{2n-1})$: $4 \times 35 = 140$ mm

$A_{eff}(= b \cdot h_{eff})$: $8839.2 \times 140 = 1237488$ mm^2

$I_{eff,y}(= \frac{b_y h_{eff}^3}{3})$: $\frac{8839.2 \times 140^3}{12} = 2.02 \times 10^9$ mm^4

The effective radius of gyration, r_{eff} is given by

$$r_{eff} = \sqrt{\frac{I_{eff}}{A_{eff}}} = \sqrt{\frac{2.02 \times 10^9}{1237488}} = 40$$

The slenderness ratio (C_c), the size factor for compression (K_{zc}), the slenderness factor for compression K_c are estimated as

$$C_c = \frac{L_e}{\sqrt{12} r_{eff}} = \frac{3810}{\sqrt{12} \times 40} = 27.21 < 43$$

$$K_{zc} = 6.3\left(2\sqrt{3} r_{eff} L\right)^{-0.13} = 6.3\left(2\sqrt{3} \times 40 \times 3810\right)^{-0.13} = 1.13 < 1.3$$

$$K_c = \left[1 + \frac{F_c K_{zc} C_c^3}{35 E_{05} K_{SE} K_T}\right]^{-1} = \left[1 + \frac{f_c(K_D K_H K_{Sc} K_T) K_{zc} C_c^3}{35 E_{05} K_{SE} K_T}\right]^{-1} = \left[1 + \frac{19.3 \times 1 \times 1.13 \times 27.21^3}{35 \times 0.87 \times 11700 \times 1}\right]^{-1} = 0.45$$

Therefore, the factored compressive resistance is,

$$P_r = \phi F_c A_{eff} K_{zc} K_c = 0.8 \times 19.3 \times 1237488 \times 1.13 \times 0.45 = 9683 \text{ kN} > 7945 \text{ kN}$$

Design against bending moment:

The section modulus in the major direction $S_{eff,y}$ is,

$$S_{eff,y} = \frac{(EI)_{eff,y}}{E_1} \cdot \frac{2}{h} = \frac{81.29 \times 10^{12}}{11700} \times \frac{2}{245} = 5.67 \times 10^7 \text{ mm}^3$$

Therefore, the bending resistance is,

$$M_{r,y} = \phi F_b S_{eff,y} K_{rb,y} = 0.9 \times 28.2 \times 5.67 \times 10^7 \times 0.85 = 1224 \text{ kN-m} > 350 \text{ kN-m}$$

Design against combination of axial and bending loads:

CLT panels subject to combined out-of-plane bending and compressive axial load shall be designed to satisfy the interaction equation which is given as

$$\frac{P_f}{P_r} + \frac{M_f}{M_r}\left[\frac{1}{1-\frac{P_f}{P_{E,v}}}\right] \leq 1$$

The Euler buckling load is given by

$$P_E = \frac{\pi^2 E_{05} I_{eff}}{(K_e L)^2} = \frac{\pi^2 \times 0.87 \times 11700 \times 2.02 \times 10^9}{(3810)^2} = 1.4 \times 10^7 \text{ N}$$

Euler buckling load in the plane of the applied bending moment adjusted for shear deformation is given by

$$P_{E,v} = \frac{P_E}{1+\frac{\kappa P_E}{(GA)_{eff}}} = \frac{1.4 \times 10^7}{1+\frac{1 \times 1.4 \times 10^7}{2.32 \times 10^9}} = 1.39 \times 10^7 \text{ N}$$

$$\frac{7945}{9683} + \frac{350}{1224}\left[\frac{1}{1-\frac{7945}{1.39 \times 10^7}}\right] = 1.11 > 1.0$$

The assumed section is not safe against the combination of axial and bending loads.

Consider, 9 layers of CLT of each panel thickness of 35 mm (i.e. 5 longitudinal layers and 4 transverse layers).

Total thickness of wall (h) = 9 $\times$ 35 = 315 mm

The factored compression resistance = P_r = 16288 kN

The bending resistance = $M_{r,y}$ = 1683 kN-m

$$\frac{P_f}{P_r} + \frac{M_f}{M_r}\left[\frac{1}{1-\frac{P_f}{P_{E,v}}}\right] = 0.70 < 1.0$$

Final thickness:

Finally, **315 mm** of thickness of CLT core wall is provided in X direction.

Design for CLT walls in Y-direction:

Cross-section details:

Consider, 7 layers of CLT of each panel thickness of 35 mm (i.e. 4 longitudinal layers and 3 transverse layers)

Total thickness of wall (h) = 7 $\times$ 35 = 245 mm

The effective bending stiffness of the panel for the major axis strength axis is given by

$$(EI)_{eff,y} = \sum_{i=1}^{n} E_i \cdot b_y \cdot \frac{t_i^3}{12} + \sum_{i=1}^{n} E_i \cdot b_y \cdot t_i \cdot z_i^2 = 134.55 \times 10^{12} \text{N-mm}^2$$

Design against compressive loads:

The effective thickness, effective cross-sectional area and the effective out-of-plane moment of inertia are obtained as,

$h_{eff}(=\sum_{i=1}^{(n+1)/2} t_{2n-1})$	: $4 \times 35 = 140$ mm
$A_{eff}(= b \cdot h_{eff})$	: $14630.4 \times 140 = 2048256$ mm^2
$I_{eff,y}(=\frac{b_y h_{eff}^3}{3})$	: $\frac{14630.4 \times 140^3}{12} = 3.35 \times 10^9$ mm^4

The effective radius of gyration, r_{eff} is given by $$r_{eff} = \sqrt{\frac{I_{eff}}{A_{eff}}} = \sqrt{\frac{3.35\times10^9}{2048256}} = 40$$ The slenderness ratio (C_c), the size factor for compression (K_{zc}), the slenderness factor for compression K_c are estimated as $$C_c = \frac{L_e}{\sqrt{12}r_{eff}} = \frac{3810}{\sqrt{12}\times40} = 27.21 < 43$$ $$K_{zc} = 6.3\big(2\sqrt{3}r_{eff}L\big)^{-0.13} = 6.3\big(2\sqrt{3}\times40\times3810\big)^{-0.13} = 1.13 < 1.3$$ $$K_c = \left[1+\frac{F_cK_{zc}C_c^3}{35E_{05}K_{SE}K_T}\right]^{-1} = \left[1+\frac{f_c(K_DK_HK_{Sc}K_T)K_{zc}C_c^3}{35E_{05}K_{SE}K_T}\right]^{-1} = \left[1+\frac{19.3\times1\times1.13\times27.21^3}{35\times0.87\times11700\times1}\right]^{-1} = 0.45$$ Therefore, the factored compressive resistance is, $$P_r = \phi F_cA_{eff}K_{zc}K_c = 0.8\times19.3\times2048256\times1.13\times0.45 = 16026.60 \text{ kN} > 5224 \text{ kN}$$
Design against bending moment:
The section modulus in the major direction $S_{eff,y}$ is, $$S_{eff,y} = \frac{(EI)_{eff,y}}{E_1}\cdot\frac{2}{h} = \frac{134.55\times10^{12}}{11700}\times\frac{2}{245} = 9.38\times10^7 \text{ mm}^3$$ Therefore, the bending resistance is, $$M_{r,y} = \phi F_bS_{eff,y}K_{rb,y} = 0.9\times28.2\times9.38\times10^7\times0.85 = 2025 \text{ kN-m} > 230 \text{ kN-m}$$
Design against combination of axial and bending loads:
CLT panels subject to combined out-of-plane bending and compressive axial load shall be designed to satisfy the interaction equation which is given as $$\frac{P_f}{P_r}+\frac{M_f}{M_r}\left[\frac{1}{1-\frac{P_f}{P_{E,v}}}\right] \leq 1$$ The Euler buckling load is given by $$P_E = \frac{\pi^2E_{05}I_{eff}}{(K_eL)^2} = \frac{\pi^2\times0.87\times11700\times3.35\times10^9}{(3810)^2} = 1.37\times10^7 \text{ N}$$ Euler buckling load in the plane of the applied bending moment adjusted for shear deformation is given by $$P_{E,v} = \frac{P_E}{1+\frac{\kappa P_E}{(GA)_{eff}}} = \frac{1.37\times10^7}{1+\frac{1\times1.37\times10^7}{3.83\times10^9}} = 1.36\times10^7 \text{ N}$$ $$\frac{5224}{16026.60}+\frac{230}{2025}\left[\frac{1}{1-\frac{5224}{1.36\times10^7}}\right] = 0.44 < 1.0$$
Final thickness:
Finally, **245 mm** of thickness of CLT core wall is provided in Y direction.

Table 3.6: Summary of design details of timber buildings

Structural member	Cross-section		
	10-storey	15-storey	20-storey
Beam	175 mm × 304 mm	175 mm × 304 mm	215 mm × 342 mm
Column	315 mm × 1026 mm	315 mm × 1064 mm	365 mm × 1064 mm
Shear Wall	245 mm thickness	245 mm thickness	315 mm thickness

Chapter 4

CLT Core Outrigger Building Design

4.1 Literature review on damped outrigger systems

Outrigger structure enhances overall structural stiffness, reduces top floor drift, and also helps to maintain a balance of the overturning moment between the core-wall and columns attached with the outriggers. Additionally, the outriggers help to prevent the axial shortening of the columns due to temperature and maintain the axial load balance between the shear core and the columns (Taranath, 2016). However, excessive load demand on the columns attached with the outrigger may lead to increase in structural member size and construction costs. To reduce these excessive load demand, Smith and Willford (2007) proposed the viscous damper, installed in the junction of outrigger and column. By the relative motion between the column and the end of the outrigger, the viscous damper strokes and dissipating the energy due to the external load, and thus the overall damping of the system is enhanced. Since then, the damper outrigger system have gained the popularity among the researchers.

Chen et al. (2010) studied the modal damping ratio and frequency of the viscous damper-based outrigger structure while the deformation of the perimeter column is not considered for simplification. However, it is seen that the overall damping of the outrigger structure is dependent on the axial stiffness of the perimeter column, i.e., if the axial stiffness of the column is insufficient, the performance of the outrigger structure is not enhanced irrespective of number of viscous damper used in the structure (Tan et al., 2014). Fang et al. (2015) proposed the general solution for the dynamic behavior of tall structure with multiple damped outrigger considering the axial stiffness of the perimeter columns. Furthermore, Zhou and Li (2014) validated the experimental investigation by numerical simulation under various earthquake records. The performance of the damped outrigger system was investigated with the recent advancement of damping technologies by replacing the viscous damper. Deng et al. (2014) studied the efficiency of the hysteresis-based damped outrigger system under earthquakes. Zhou et al. (2017) investigated the performance of buckling restrained bracing (BRB) arranged in various configurations, used in the outrigger structure. Lin et al. (2018) studied the effects of inelastic deformation of BRB to reduce the seismic induced vibration of a damped outrigger structure. Also, they extended their works for the multiple damped outrigger system (Lin et al., 2019). However, hardening effect in BRB-based outrigger is observed under the severe earthquake, which may lead to local buckling induced deterioration and damage in BRB (Lu et al., 2019). For this reason, Lu et al. (2019) proposed a novel sacrificial energy dissipation outrigger system to enhance the seismic performance. In the recent decade, due to advancement of material technologies, active or semi-active devices are used into the outrigger structure where the fundamental properties of the device are tuned in the real-time which helps to generate the optimal force for suppressing the vibration. With this in view, Chang et al. (2013) developed a magneto-rheological (MR) damper-based outrigger system. The efficiency of MR damper to reduce the seismic induced vibration for the outrigger structure is validated experimentally by Asai et al. (2013). Kim and Kang (2017) investigated the performance of fuzzy logic control algorithm based MR damper for the mitigation of wind and seismic induced vibration for outrigger structure. Though active / semi-active systems have better efficiency to reduce the vibration, these system are cost effective for monitoring. For this reason, the usage of new control strategies and smart materials into the passive system have gained popularity. Asai and Watanabe (2017) developed the tuned inertial mass electromagnetic transducer to control the outrigger structure's response during long-period earthquake excitation. The rotational inertia damper for the seismic mitigation of outrigger structure is proposed by Liu et al. (2018). The above literature depict the effectiveness of the damped outrigger structure, the functionality of the structure after the earthquake needs to be investigated further as residual displacement in the damping system may lead to reduce its fatigue life.

With this in view, shape memory alloy (SMA) has gained the popularity in the recent past due its excellent recovery potential in the post-earthquake (Huang and Chang, 2018; Wang and Zhu, 2018). It has the ability to recover its initial state while it undergoes to the large strain (up to 10%), either by changing the temperature or by inducing stress. The process associated with the change in temperature to capture the self-centering (i.e. residual strain becomes zero) property of SMA, is known as shape memory effect (Tanaka et al., 1995). On the other-hand, the process related to the stress-strain loading-unloading phenomenon, is termed as superelasticity or pseudoelasticity. This behavior is widely used in the passive vibration control applications. Dolce et al. (2000) studied the performance of SMA-based device experimentally, in which SMA is used as a special brace for the framed structure. The effectiveness of SMA damper for vibration mitigation is studied by Han et al. (2003) through experimental and numerical investigations. Li et al. (2008) developed the tension-SMA and scissor-SMA devices, installed with the chevron braces to increase its overall stiffness. They used the pseudoelasticity behavior of SMA and showed the effectiveness of the proposed devices through a shake table test. Ozbulut and Hurlebaus (2011) demonstrated the optimal performance of superelastic SMA damper, combined with friction base isolator to reduce seismic induced vibration for bridges. Further, they investigated the energy dissipation capabilities of the variable friction damper combined with SMA wires for a 20-storey nonlinear benchmark building (Ozbulut and Hurlebaus, 2012). Eatherton et al. (2014) developed self-centering BRB with pretensioned SMA bar for dissipation of seismic energy. Other use of SMA for mitigating dynamic force induced vibration may be found in Araki et al. (2016); Qiu and Zhu (2017).

The above literature focuses on the potential dissipation capabilities of SMA, which motivates the present study for further investigation of the outrigger structure. However, to obtain the optimal performance of the outrigger structure, the locations, number of outriggers, tuning parameters of the damper are needed to design before installation. Smith and Salim (1981) showed the analysis for optimal locations and number of outriggers by minimizing the top floor drift. A closed form solution to estimate the fundamental vibration period of the outrigger structure is proposed by Zhu (1995). Morales-Beltran et al. (2018) performed a parametric study on the outrigger location, damping ratio, and rigidity ratios of core-to-outrigger and core-to-column. Chen et al. (2010) developed a characteristic equation for the optimal location and size of the damper for the single outrigger structure. Hoenderkamp (2008) showed the optimal location for the second outrigger, keeping fixed location of the first outrigger, by maximizing top floor drift reduction. The optimal location of the outrigger for the coupled-wall system is investigated by Zeidabadi et al. (2004). Zhou et al. (2017) showed the optimal location of outrigger for up to three outrigger systems by minimizing inter-storey drift under wind and earthquake. Das and Tesfamariam (2020) investigated the optimal location of the outrigger in the reliability-based design framework.

4.2 Theoretical solution of outrigger system under uniformly distributed loads

In this section, the theoretical solution of multi-outrigger system is presented briefly along with appropriate equations for the uniform loads. Though distribution of wind and earthquake load is not uniform along the height of the structure, the uniformly distributed loads is useful to examine the behavior of the outrigger system and to estimate the approximate outrigger location which is the main design parameter for a outrigger structure. The analysis for the outrigger structure presented in this section, has some certain assumptions. The assumptions adopted for the analysis are:

- Structure is linearly elastic.
- The columns carry only axial forces.
- The outriggers are connected with the core wall rigidly and other end of the outrigger is connected with the column through pin connection.
- Cross-sectional properties of the core-wall, outriggers and columns are uniform throughout the height of the structure.

The first effort is devoted for the two-outrigger system, as shown in Fig. 4.1. After that, this analysis is generalized for N number of outriggers. In Fig. 4.1, it is seen that structure is subjected to a uniform wind load with intensity w. The height of the structure is H. The bending stiffness of the core and outrigger are denoted by (EI) and $(EI)_0$, respectively. The axial stiffness of the columns is represented by $(EA)_c$. The outriggers are located at a height of x_1 and x_2 from the top of the structure. M_1

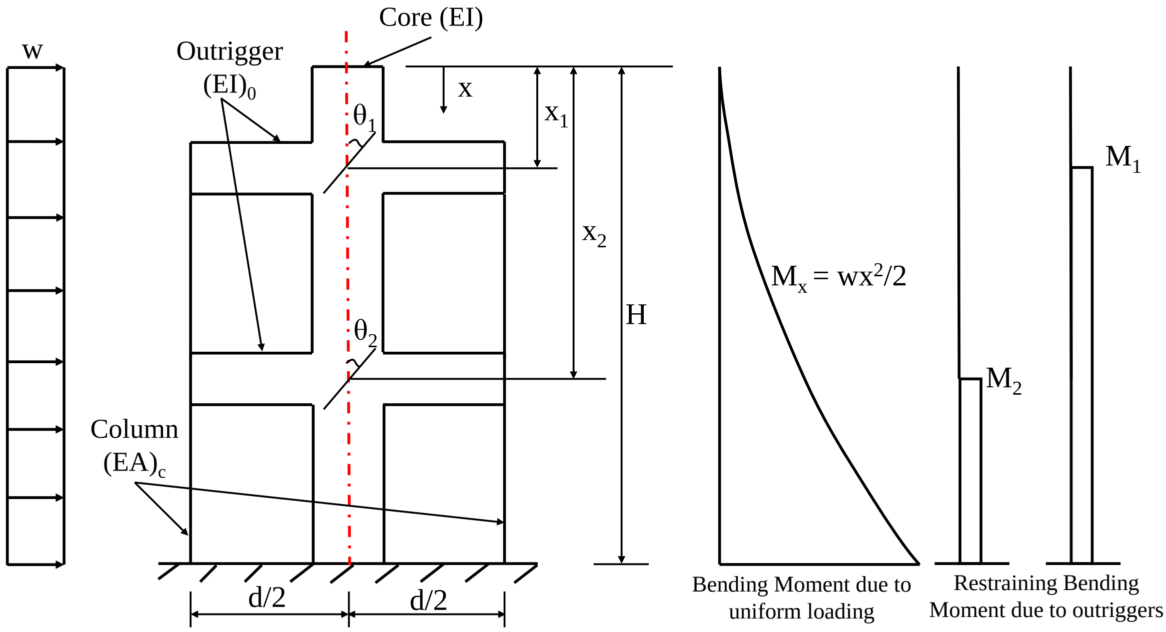

Figure 4.1: The configuration of two outriggers system under wind load

and M_2 are the restraining moment due to the outriggers. Also, $d/2$ is the distance between centre of the core to end of the outrigger. From the Moment area method, the core rotation at the outrigger positions are given by (Smith and Coull, 1991):

$$\theta_1 = \frac{1}{EI}\int_{x_1}^{x_2}\left(\frac{wx^2}{2} - M_1\right)dx + \frac{1}{EI}\int_{x_2}^{H}\left(\frac{wx^2}{2} - M_1 - M_2\right)dx \tag{4.1a}$$

$$\theta_2 = \frac{1}{EI}\int_{x_2}^{H}\left(\frac{wx^2}{2} - M_1 - M_2\right)dx \tag{4.1b}$$

At the junction of outrigger with core, the rotation is given by (Smith and Coull, 1991):

$$\theta_1 = \frac{2M_1(H - x_1)}{d^2(EA)_c} + \frac{2M_2(H - x_2)}{d^2(EA)_c} + \frac{M_1 d}{12(EI)_o} \tag{4.2a}$$

$$\theta_2 = \frac{2(M_1 + M_2)(H - x_2)}{d^2(EA)_c} + \frac{M_2 d}{12(EI)_o} \tag{4.2b}$$

where the effective flexural rigidity of the outrigger, $(EI)_o$ is given by

$$(EI)_o = \left[1 + \frac{(b_c/2)}{(d/2 - b_c/2)}\right]^3 (EI')_o \tag{4.3}$$

where $(EI')_o$ is the actual flexural rigidity of the outrigger. In the above equation, b_c denotes the width of the core. Comparing Eq. 4.1a, Eq. 4.2a and Eq. 4.1b, Eq. 4.2b, it

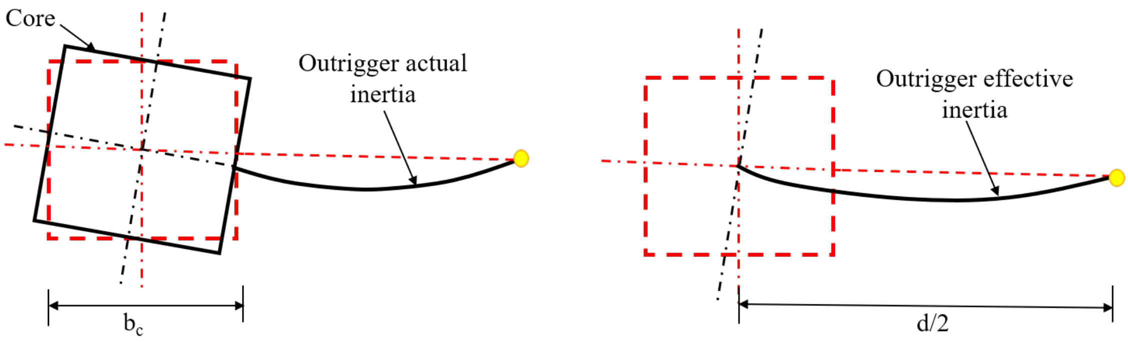

Figure 4.2: Wide-column effect of core and outrigger

can be written as

$$M_1\left[S_1 + S(H - x_1)\right] + M_2S(H - x_2) = \frac{w}{6EI}(H^3 - x_1^3) \tag{4.4a}$$

$$M_1S(H - x_2) + M_2\left[S_1 + S(H - x_2)\right] = \frac{w}{6EI}(H^3 - x_2^3) \tag{4.4b}$$

where the factors S and S_1 are given by

$$S = \frac{1}{EI} + \frac{2}{d^2(EA)_c} \qquad S_1 = \frac{d}{12(EI)_o} \tag{4.5}$$

From Eq. 4.4, it can be expressed in matrix formulation, is given by

$$\begin{bmatrix} S_1 + S(H - x_1) & S(H - x_2) \\ S(H - x_2) & S_1 + S(H - x_2) \end{bmatrix} \begin{bmatrix} M_1 \\ M_2 \end{bmatrix} = \frac{w}{6EI} \begin{bmatrix} H^3 - x_1^3 \\ H^3 - x_2^3 \end{bmatrix} \tag{4.6}$$

The restraining moments are estimated from the above equation, is given by

$$\begin{bmatrix} M_1 \\ M_2 \end{bmatrix} = \frac{w}{6EI} \begin{bmatrix} S_1 + S(H - x_1) & S(H - x_2) \\ S(H - x_2) & S_1 + S(H - x_2) \end{bmatrix}^{-1} \begin{bmatrix} H^3 - x_1^3 \\ H^3 - x_2^3 \end{bmatrix} \tag{4.7}$$

In general, for n number of outriggers, the restraining moments due to each outrigger, are expressed as following

$$\begin{bmatrix} M_1 \\ M_2 \\ \vdots \\ M_i \\ \vdots \\ M_n \end{bmatrix} = \frac{w}{6EI} \begin{bmatrix} S_1 + S(H - x_1) & S(H - x_2) & \cdots & S(H - x_i) & \cdots & S(H - x_n) \\ S(H - x_2) & S_1 + S(H - x_2) & \cdots & S(H - x_i) & \cdots & S(H - x_n) \\ \vdots & \vdots & \cdots & \vdots & \cdots & \vdots \\ S(H - x_i) & S(H - x_i) & \cdots & S_1 + S(H - x_i) & \cdots & S(H - x_n) \\ \vdots & \vdots & \cdots & \vdots & \cdots & \vdots \\ S(H - x_n) & S(H - x_n) & \cdots & S(H - x_n) & \cdots & S_1 + S(H - x_n) \end{bmatrix}^{-1} \begin{bmatrix} H^3 - x_1^3 \\ H^3 - x_2^3 \\ \vdots \\ H^3 - x_i^3 \\ \vdots \\ H^3 - x_n^3 \end{bmatrix} \tag{4.8}$$

The resulting moment in the core is written as

$$M_x = \begin{cases} \frac{wx^2}{2}, & \text{if } 0 \leq \text{x} < x_1 \\ \frac{wx^2}{2} - M_1, & \text{if } x_1 \leq \text{x} < x_2 \\ \frac{wx^2}{2} - M_1 - M_2, & \text{if } x_2 \leq \text{x} \leq \text{H} \end{cases} \tag{4.9}$$

As the core is modeled as a cantilever beam as shown in Fig. 4.3, the deflection of the

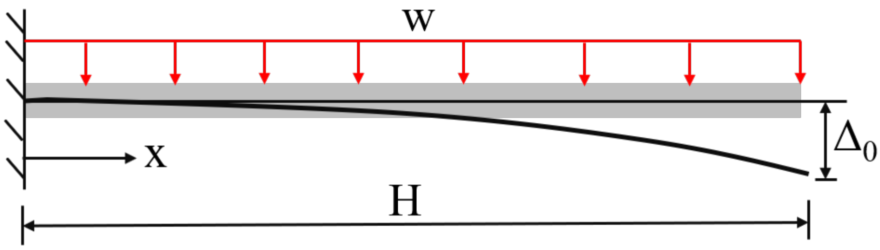

Figure 4.3: Deflection of a cantilever beam under uniformly distributed load

core at any distance x under the uniformly distributed load (udl), w, is written as

$$\Delta(x) = \frac{wx^2}{24EI}(x^2 + 6H^2 - 4Hx) \tag{4.10}$$

The maximum horizontal deflection at the top of the core due to udl is estimated by substituting $x = H$ into Eq. 4.10, yields into

$$\Delta(L) = \frac{wH^4}{8EI} \tag{4.11}$$

Similarly, the deflection at top of the core due to restraining moments can be obtained using conjugate beam method, which is given by

$$\Delta_M = \frac{1}{2EI}\left[M_1(H^2 - x_1^2) + M_2(H^2 - x_2^2)\right] \tag{4.12}$$

The net deflection at the top of the core is written as

$$\Delta_0 = \frac{wH^4}{8EI} - \frac{1}{2EI}\left[M_1(H^2 - x_1^2) + M_2(H^2 - x_2^2)\right] \tag{4.13}$$

In general, for n number of outriggers, the net deflection at the top of the core is expressed as

$$\Delta_0 = \frac{wH^4}{8EI} - \frac{1}{2EI}\sum_{i=1}^{n} M_i(H^2 - x_i^2) \tag{4.14}$$

Optimum location of outriggers

The optimum outrigger locations are estimated by minimizing the deflection at the top of the core. Once the deflection is obtained, optimum outrigger locations are obtained by taking first derivative of deflection at top of core with respect to outrigger positions, is given by

$$\frac{d\Delta_0}{dx_i} = 0 \qquad i = 1, 2, \ldots, n \tag{4.15}$$

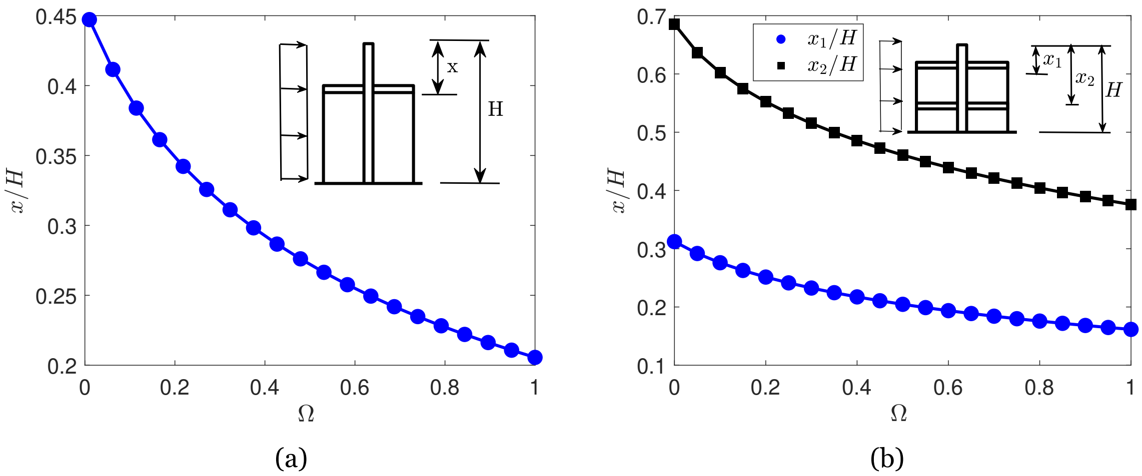

Figure 4.4: Optimum location of outriggers under uniformly distributed load; (a) one-outrigger system and (b) two-outrigger system

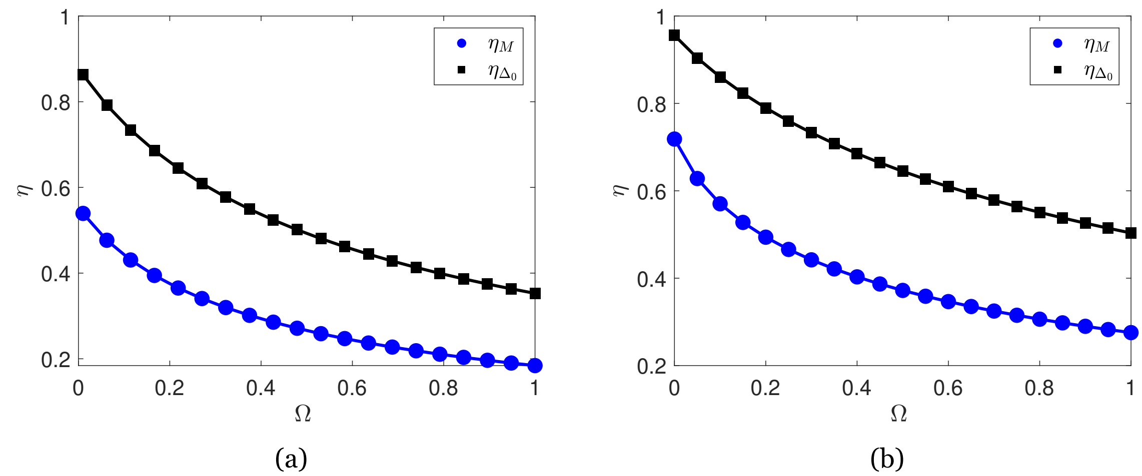

Figure 4.5: Reduction efficiency for core base moment and top drift under uniformly distributed load; (a) one-outrigger system and (b) two-outrigger system

The optimum location of outriggers under uniformly distributed load for one- and two-outrigger system are shown in Fig. 4.4. The results are plotted for varying a non-dimensional parameter (Ω), is given by

$$\Omega = \frac{\beta}{12(1+\alpha)} \tag{4.16}$$

where the non-dimensional parameters, α and β, represent core-to-column and core-to-outrigger rigidities, are given by

$$\alpha = \frac{EI}{(EA)_c(d^2/2)} \qquad \beta = \frac{EI}{(EI)_o}\frac{d}{H} \tag{4.17}$$

Similarly, the reduction efficiency of core base moment and top floor drift are shown in Fig. 4.5 for one- and two-outrigger system.

4.3 Theoretical solution of outrigger system under triangular distributed loads

In this subsection, triangular distributed loads are considered where intensity at the top of the core is w, as shown in Fig. 4.6. From the Moment area method, the core rotation at the outrigger positions are given by

$$\theta_1 = \frac{1}{EI}\int_{x_1}^{x_2}\left(\frac{w}{6H}\big(3Hx^2 - x^3\big) - M_1\right)dx + \frac{1}{EI}\int_{x_2}^{H}\left(\frac{w}{6H}\big(3Hx^2 - x^3\big) - M_1 - M_2\right)dx \tag{4.18a}$$

$$\theta_2 = \frac{1}{EI}\int_{x_2}^{H}\left(\frac{w}{6H}\big(3Hx^2 - x^3\big) - M_1 - M_2\right)dx \tag{4.18b}$$

Like previous formulation, the rotation at the junction of outrigger with core is given by (Smith and Coull, 1991):

$$\theta_1 = \frac{2M_1(H-x_1)}{d^2(EA)_c} + \frac{2M_2(H-x_2)}{d^2(EA)_c} + \frac{M_1 d}{12(EI)_o} \tag{4.19a}$$

$$\theta_2 = \frac{2(M_1+M_2)(H-x_2)}{d^2(EA)_c} + \frac{M_2 d}{12(EI)_o} \tag{4.19b}$$

Comparing Eq. 4.18a, Eq. 4.19a and Eq. 4.18b, Eq. 4.19b, it can be written as

$$M_1\big[S_1 + S(H-x_1)\big] + M_2 S(H-x_2) = \frac{w}{24EIH}(3H^4 + x_1^4 - 4Hx_1^3) \tag{4.20a}$$

$$M_1 S(H-x_2) + M_2\big[S_1 + S(H-x_2)\big] = \frac{w}{24EIH}(3H^4 + x_2^4 - 4Hx_2^3) \tag{4.20b}$$

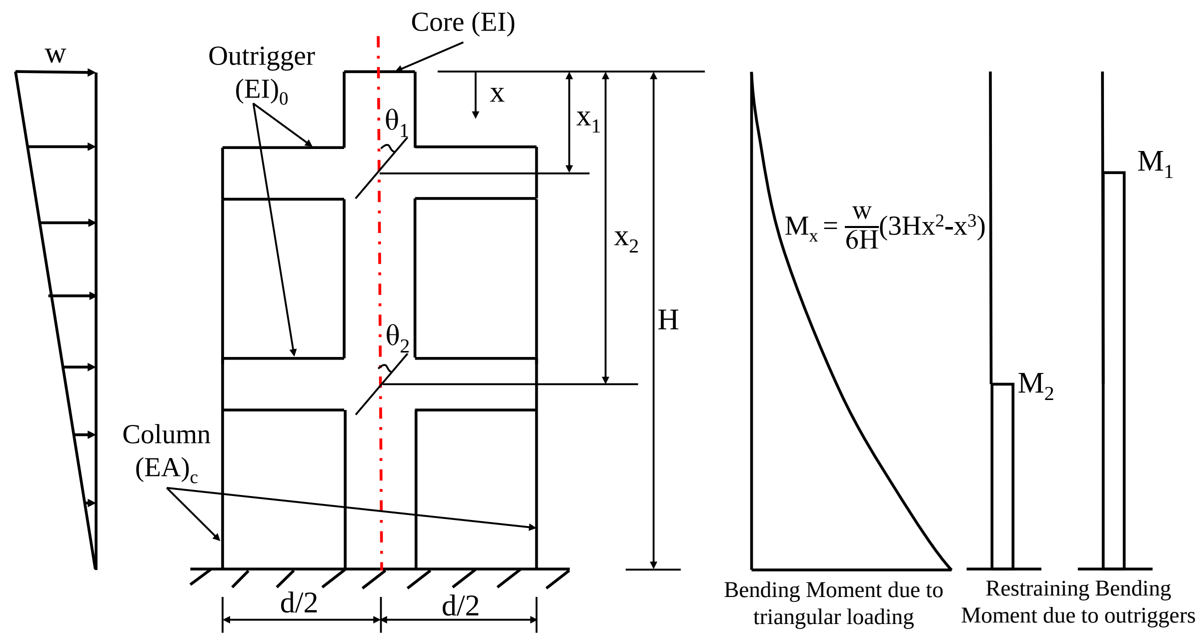

Figure 4.6: The configuration of two outriggers system under earthquake load

where S and S_1 are same as previous, depicted in Eq. 4.5. From Eq. 4.20, it can be expressed in matrix formulation, is given by

$$\begin{bmatrix} S_1 + S(H-x_1) & S(H-x_2) \\ S(H-x_2) & S_1 + S(H-x_2) \end{bmatrix} \begin{bmatrix} M_1 \\ M_2 \end{bmatrix} = \frac{w}{24EIH} \begin{bmatrix} 3H^4 + x_1^4 - 4Hx_1^3 \\ 3H^4 + x_2^4 - 4Hx_2^3 \end{bmatrix} \tag{4.21}$$

The restraining moments are estimated from the above equation, is given by

$$\begin{bmatrix} M_1 \\ M_2 \end{bmatrix} = \frac{w}{24EIH} \begin{bmatrix} S_1 + S(H-x_1) & S(H-x_2) \\ S(H-x_2) & S_1 + S(H-x_2) \end{bmatrix}^{-1} \begin{bmatrix} 3H^4 + x_1^4 - 4Hx_1^3 \\ 3H^4 + x_2^4 - 4Hx_2^3 \end{bmatrix} \tag{4.22}$$

The resulting moment in the core is written as

$$M_x = \begin{cases} \frac{w}{6H}(3Hx^2 - x^3), & \text{if } 0 \leq \text{x} < x_1 \\ \frac{w}{6H}(3Hx^2 - x^3) - M_1, & \text{if } x_1 \leq \text{x} < x_2 \\ \frac{w}{6H}(3Hx^2 - x^3) - M_1 - M_2, & \text{if } x_2 \leq \text{x} \leq \text{H} \end{cases} \tag{4.23}$$

The maximum horizontal deflection at the top of the core due to triangular distributed load is given by

$$\Delta(L) = \frac{11wH^4}{120EI} \tag{4.24}$$

Similarly, the deflection at top of the core due to restraining moments can be obtained using conjugate beam method, which is given by

$$\Delta_M = \frac{1}{2EI}\left[M_1(H^2 - x_1^2) + M_2(H^2 - x_2^2)\right] \tag{4.25}$$

The net deflection at the top of the core is written as

$$\Delta_0 = \frac{11wH^4}{120EI} - \frac{1}{2EI}\left[M_1(H^2 - x_1^2) + M_2(H^2 - x_2^2)\right] \tag{4.26}$$

In general, for n number of outriggers, the net deflection at the top of the core is expressed as

$$\Delta_0 = \frac{11wH^4}{120EI} - \frac{1}{2EI}\sum_{i=1}^{n} M_i(H^2 - x_i^2) \tag{4.27}$$

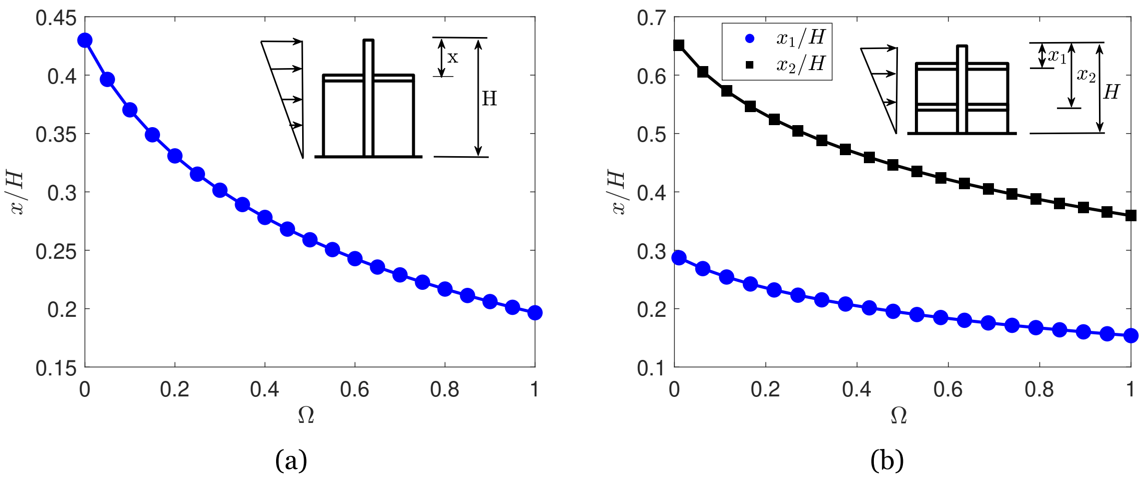

Figure 4.7: Optimum location of outriggers under triangular distributed load; (a) one-outrigger system and (b) two-outrigger system

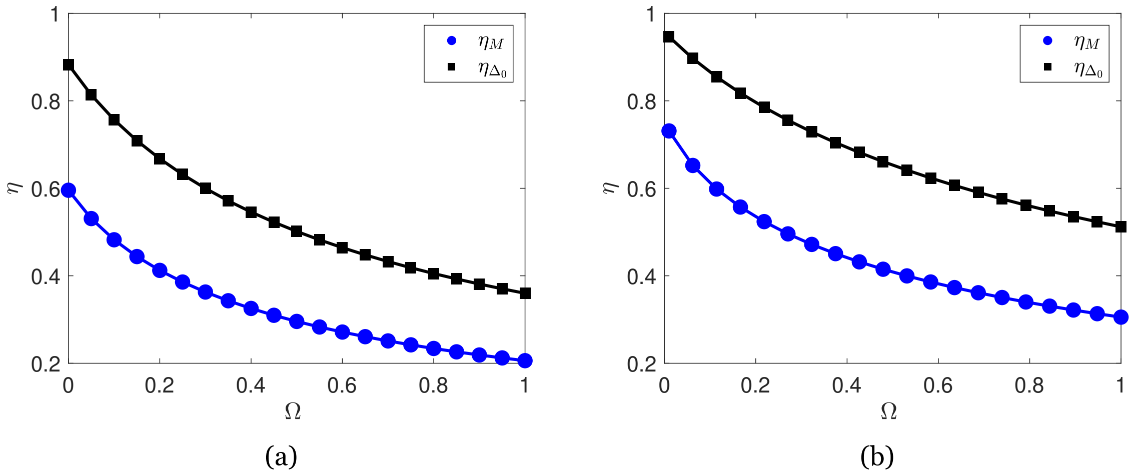

Figure 4.8: Reduction efficiency for core base moment and top drift under triangular distributed load; (a) one-outrigger system and (b) two-outrigger system

Chapter 5

Lagrangian Formulation of Outrigger Structure

In this chapter, a tall-timber building is considered to elucidate the proposed optimal tuning of an SMA-based outrigger for mitigating the earthquake-induced vibration. The architectural description and structural design against the gravity load are discussed in Chapter 3. Once the sizes of the structural member such as beam, column, shear-wall, etc. are estimated, the governing equations of motion are derived for a reduced-order model of SMA-based outrigger for timber structure using Lagrangian formulation. It is followed by ground motion selection, optimal tuning for outriggers using multi-objective optimization, and numerical demonstration of its performance.

5.1 Coupled dynamics of structure and outrigger system

In this section, a reduced order model of high-rise structure with shape memory alloy (SMA) based outrigger beam is considered to demonstrate the optimal tuning of SMA spring. The purpose of SMA spring is to reduce the excessive loads on the perimeter column. Fig. 5.1 shows the architecture of the proposed outrigger system where one end of the outrigger is attached with the core of the structure and other end is connected with SMA spring which is attached with the perimeter column. The core of the structure is idealized as a cantilever beam and each floor mass is considered as a discrete mass which is acted at the junction between floor and core of the structure.

The governing equations of motion of the combined system of shear core and outrigger are derived using Lagrange formulation. The following assumptions have been made in the formulation of the governing equations of motion for the combined system: floor slabs of the system are rigid and the core and columns are fixed at the base of the structure. The outrigger beam is modeled as a torsional spring, having a constant rotational stiffness and the moment developed due to the torsional spring is concentrated at the junction of core of the structure and the outrigger (Fig. 5.1). Also, in this study, the plan of the structure has been considered as symmetric and effect of torsion on the structure is neglected. Thus, the analysis and design was undertaken for planar shear wall as shown in Fig. 5.1.

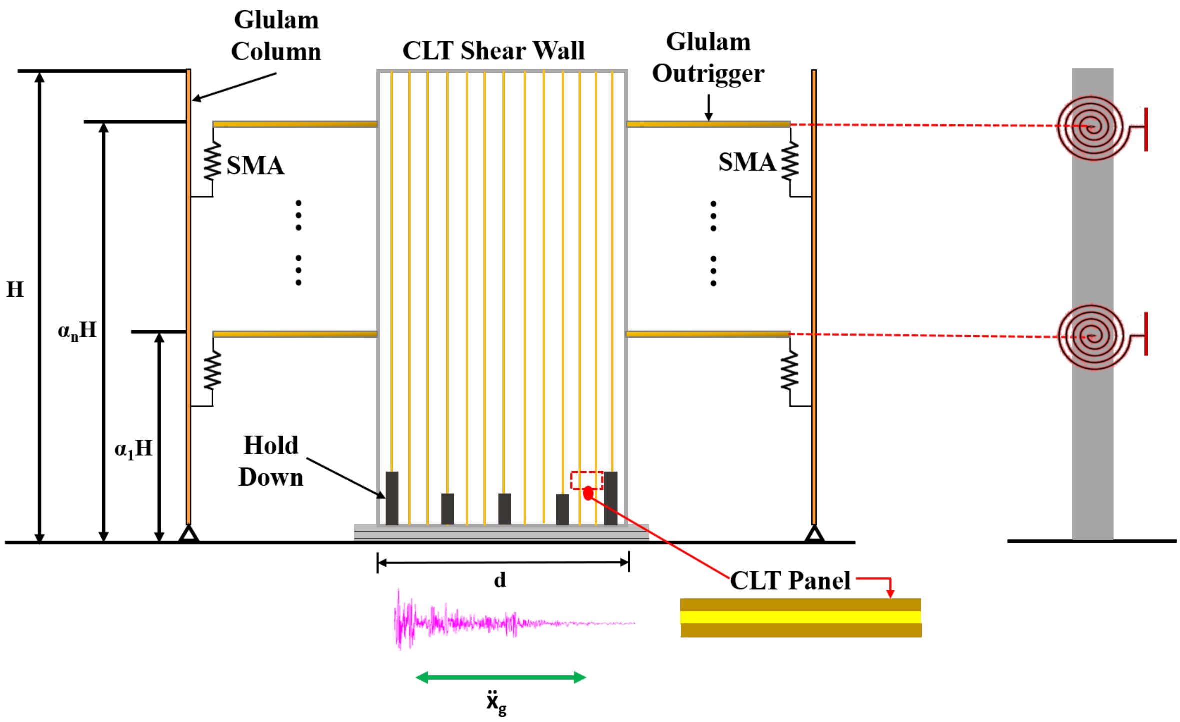

Figure 5.1: Schematic representation of SMA based damped outrigger structure

5.1.1 CLT core representation using Lagrangian formulation

Based on the above assumptions, the core of the structure is modeled as a continuous cantilever beam with a rectangular cross-section and associated equations of motion is formulated based on Hamilton's principle. Consider the flexural stiffness $EI(x)$ and mass per unit height $m(x)$ of the continuous beam. Let $u(x, t)$ be the displacement of the system which is assumed as a function of position and time, is defined as follows

$$u(x,t) = \Phi(x)q(t) = \sum_i \phi_i(x)q_i(t) \tag{5.1}$$

where ϕ_i represents the i^{th} mode-shape of the system. Also, q_i is the displacement of the i^{th} mode shape. Therefore, kinetic energy of the system is given by (Meirovitch, 1980):

$$T = \underbrace{\frac{1}{2}\int_0^H m(x)\left[\frac{\partial u(x,t)}{\partial t}\right]^2 dx}_{\text{Core (Continuous System)}} + \underbrace{\frac{1}{2}\sum_{k=1}^{N}\hat{M}_k\left[\frac{\partial u(H_k,t)}{\partial t}\right]^2}_{\text{Floor (Discrete System)}} \tag{5.2}$$

where x denotes the spatial position of any point on the structure along the height which is bounded in $0 \leq x \leq H$. In Fig. 5.1, H represents the total height of the structure. In Eq. 5.2, the discrete floor mass is denoted by $\hat{M}_k$ which is acted at a height of H_k, measured from the base of the structure. N is the total number of floors in the structure. Similarly, the potential energy of the combined outrigger system can be expressed as (Meirovitch, 1980):

$$V = \underbrace{\frac{1}{2}\int_0^H EI(x)\left[\frac{\partial^2 u(x,t)}{\partial x^2}\right]^2 dx}_{\text{Core (Continuous System)}} + \underbrace{\sum_{j=1}^{n} K_{r_j}\left[\frac{\partial u\big(\alpha_j H,t\big)}{\partial x}\right]^2}_{\text{Outrigger (Discrete System)}} \tag{5.3}$$

where K_{r_j} represents the j^{th} equivalent rotational stiffness due to outrigger. n is the total number of outriggers considered into the structure. In Eq. 5.3, α_i is the normalized position of the outrigger measured from the base of the structure and ranges $0 \leq \alpha_j \leq 1$, as shown in Fig. 5.1. Using the Hamilton's principle, the principle function of dynamics, $\mathcal{A}$ is expressed as time integral of Lagrangian, $\mathcal{L}$ between two time instants t_1 and t_2, is given by (Meirovitch, 1980):

$$\mathcal{A} = \int_{t_1}^{t_2} \mathcal{L}dt \tag{5.4}$$

where Lagrangian $\mathcal{L}$ denotes the difference between the kinetic energy and the potential energy. Using Hamilton's variational principle, minimum value of $\mathcal{A}$, as defined in the above equation, is attained when (Piersol and Paez, 2010):

$$\delta\mathcal{A} = \delta\int_{t_1}^{t_2}\mathcal{L}dt = \int_{t_1}^{t_2}\delta\mathcal{L}dt = \int_{t_1}^{t_2}\delta(T-V)dt = 0 \tag{5.5}$$

where $\delta(\cdot)$ is the variation operator. The nonconservative virtual work due to external force can be expressed as (Meirovitch, 1980):

$$\delta W_{nc}(x,t) = F(x,t)\delta u(x,t) \tag{5.6}$$

Substituting Eqs. 5.2, 5.3 and 5.6 into Eq. 5.5 yields

$$\begin{aligned}\delta\mathcal{A} =& \frac{1}{2}\int_{t_1}^{t_2}\int_0^H \delta\left\{m(x)\left[\frac{\partial u(x,t)}{\partial t}\right]^2 - EI(x)\left[\frac{\partial^2 u(x,t)}{\partial x^2}\right]^2\right\}dxdt \\ &+ \int_{t_1}^{t_2}\delta\left\{\frac{1}{2}\sum_{k=1}^{N}\hat{M}_k\left[\frac{\partial u(H_k,t)}{\partial t}\right]^2 - \sum_{j=1}^{n}K_{r_j}\left[\frac{\partial u\big(\alpha_j H,t\big)}{\partial x}\right]^2\right\}dt + \int_{t_1}^{t_2}\int_0^H \delta W_{nc}dxdt = 0\end{aligned} \tag{5.7}$$

The Lagrangian density variation can be expressed as Meirovitch (1980):

$$\delta\hat{\mathcal{L}} = \frac{\partial\hat{\mathcal{L}}}{\partial u}\delta u + \frac{\partial\hat{\mathcal{L}}}{\partial u'}\delta u' + \frac{\partial\hat{\mathcal{L}}}{\partial u''}\delta u'' + \frac{\partial\hat{\mathcal{L}}}{\partial \dot{u}}\delta\dot{u} \tag{5.8}$$

where $\hat{\mathcal{L}}$ is the Lagrangian density which is expressed as $\hat{\mathcal{L}} = \frac{1}{2}\Big\{m(x)\left[\frac{\partial u(x,t)}{\partial t}\right]^2 - EI(x)\left[\frac{\partial^2 u(x,t)}{\partial x^2}\right]^2\Big\}$. In Eq. 5.8, u' and $\dot{u}$ represent total derivative of u with respect to x and t, respectively. Also, the discrete term of the Lagrangian variation in Eq. 5.7 can be written as

$$\delta\hat{\mathcal{L}}_0 = \frac{\partial\hat{\mathcal{L}}_0}{\partial u'}\delta u' + \frac{\partial\hat{\mathcal{L}}_0}{\partial \dot{u}}\delta\dot{u} \tag{5.9}$$

where $\hat{\mathcal{L}}_0 = \frac{1}{2}\sum_{k=1}^{N}\hat{M}_k\left[\frac{\partial u(H_k,t)}{\partial t}\right]^2 - \sum_{j=1}^{n}K_{r_j}\left[\frac{\partial u(\alpha_j H,t)}{\partial x}\right]^2$. Substituting Eqs. 5.6, 5.8 and 5.9 into Eq. 5.7 yields

$$\int_{t_1}^{t_2}\left[\int_0^H\left(\frac{\partial\hat{\mathcal{L}}}{\partial u}\delta u + \frac{\partial\hat{\mathcal{L}}}{\partial u'}\delta u' + \frac{\partial\hat{\mathcal{L}}}{\partial u''}\delta u'' + \frac{\partial\hat{\mathcal{L}}}{\partial \dot{u}}\delta\dot{u} + F\delta u\right)dx + \delta\hat{\mathcal{L}}_0\right]dt = 0 \tag{5.10}$$

Using integration by parts of Eq. 5.10 with respect to both x and t, the governing equation can be expressed as (Meirovitch, 1980):

$$\int_{t_1}^{t_2}\left[\int_0^H \left\{\frac{\partial\hat{\mathcal{L}}}{\partial u}-\frac{\partial}{\partial x}\Big(\frac{\partial\hat{\mathcal{L}}}{\partial u'}\Big)+\frac{\partial^2}{\partial x^2}\Big(\frac{\partial\hat{\mathcal{L}}}{\partial u''}\Big)-\frac{\partial}{\partial t}\Big(\frac{\partial\hat{\mathcal{L}}}{\partial \dot{u}}\Big)+F\right\}\delta u dx \\ +\left(\frac{\partial\hat{\mathcal{L}}}{\partial u}+\frac{\partial\hat{\mathcal{L}}_0}{\partial u}\right)\delta u\bigg|_{x=H}-\frac{\partial\hat{\mathcal{L}}}{\partial u'}\delta u\bigg|_{x=0}\right]dt=0 \tag{5.11}$$

The governing equation of motion and the boundary conditions for the outrigger structure can be written from Eq. 5.11, which are given by

$$\frac{\partial\hat{\mathcal{L}}}{\partial u}-\frac{\partial}{\partial x}\Big(\frac{\partial\hat{\mathcal{L}}}{\partial u'}\Big)+\frac{\partial^2}{\partial x^2}\Big(\frac{\partial\hat{\mathcal{L}}}{\partial u''}\Big)-\frac{\partial}{\partial t}\Big(\frac{\partial\hat{\mathcal{L}}}{\partial \dot{u}}\Big)+F=0\,;\quad 0<x<H \tag{5.12a}$$

$$\frac{\partial\hat{\mathcal{L}}}{\partial u'}\delta u\bigg|_{x=0}=0 \tag{5.12b}$$

$$\left(\frac{\partial\hat{\mathcal{L}}}{\partial u}+\frac{\partial\hat{\mathcal{L}}_0}{\partial u}\right)\delta u\bigg|_{x=H}=0 \tag{5.12c}$$

Substituting values of $\hat{\mathcal{L}}$ and $\hat{\mathcal{L}}_0$ into the above equations, yield the following differential equations in the following form

$$m\frac{\partial^2 u}{\partial t^2}+\frac{\partial^2}{\partial x^2}\left(EI\frac{\partial^2 u}{\partial x^2}\right)-F=0\,;\quad 0<x<H \tag{5.13a}$$

$$\left[\frac{\partial}{\partial x}\left(EI\frac{\partial^2 u}{\partial x^2}\right)\right]_{x=0}=0 \tag{5.13b}$$

$$\left[EI\frac{\partial^2 u}{\partial x^2}+2\sum_{j=1}^{n}K_{r_j}\frac{\partial u(\alpha_j H,t)}{\partial x}-\sum_{k=1}^{N}\hat{M}_k\frac{\partial u(H_k,t)}{\partial t}\right]_{x=H}=0 \tag{5.13c}$$

Also, the structure is modeled as a cantilever beam whose base is fixed, the essential boundary conditions are as follows

$$u(0,t)=0 \qquad \frac{\partial u(0,t)}{\partial x}=0 \tag{5.14}$$

The modal frequency for the outrigger building is obtained by solving Eq. 5.13 and 5.14 and external force (F) is set to zero. The closed form solutions for the modal frequencies and mode shapes are proposed by Malekinejad and Rahgozar (2013).

5.1.2 Rotational stiffness due to outrigger

For wall-framed structure with outriggers, the outriggers are connected with shear wall at one end, and the other end of outriggers is connected with the column. For simplicity, the effect of outrigger on the structure is modeled as a rotational spring at the junction of shear wall and outrigger. It is evident that the equivalent rotational stiffness due to outrigger depends on the flexural rigidity of the core wall, the outrigger - perimeter column system (Lee et al., 2008). The equivalent rotational stiffness due to outrigger is computed as (Lee et al., 2008):

$$K_r = \frac{1}{\theta} \tag{5.15}$$

where θ_i is the total rotation in outrigger due to restraining moment which can be expressed as

$$\theta = \theta_c + \theta_o \tag{5.16}$$

where θ_c is the rotation in the outrigger due to the restraining forces in the perimeter column, caused by axial deformation of the column. The rotation, θ_a, is computed as (Lee et al., 2008):

$$\theta_c = \frac{2\alpha H}{d^2 E_c A_c} \tag{5.17}$$

where d is the length of the outrigger; (αH) is the location of the outrigger from the ground level and $E_c A_c$ is the axial stiffness of the perimeter column. In Eq. 5.16, θ_o is the flexural deformation of the outrigger system due to the action of column forces, results in additional drift in the floor. The rotation, θ_o, is computed as (Lee et al., 2008):

$$\theta_o = \frac{d}{12 E_o I_{oe}} \tag{5.18}$$

where $E_o I_{oe}$ is the effective flexural stiffness of the outrigger which is obtained from the actual flexural rigidity of the outrigger $E_o I_o$ by converting the flexural rigidity of a wide-column beam to that of an equivalent full span beam, is computed as (Smith and Salim, 1983):

$$E_o I_{oe} = \left[1 + \frac{(b_c/2)}{(d/2 - b_c/2)}\right]^3 E_o I_o \tag{5.19}$$

where b_c is the width of the core, as shown in Fig. 4.2. Finally, the equivalent rotational stiffness for the undamped outrigger system is obtained by substituting Eq. 5.17 and 5.18 into Eq. 5.15 yields,

$$K_r = \left[\frac{2\alpha H}{d^2 E_c A_c} + \frac{d}{12 E_o I_{oe}} \right]^{-1} \tag{5.20}$$

5.1.3 Constitutive model of SMA

In this study, shape memory alloy (SMA) is introduced to augment the energy dissipation characteristics of the outrigger. In the recent past, SMA gained popularity due to its ability to recover large strain. For this reason, fatigue life of the damper increases. Generally, SMA has two micro-structural orientations i.e. austenite phase and martensite phase. The conversion from one state to another is occurred when it exposed to temperature or during the loading-unloading process. When SMA recovers its initial state by application of heat, is known as Shape Memory Effect (SME) while large strain is recovered during unloading, is known as super-elasticity effect (SE). Mainly, SE is utilized in passive vibration control application. Fig. 5.3 shows the typical stress - strain - temperature hysteresis behavior of SMA where the path A-B-C-D-E-A depicts the SME while SE is depicted by the path G-H-I-J-K-L-G. The details of the micro-structural behavior of SMA can be found in Das et al. (2019); Das and Tesfamariam (2020); Das et al. (2020).

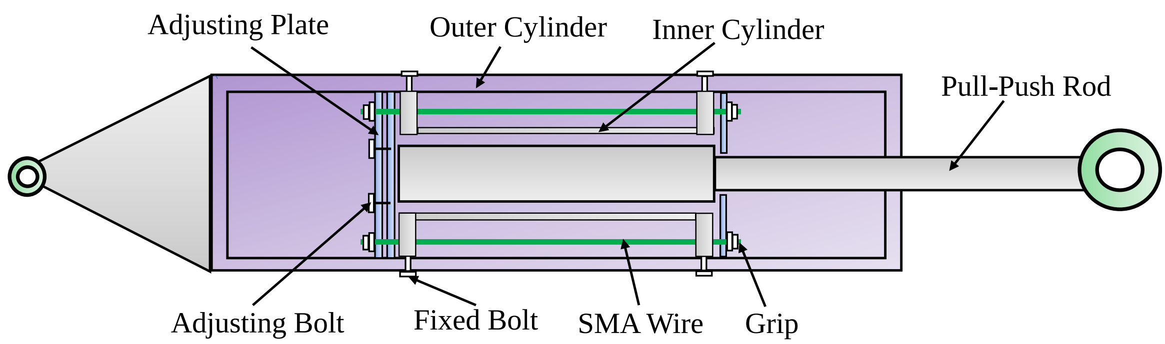

Figure 5.2: Schematic diagram of SMA damper

Different constitutive models have been proposed in the literature for the nonlinear behavior of SMA. Among them, Graesser and Cozzarelli (1991, 1994) is frequently used for passive vibration control. It illustrates super elastic behavior above austenite finish temperature following the classical Bouc-Wen hysteresis representing one

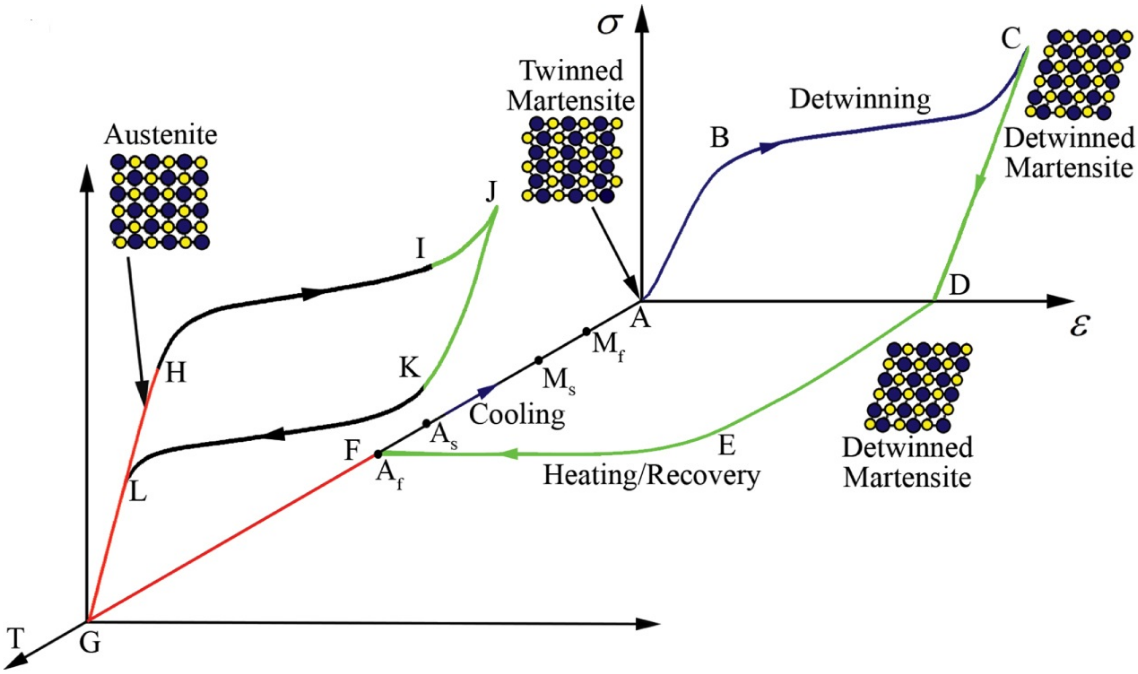

Figure 5.3: Typical stress-strain-temperature hysteresis behavior of SMA

dimensional force vs. deformation characteristics of SMA. The description of this model is given below

$$\dot{F}_{SMA} = k_a \left[\dot{x}_s - |\dot{x}_s| \left| \frac{F_{SMA} - \beta}{F_{ys}} \right|^{n-1} \left(\frac{F_{SMA} - \beta}{F_{ys}} \right) \right] \tag{5.21a}$$

$$\beta = k_a \alpha_s \left[x_s - \frac{F_{SMA}}{k_a} + f_T |x_s|^c \, \text{erf}\,(a x_s) \right] \tag{5.21b}$$

where k_a and F_{ys} represent initial austenite stiffness and yield force in SMA, respectively, while β is the uni-axial back-stress. In Eq. 5.21, α_s is the ratio of the transformation stiffness to initial austenite stiffness k_a of SMA, n and f_T are the two constants, which control the sharpness of transition from elastic to inelastic phase and size of hysteresis, respectively. The other constants a and c control the extent of elastic recovery during unloading and the slope of the unloading path. The erf$\,(x)$ denotes error function, which is given by

$$\text{erf}\,(x) = \frac{2}{\sqrt{\pi}} \int_0^x e^{-t^2} dt \tag{5.22}$$

For the multi-objective optimization, the combined outrigger system needs to be solved multiple times where computational time becomes a factor. For this reason, the

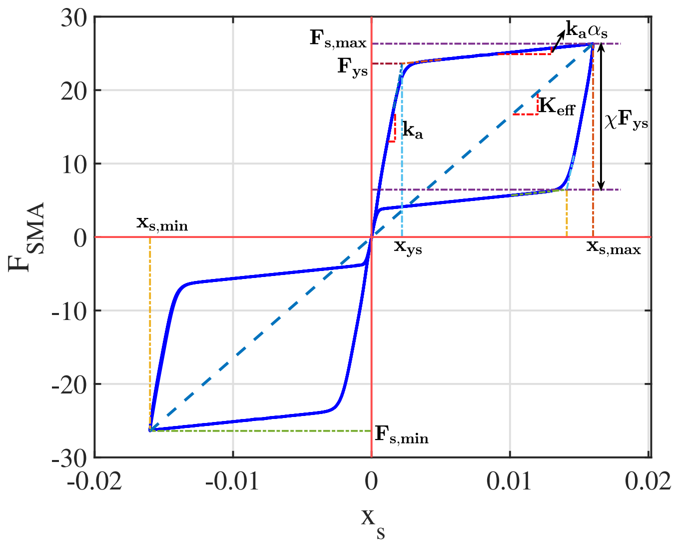

Figure 5.4: Nonlinear hysteresis of SMA

hysteresis model depicted in Eq. 5.21 is converted into an equivalent system, is given by

$$F_{SMA} = K_{eff}x_s + C_{eff}\dot{x}_s \tag{5.23}$$

where K_{eff} and C_{eff} are the equivalent effective stiffness and damping, respectively, which are estimated from the hysteresis of SMA, shown in Fig. 5.4, are given by

$$K_{eff} = \frac{F_{s,max} - F_{s,min}}{x_{s,max} - x_{s,min}} = \frac{1 + \alpha_s(\mu_s - 1)}{\mu_s}k_a \tag{5.24a}$$

$$C_{eff} = 2\xi_{eff}M\omega_{eff} \tag{5.24b}$$

In the above equations, $F_{s,max}$ and $F_{s,min}$ are two extreme forces corresponding to displacements $x_{s,max}$ and $x_{s,min}$, respectively, as shown in Fig. 5.4. Also, μ_s denotes the ductility ratio which is expressed as a ratio of maximum design displacement, $x_{s,max}$ to yield displacement, x_{ys} of SMA. In Eq. 5.21, the yield force, F_{ys} equals to $k_a x_{ys}$. In Eq. 5.24b, M and ω_{eff} are the total mass of the outrigger structure and effective frequency ($\omega_{eff} = \sqrt{K_{eff}/M}$), respectively. The effective modal damping ratio, ξ_{eff} is expressed as

$$\xi_{eff} = \frac{W_D}{2\pi K_{eff}x_{s,max}^2} \tag{5.25}$$

where W_D is the loss of energy per cycle of the hysteresis, equals to $2\chi F_{ys}(x_{s,max} - x_{ys})$. Here χ = (1- α_s).

5.1.4 Coupled system dynamics

Once the modal frequencies and corresponding mode shapes are estimated, the mass and stiffness of any vibrational mode can be expressed as

$$M_i = \int_0^H m\phi_i^2(x)dx \qquad K_i = \omega_i^2 M_i \tag{5.26}$$

where ϕ is the normalized mode shape corresponding to i^{th} vibrational frequency. In this study, SMA damper is installed in the junction of the outrigger and perimeter column, as shown in Fig. 5.5. The restrained moment due the SMA based damper outrigger system is expressed as

$$M_o(x,t) = \delta(x - \alpha H)\left[2\left\{F_{SMA}\left(\frac{d}{2}\right) + K_r\right\}\frac{\partial u(\alpha H, t)}{\partial x}\right] \tag{5.27}$$

where αH is the location of outrigger from the ground level; $(d/2)$ is the length of the outrigger in one side. As outriggers are attached on both sides of the core wall, the factor 2 is added. K_r is the rotational stiffness due to outrigger, obtained from Eq. 5.20. The force induced in SMA damper is denoted by F_{SMA}, as in Eq. 5.21. In Eq. 5.27, $\delta(x - \alpha H)$ represents the Dirac-delta function, is given by

$$\delta(x - \alpha H) = \begin{cases} \infty, & \text{when } x = \alpha H \\ 0, & \text{when } x \neq \alpha H \end{cases} \tag{5.28}$$

Substituting Eq. 5.1 into Eq.5.27 yields

$$M_o(x,t) = \delta(x - \alpha H)\left[2\left\{F_{SMA}\left(\frac{d}{2}\right) + K_r\right\}\sum_i \frac{\partial \phi_i(x)}{\partial x} q_i(t)\right] \tag{5.29}$$

The modal force from the outrigger is expressed as

$$\begin{aligned} F_{o,i}(t) = \int_0^H \phi_i(x) f(x,t)dx &= \int_0^H \phi_i(x)\frac{\partial M_o}{\partial x}dx \\ &= \int_0^H \phi_i(x)\frac{\partial \delta(x - \alpha H)\left[2\left\{F_{SMA}\left(\frac{d}{2}\right) + K_r\right\}\sum_i \frac{\partial \phi_i(x)}{\partial x} q_i(t)\right]}{\partial x}dx \\ &= 2\left\{F_{SMA}\left(\frac{d}{2}\right) + K_r\right\}\left\{\frac{\partial \phi_i(x)}{\partial x}\sum_i \frac{\partial \phi_i(x)}{\partial x}\right\}\Bigg|_{x=\alpha H} q_i(t) \end{aligned} \tag{5.30}$$

Similarly, the modal force due to external loading is written as

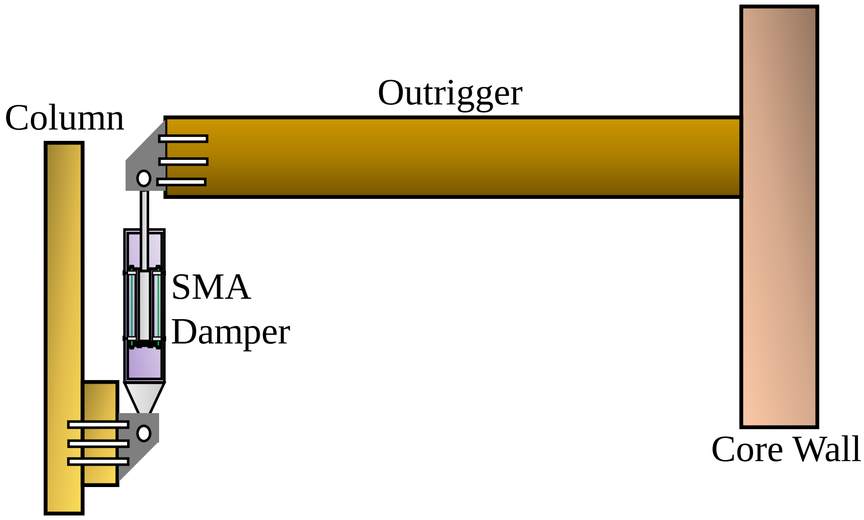

Figure 5.5: Arrangement of SMA-based damped outrigger

$$F_{g,i}(t) = -\int_0^H \phi_i(x) f(x,t) dx = -\int_0^H \phi_i(x) m \ddot{x}_g(t) dx = -S_i m H \ddot{x}_g(t) \tag{5.31}$$

where $\ddot{x}_g$ is the ground acceleration and S_i is the load coefficient of i^{th} vibrational mode. Finally, the governing equation of motion of the outrigger system for i^{th} mode is given by

$$M_i \ddot{q}_i(t) + C_i \dot{q}_i(t) + K_i q_i(t) = F_{g,i}(t) - F_{o,i}(t) \tag{5.32}$$

Considering the first n modes, the above governing equation of motion can be re-written as

$$[M][\ddot{q}(t)] + [C][\dot{q}(t)] + [K][q(t)] = I_g m H \ddot{x}_g(t) - 2\left\{F_{SMA}\left(\frac{d}{2}\right) + K_r\right\}[\bar{\phi}\ \bar{\phi}^T][q(t)] \tag{5.33}$$

where

$$I_g = -\begin{bmatrix} S_1 & \cdots & S_n \end{bmatrix}^T \qquad \bar{\phi} = \begin{bmatrix} \frac{\partial \phi_1(x)}{\partial x} & \cdots & \frac{\partial \phi_n(x)}{\partial x} \end{bmatrix}^T \Bigg|_{x=\alpha H} \tag{5.34a}$$

$$[M] = \begin{bmatrix} M_1 & \cdots & 0 \\ \vdots & \ddots & \vdots \\ 0 & \cdots & M_n \end{bmatrix}; \quad [K] = \begin{bmatrix} \omega_1^2 & \cdots & 0 \\ \vdots & \ddots & \vdots \\ 0 & \cdots & \omega_n^2 \end{bmatrix}[M]; \quad [C] = \begin{bmatrix} 2\xi_1\omega_1 & \cdots & 0 \\ \vdots & \ddots & \vdots \\ 0 & \cdots & 2\xi_n\omega_n \end{bmatrix}[M] \tag{5.34b}$$

It is noted that Eq. 5.13 is the partial differential equation whereas Eq.5.33 is the ordinary differential equation which is much easier to solve compared to Eq. 5.13. The fourth-order Runge-Kutta method is adopted to solve Eq.5.33 in MATLAB environment.

5.2 Ground motion selection

Ground motion (GM) selection is carried out by matching the response spectra of the selected records to a target response spectrum at the site of interest. The ground motion selection is reported in Tesfamariam et al. (2019, 2021b).

A probabilistic seismic hazard analysis (PSHA) tool is used based on Monte Carlo simulations (Atkinson and Goda, 2011) by implementing all major components of the national seismic hazard model (Halchuk et al., 2014). A set of records based on regional seismic hazard characteristics, using multiple-conditional mean spectrum-based record selection method (Goda, 2019), at the anchor period of TA = 2.0 s, 30 records (bi directional) are selected, i.e. 60 unidirectional records. Lower and upper limit vibration periods, T_{min} = 0.1 s and T_{max} = 4.0 s, are considered for the ground motion selection. Fig. 5.6 compares the response spectra of the selected ground motion records with the target spectrum. The match is satisfactory over a wide range of vibration periods from 0.1 s to 4.0 s (Tesfamariam et al., 2021b).

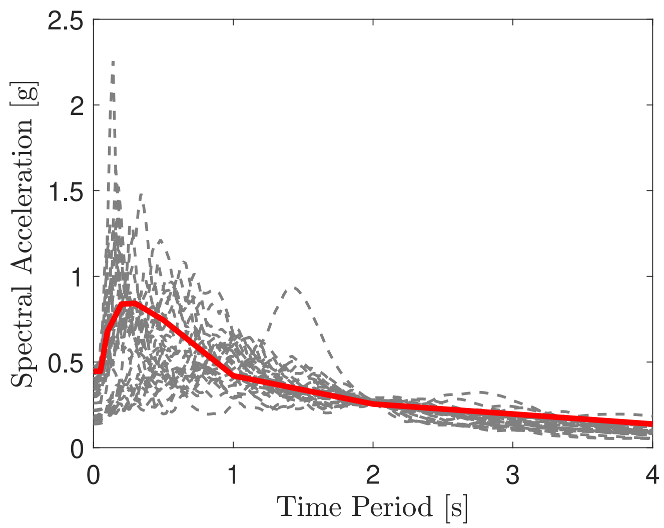

Figure 5.6: Response spectra of selected ground motions and target response spectra for 2% probability of exceedance in 50 years

Chapter 6

Multi-objective Optimization

In general, the multi-objective optimization (MOO) considers a number of objective functions which are aimed to optimize simultaneously. This kind of optimizations becomes essential when conflicted objective functions are taken into consideration. Under this situation, a set of optimal points are obtained instead of one optimal point. These optimal solutions are known as Pareto optimal solutions. Among those Pareto optimal solutions, no optimal solution can be regarded as better solution than any other with respect to all objective functions. The multi-objective optimization can be formulated as

$$
\begin{aligned}
&\text{Minimize / Maximize} \quad && f_i(\mathbf{x}) \qquad\qquad i = 1, 2, \ldots, N_{obj} \\
&\text{Subject to} \quad && : \begin{cases} g_k(\mathbf{x}) = 0, & k = 1, 2, \ldots, K \\ h_l(\mathbf{x}) \leq 0, & l = 1, 2, \ldots, L \\ \mathbf{x}^{(L)} \leq \mathbf{x} \leq \mathbf{x}^{(U)} \end{cases}
\end{aligned}
\tag{6.1}
$$

In the above equation, $f_i(\mathbf{x})$ represents the objective function which is to be minimized or maximized. Also, N_{obj} denotes the total number of objective functions considered in the multi-objective formulation. The optimization may be carried out in presence of constraints or without constraints. In Eq. 6.1, the equality and inequality constraints are denoted by $g_k(\mathbf{x})$ and $h_l(\mathbf{x})$, respectively. Also, the decision variables are represented by $\mathbf{x} = [x_1, x_2, \ldots, x_n]^T$, which are bounded in between lower bound, $\mathbf{x}^{(L)}$ and upper bound, $\mathbf{x}^{(U)}$, respectively. There are many approaches to solve the multi-objective formulation. Among those, classical approach, ϵ- Constraint method are the common and oldest approaches. In classical method, the multi-objective optimization formulation is converted to a single objective optimization problem by choosing some weight factors (Das et al., 2021). However, sometimes this approach does not provide accurate solution as the priori knowledge of the weights are needed. Also, this method is efficient to find the Pareto optimal solutions in non-convex region. This issue can be overcome by using ϵ- Constraint method. However, the bounds in which the search operation is carried out, should be known and thus, this method becomes inefficient for black-box type optimization. For this reason, evolutionary multi-objective optimization is the best option which can able to find pareto optimal points irrespective of shape of Pareto front (i.e. continuous / discontinuous, convex / concave). Evolutionary algorithm uses a population of solutions in every iteration and those are updated in every iteration based on level of information obtained from the iterations. In this chapter, a brief description of Non-dominated Sorting Genetic Algorithm-II (NSGA-II) is presented.

6.1 Non-dominated Sorting Genetic Algorithm-II

Genetic algorithm (GA) is one of the popular evolutionary algorithm which can provide the pareto optimal solutions from a population using a single run of GA. There are numerous variants of GA implemented in the literature for the multi-objective optimization (Deb et al., 2002). Among those, non-dominated sorting genetic algorithm (NSGA), proposed by Deb et al. (2002), is commonly used for the multi-objective optimization. In this study, version 2 of NSGA is used, which is often called NSGA-II. The algorithm starts with generating a population of N individuals, as shown in Fig 6.1(a). It is noted that each randomly generated individual represents the set of decision variables ($\mathbf{x}$) and is encoded in form of chromosome. The values of objective functions are estimated corresponding to each individual. Once function values are obtained, are classified into a number of non-domination level, as shown in Fig. 6.1(b). For example, in Fig. 6.1(b), x_1 and x_2 are said to be non-dominated because function values (f_1 and f_2) at x_1 and x_2 are conflicting i.e. one increases, other decreases. Using this concept, the entire population is categorized into different non-domination level and ranked them accordingly. In Fig. 6.1(b), it is seen that the solutions corresponding to rank 2 are dominated by rank 1. Similarly, solutions corresponding to rank 3 are dominated by rank 2. Thus, rank 1 solutions becomes non-dominated by any other solutions, called pareto optimal solutions, which are stored in every iteration using elitism operator. Non-dominated solution is not only one criteria to obtain final Pareto front, the diversity of non-dominated solution in the population is also checked which is estimated using crowding distance. The crowding distance is defined as Eucleadian distance between each individual on a front, as shown in Fig 6.1(c). Once every individual in a population is ranked and crowding distance is assigned to each individual, NSGA-II selects the individuals with lowest rank. If two individuals having same rank, then the individual with larger crowding distance is selected as a parent, shown in Fig. 6.1(d). Using the parents obtained from the current iteration, offsprings are generated using crossover and mutation operators. The generated offsprings and parent population are combined used as a population for the next iteration, shown in Fig. 6.1(e). The best solutions are selected based on rank and crowding distances. The entire procedure is continued until specified number of generations is achieved. The final Pareto front is shown in Fig. 6.1(f). The pseudo-code of NSGA-II is shown in Algorithm 1.

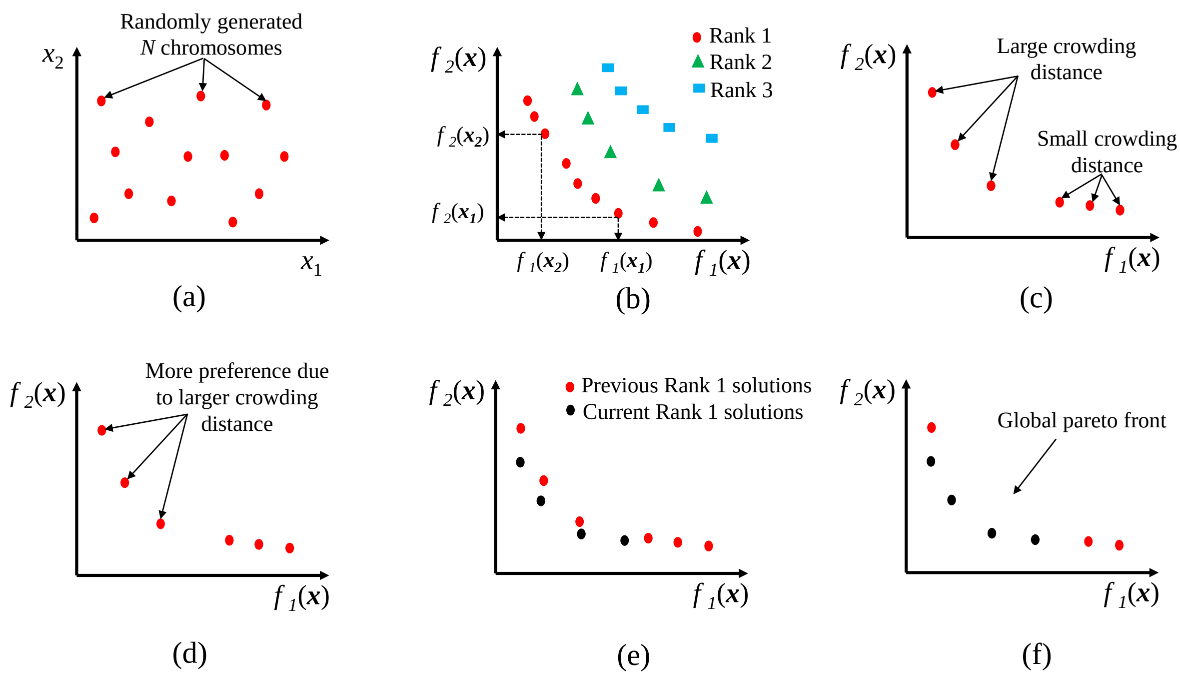

Figure 6.1: Schematic diagram for NSGA-II

6.2 Problem Formulation for MOO

Once the combined structural system with the stochastic ground motions is defined, the location of the outriggers and the tuning parameters are estimated using multi-

Algorithm 1 Pseudo-code for NSGA-II

Initialize parameters related to NSGA-II such as Maximum generations (N_G), Population size (N), Crossover and Mutation percentage and Mutation rate
Generate random population of size N
for $i = 1 : N$ **do**
    Assign rank to individual according to non-dominance criteria
    Calculate crowding distance
end for
for $i = 1 : N_G$ **do**
    Select parents from the population
    Generate N number of offsprings using crossover and mutation
    Assemble parent and offspring population into new population of size $2N$
    for $j = 1 : 2N$ **do**
        Assign rank to individual according to non-dominance criteria
        Calculate crowding distance
    end for
    Generate population of size N, having best rank among $2N$ population
end for
Obtain global pareto front

objective optimization for the optimal performance of the structural system. For this purpose NSGA-II, described in the previous section, is considered. For any high-rise structure, the storey drift and the acceleration of the floors are important, as these performance indices increase with the height of the structure. Thus, the objective functions for the optimization are defined by the following expressions

$$\begin{aligned}
&\min \begin{cases} f_1(\mathbf{x}) = \max\limits_{k\in[1,N]} \left(\frac{1}{N_{sim}} \sum_{i=1}^{N_{sim}} \mathrm{IDR}_{k,i}\right) \\ f_2(\mathbf{x}) = \max\limits_{k\in[1,N]} \left(\frac{1}{N_{sim}} \sum_{i=1}^{N_{sim}} \ddot{u}_i(H_k)\right) \end{cases} \\
&\text{subject to} \begin{cases} \alpha_n - \alpha_{n-1} \geq h/H \\ \alpha_{n-1} - \alpha_{n-2} \geq h/H \\ \vdots \quad \vdots \quad \vdots \\ \alpha_2 - \alpha_1 \geq h/H \end{cases}
\end{aligned} \tag{6.2}$$

In the above equation, IDR represents the inter-storey drift ratio, is expressed as $\{u(H_k,t) - u(H_{k-1},t)\}/\{H_k - H_{k-1}\}$, where $u(H_k,t)$ is the displacement at the height , H_k i.e. floor displacement. Also, N in Eq. 6.2 denotes the total number of floors in the structure. In this study, an ensemble of ground motions (N_{sim}) is considered. The peak value of IDR is calculated for every floor corresponding to each ground motion.

Once the maximum IDR is estimated, the mean IDR is calculated for all floors. The first objective function $f_1(\mathbf{x})$ is taken as the maximum value of mean IDR among all floors. Similarly, the second objective function is considered as the maximum value of mean floor accelerations among all floors, where $\ddot{u}(H_k)$ represents the maximum floor acceleration of storey k. In Eq. 6.2, $\mathbf{x}$ is the design vector which are bounded with lower and upper limits, $\mathbf{x}_{ll}$ and $\mathbf{x}_{ul}$, respectively. Here the design vector is the outrigger location and tuning parameters of SMA. The multi-objective optimization is performed under some constraints when more than one outrigger is considered in the system. The outrigger locations are taken as a constraint where the distance between two consecutive outriggers is greater or equal to storey height (h).

Chapter 7

Numerical Results

In this section, the optimal design of the SMA-based outrigger system is illustrated for earthquake-induced vibration control of timber building. Three different structures with the same plan dimensions i.e. 10-, 15-, and 20-storey are considered for demonstration purposes whose details are provided in Chapter 3. With the obtained member sizes, a multi-objective optimization is performed for SMA-based damped outrigger structures to estimated the optimal locations of outriggers and tuning parameters of SMA.

7.1 Structural responses under different ground motions

Table 7.1: Ground motions used for performance comparison

GM	Name	Year	Magnitude	NGA	Mechanism	V_{S30}(m/s)	Record
1	Big Bear	1992	6.46	902	Strike-slip	345.4	DHP090 DHP360
2	Chi-Chi	1999	7.62	1183	Reverse-oblique	210.7	CHY008-N CHY008-W
3	Düzce	1999	7.14	1602	Strike-slip	326.0	BOL000 BOL090
4	Kobe	1995	6.90	1119	Strike-slip	312.0	TAZ000 TAZ090
5	Northridge	1994	6.69	949	Reverse	297.7	ARL090 ARL360
6	Superstition	1987	6.54	721	Strike-slip	192.1	B-ICC000 B-ICC090

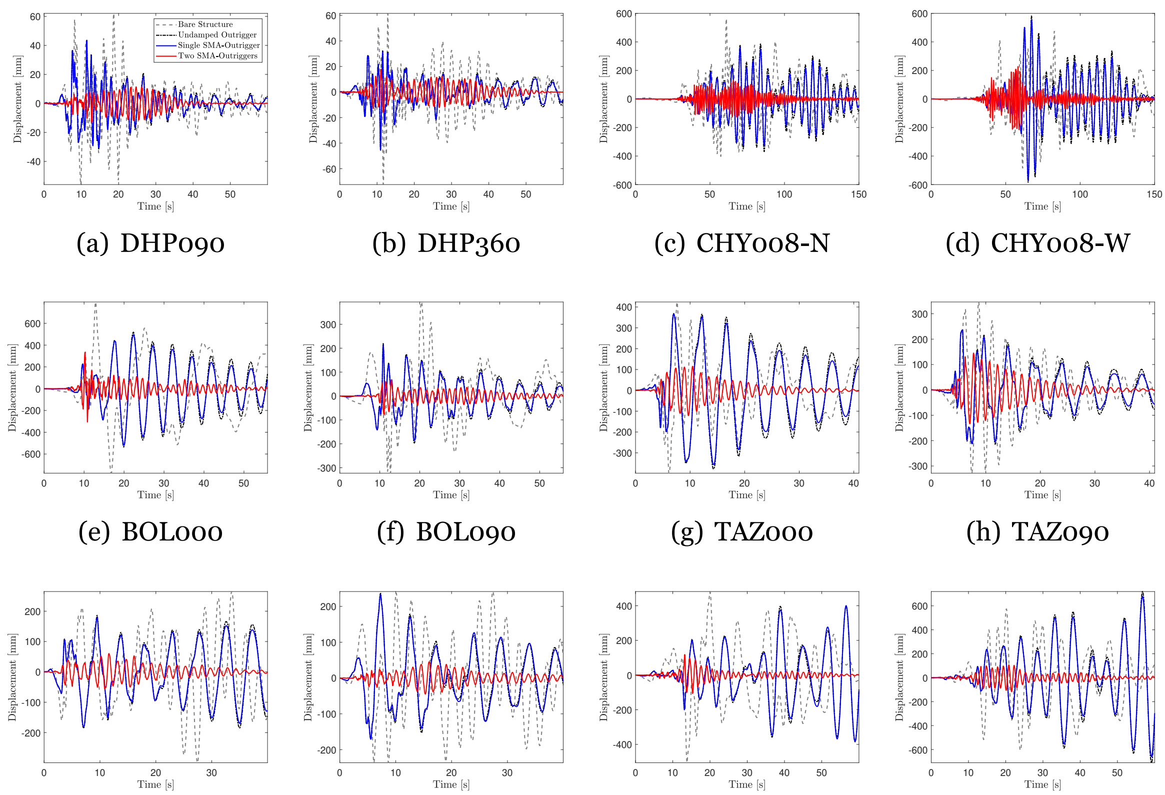

(a) DHP090 (b) DHP360 (c) CHY008-N (d) CHY008-W

(e) BOL000 (f) BOL090 (g) TAZ000 (h) TAZ090

(i) ARL090 (j) ARL360 (k) B-ICC000 (l) B-ICC090

Figure 7.1: Top floor displacement for bare structure, undamped outrigger and SMA-based one and two outrigger system for 20-storey building

Table 7.2: Peak to peak reduction of top floor responses for 20-storey building

Record	Displacement Reduction [%]			Acceleration Reduction [%]		
	Undamped	1-SMA	2-SMA	Undamped	1-SMA	2-SMA
DHP090	29	30	79	14	15	74
DHP360	36	39	75	42	43	77
CHY008-N	31	36	76	23	24	77
CHY008-W	0.01	0.05	53	8	10	67
BOL000	32	35	58	6	7	56
BOL090	44	45	80	1	4	66
TAZ000	11	13	71	19	20	81
TAZ090	31	32	58	13	14	70
ARL090	37	40	80	10	11	71
ARL360	2	4	81	25	27	70
B-ICC000	21	22	76	31	32	71
B-ICC090	1	3	80	10	13	43

* Undamped, 1-SMA and 2-SMA denote structure with undamped outriggers, proposed one and two SMA-outriggers

* The reduction is estimated w.r.t top floor displacement of structure without outrigger

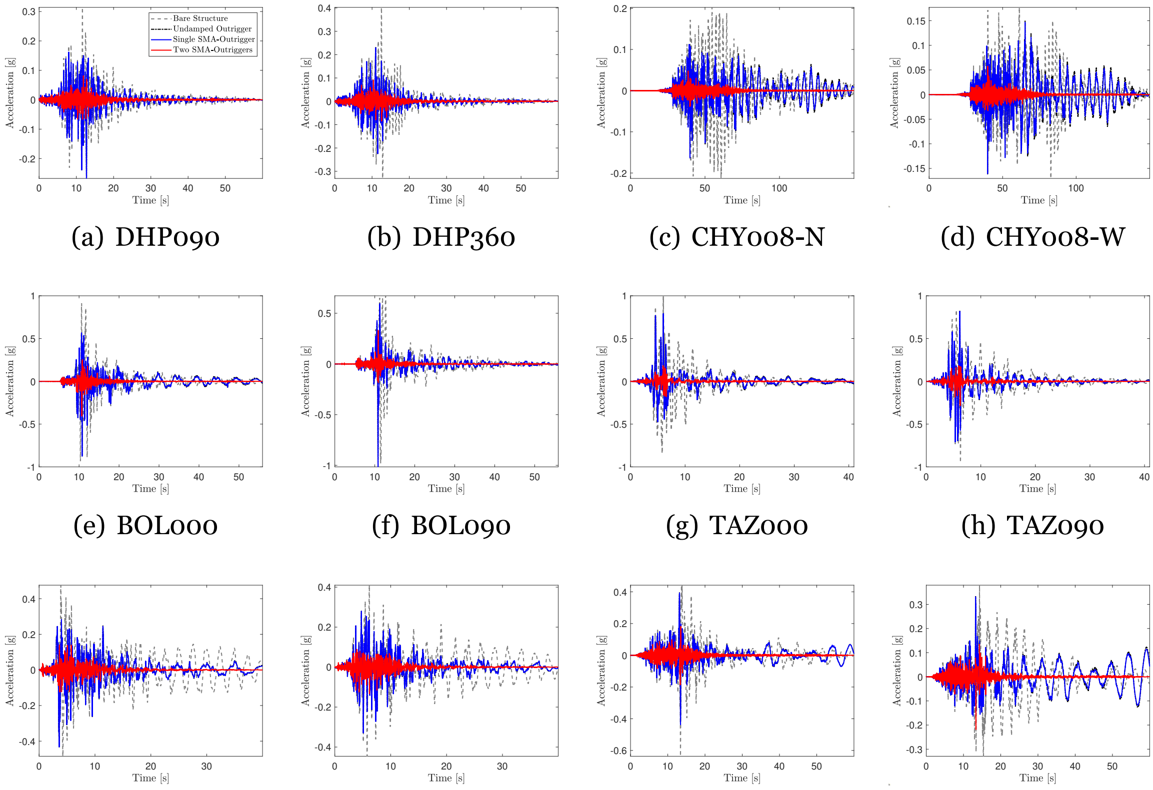

(a) DHP090 (b) DHP360 (c) CHY008-N (d) CHY008-W

(e) BOL000 (f) BOL090 (g) TAZ000 (h) TAZ090

(i) ARL090 (j) ARL360 (k) B-ICC000 (l) B-ICC090

Figure 7.2: Top floor acceleration for bare structure, undamped outrigger and SMA-based one and two outrigger system for 20-storey building

Table 7.3: RMS reduction of top floor responses for 20-storey building

Record	Displacement Reduction			Acceleration Reduction		
	Undamped	1-SMA	2-SMA	Undamped	1-SMA	2-SMA
DHP090	37	40	74	22	23	79
DHP360	41	45	69	38	40	81
CHY008-N	12	22	76	42	47	92
CHY008-W	1	2	71	17	25	90
BOL000	20	29	82	28	30	83
BOL090	40	46	84	41	42	87
TAZ000	3	5	72	41	43	88
TAZ090	19	27	63	26	28	84
ARL090	21	27	82	41	42	83
ARL360	29	31	86	40	42	81
B-ICC000	14	15	87	35	37	82
B-ICC090	0.13	1	85	32	37	86

* RMS : Root mean square

In this section, structural performances with undamped outrigger, proposed SMA-based one and two outrigger system for 20-storey building are shown for different actual ground motion records. Six records with two orthogonal components are considered which are Big Bear (1992), Chi-Chi (1999), Duzce (1999), Kobe (1995), Northridge (1994) and Superstition (1987), represent different earthquake scenarios. The details of the ground motion records are tabulated in Table 7.1. The top floor displacement and top floor acceleration for all records are shown in Fig. 7.1 and Fig. 7.2, respectively. The peak to peak and RMS reduction of displacement and acceleration at top floor are tabulated in Table 7.2 and Table 7.3, respectively. It is seen from the table that SMA-based outrigger can reduce peak as well as RMS responses efficiently.

7.2 Multi-objective optimization of outrigger structure

Once the member sizes are obtained from the gravity load analysis, the reduced-order model for the shear wall with outriggers is derived using Lagrangian formulation. To reduce the loads on the column connecting with the outrigger, a shape memory alloy (SMA) spring is introduced at the junction of the outrigger and column. For ensuring the satisfactory performance of the proposed SMA-based damped outrigger system, multi-objective optimization is carried out to find the optimal location of the outrigger and the tuning parameters of SMA. The prime design parameter is the normalized outrigger location, α which ranges from 0 to 1, as shown in Fig. 5.1. The other design variables are the parameters related to hysteresis of SMA, which are the initial austenite stiffness (k_a), the maximum design displacement ($x_{s,max}$), and the ductility ratio (μ_s) of SMA. Also, the initial austenite stiffness is estimated from normalized transformation strength of SMA, which is $F_0 = k_a x_{ys}/(mH)$, ranges $F_0 \in [0.1, 0.5]$ (Das and Tesfamariam, 2020). The mean value of other parameters $x_{s,max}$ and μ_s are taken as 0.2 m and 20 (Ghodke and Jangid, 2016), respectively. The coefficient of variation of these two variables is assumed to be 20%, which follows a uniform distribution. The bounds are applied to the design parameters to avoid numerical instability during optimization. For this reason, the bounds are taken as $x_{s,max} \in [0.13, 0.27]$ and $\mu_s \in [13, 27]$, respectively.

With these design variables, the multi-objective optimization is performed as described in Section 6.2 considering the maximum inter-storey drift ratio and maximum acceleration among all floors in the objective function. Non-dominated sorting genetic algorithm-II (NSGA-II) is used for multi-objective optimization. The algorithm starts with initializing the size of the population which determines population size at each generation (i.e. in every iteration). In this study, the population size is taken as 100 for every algorithm. The other parameters related to NSGA-II i.e. crossover percentage, mutation percentage, and mutation rate are chosen as 0.7, 0.4, and 0.02, respectively. The stopping criteria for this meta-heuristic algorithm is chosen as the maximum number of iterations i.e. Generations whose value is assumed to be 200. Fig. 7.3 shows the non-dominated solutions obtained using NSGA-II for 10-, 15- and 20-storey timber building considering one outrigger. From Fig. 7.3(a), it is seen that the optimal normalized location of the outrigger is 0.6 for 10-storey building i.e. the optimal location is 60% of the total height of the structure. Also, the maximum floor acceleration is reached up to 0.6g which may lead to non-structural damage. Similarly, for 15- and 20-storey building, the optimal normalized location of the outrigger are found to be 0.62, shown in Fig. 7.3(b) and Fig. 7.3(c), respectively. Here it is seen that the most of non-dominated solutions exceed 2.5% inter-storey drift which is not acceptable in design perspective as according to National Building Code of Canada (NBC, 2015), the maximum acceptable inter-storey drift is 2.5%. For this reason, a two-outriggers system is considered. Fig. 7.4 shows the non-dominated solutions for 10-, 15-, and 20-storey timber buildings considering two outriggers. Here it is seen that in every structure, the inter-storey drift ratio and floor acceleration are reduced compared to a single outrigger system. The optimal locations of the two outriggers for considered three structures are shown in Fig. 7.4. Other optimal values for the tuning parameters related to hysteresis of SMA, i.e., normalized transformation strength, maximum design displacement, and ductility ratio of SMA are found to be 0.47, 0.175 m, and 24.6, respectively.

Once optimal outrigger locations and tuning parameters of SMA are obtained, displacement and acceleration time histories at the top floor are simulated with the optimal values obtained from NSGA-II for bare structure (i.e. without outrigger), undamped and SMA-based one and two outrigger structure, which are shown in Fig. 7.6(a) and Fig. 7.6(b), respectively. Due to the paucity of space, the performance of the proposed system for 20-storey building is shown. In Fig. 7.6(a), the maximum displacement at the top floor is found to be 643 mm for bare structure, whereas the same is obtained as 544 mm for undamped outrigger structure. Using the proposed one and two SMA-based outriggers, the top floor displacements are found to be 475 mm and 289 mm, respectively. Thus, the peak reduction is 16% for undamped

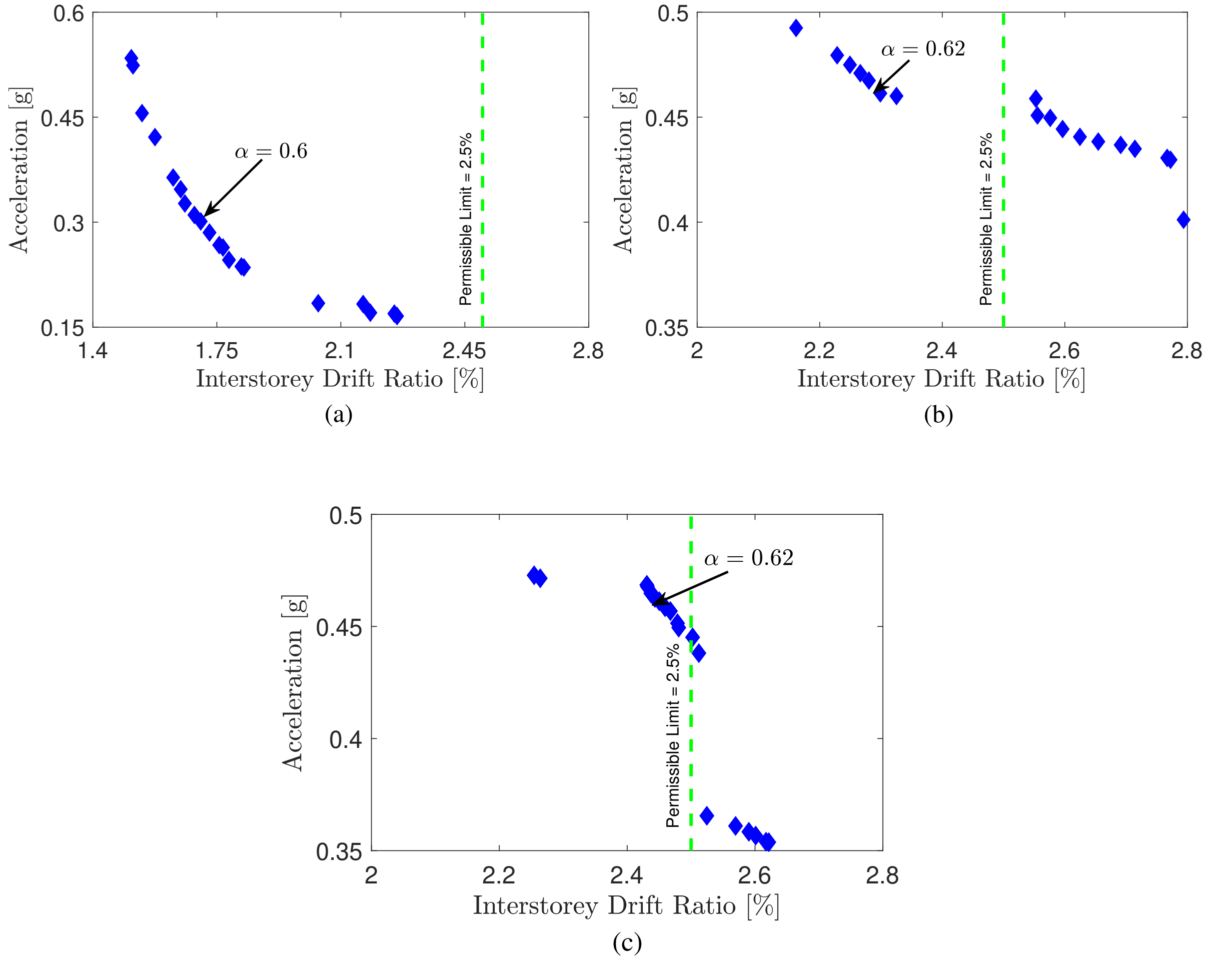

Figure 7.3: Pareto front obtained using NSGA-II for (a) 10-, (b) 15- and (c) 20-storey building with one outrigger

outrigger, whereas with one and two SMA-based outriggers, the peak reductions are 26% and 55%, respectively. The root mean square (rms) reduction is found to be 6% for undamped outrigger, while one and two SMA-based outrigger systems offer 20% and 72% rms reduction, respectively. Similarly, from Fig. 7.6(b), the maximum acceleration of the top floor is 0.39g for bare structure, whereas the same is found to be 0.28g, 0.27g, and 0.12g for undamped, one, and two SMA outriggers, respectively. Thus, peak reductions are obtained as 28%, 31%, and 69%, respectively for undamped, one, and two SMA outrigger structures. The rms reductions are found to be 37%, 42%, and 74%, respectively for all three cases considered in this study. Also, the inter-storey drift ratio and acceleration of all floors are shown in Fig. 7.7. This figure reveals that the proposed two SMA-based outrigger system is much efficient in reducing the inter-storey drift ratio and acceleration of all floors.

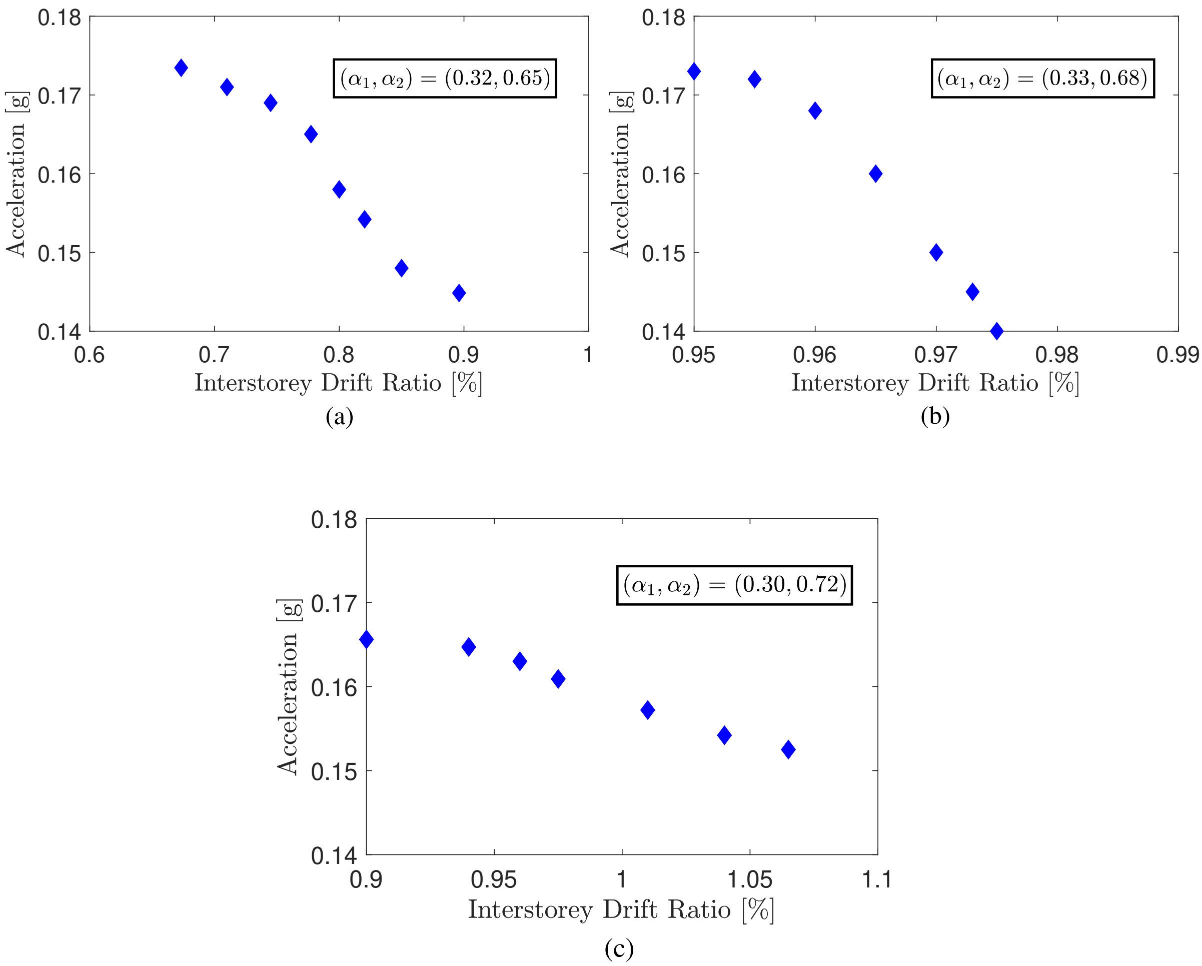

Figure 7.4: Pareto front obtained using NSGA-II for (a) 10-, (b) 15- and (c) 20-storey building with two outriggers

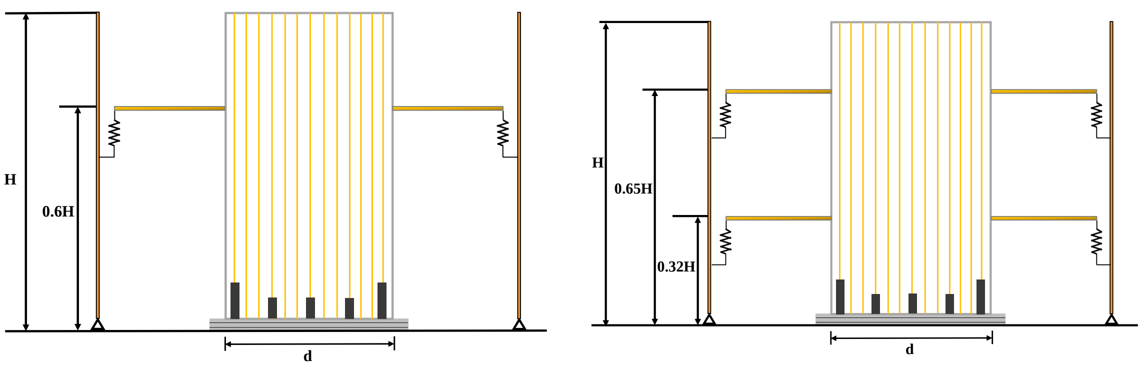

Figure 7.5: Optimal location of outrigger for (a) one and (b) two outrigger system

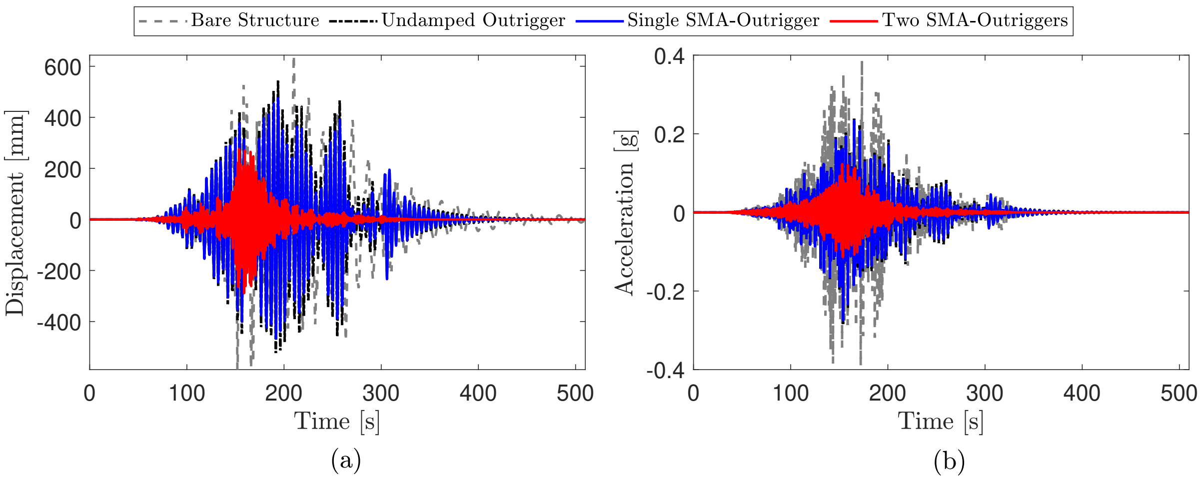

Figure 7.6: Top floor (a) displacement and (b) acceleration time history for bare structure, undamped outrigger and SMA-based one and two outrigger system for 20-storey building

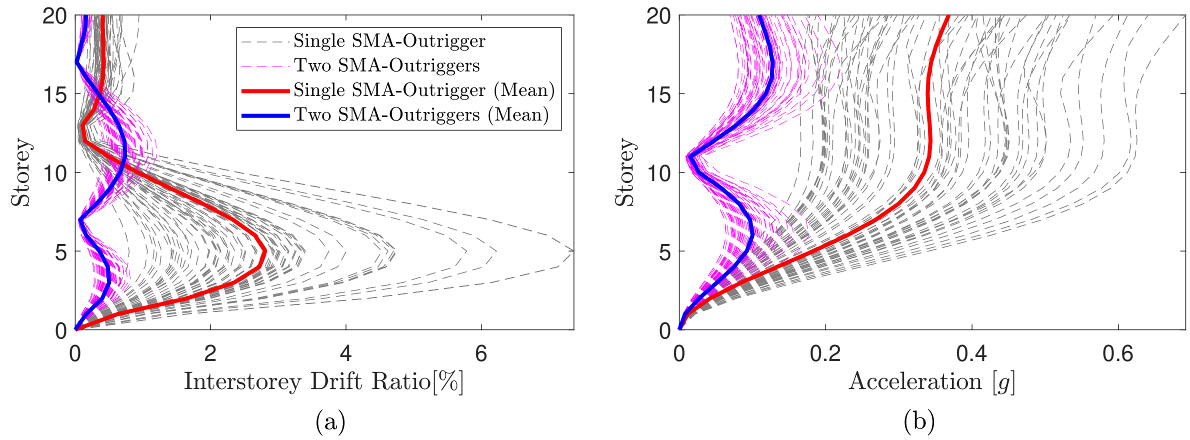

Figure 7.7: Maximum (a) inter-storey drift ratio and (b) acceleration of all floors for one and two SMA-based outriggers for 20-storey building

7.3 Combined outrigger - truss system

Like outrigger beam, in this section, outrigger beam with bracing element is introduced for better energy dissipation under earthquake. With this in view, different configuration for bracing are considered which are X-type bracing, chevron type bracing, V-type bracing and X-type bracing with truss, as shown in Fig. 7.10. A typical section view of combined outrigger - truss system is depicted in Fig. 7.8. To estimate the load demand i.e. forces and moments in beams, columns, core walls and outriggers, ETABS models are used for undamped outrigger - truss system. The

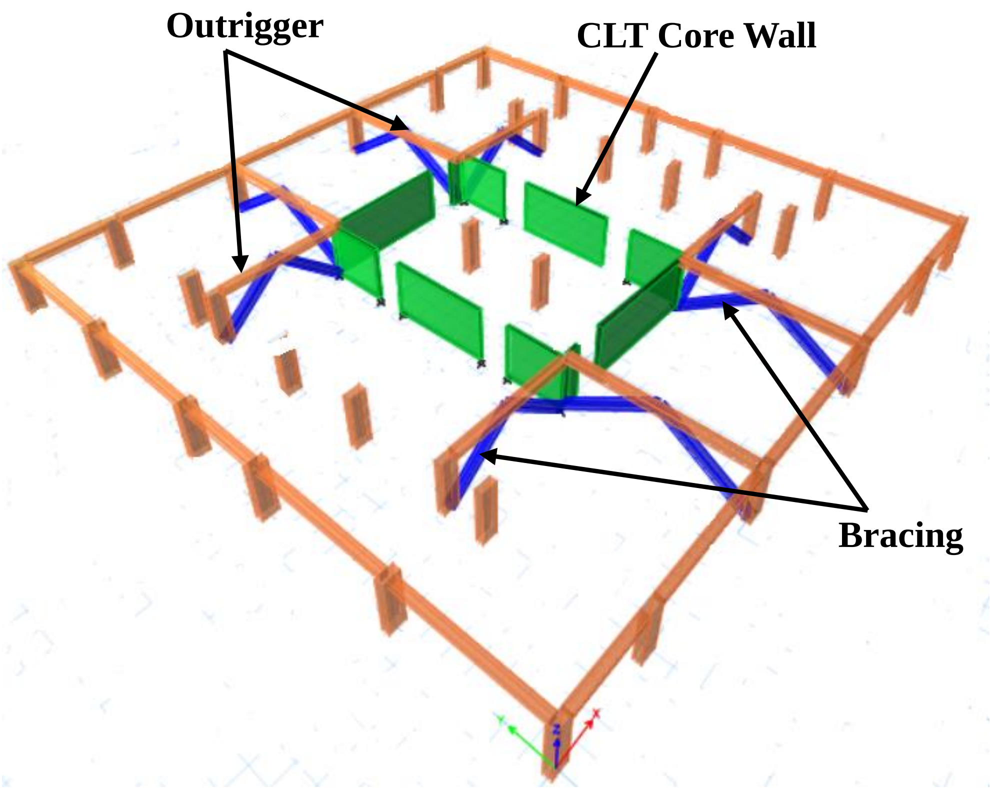

Figure 7.8: Section view of outrigger-truss system

connection between outrigger and wall is assigned as rigid connection whereas the bracing elements are connected with core wall and outrigger by hinge connection. The connection details of the outrigger - truss system are shown in Fig. 7.11. The loads in the members for different configuration of bracing are tabulated in Table 7.4. It is shown that the load demand is decreased while outrigger - truss system is used. As a result, member sizes of beam, column and thickness of core wall will be reduced. The schematic diagram of SMA-based damped outrigger - truss system is shown in Fig. 7.12.

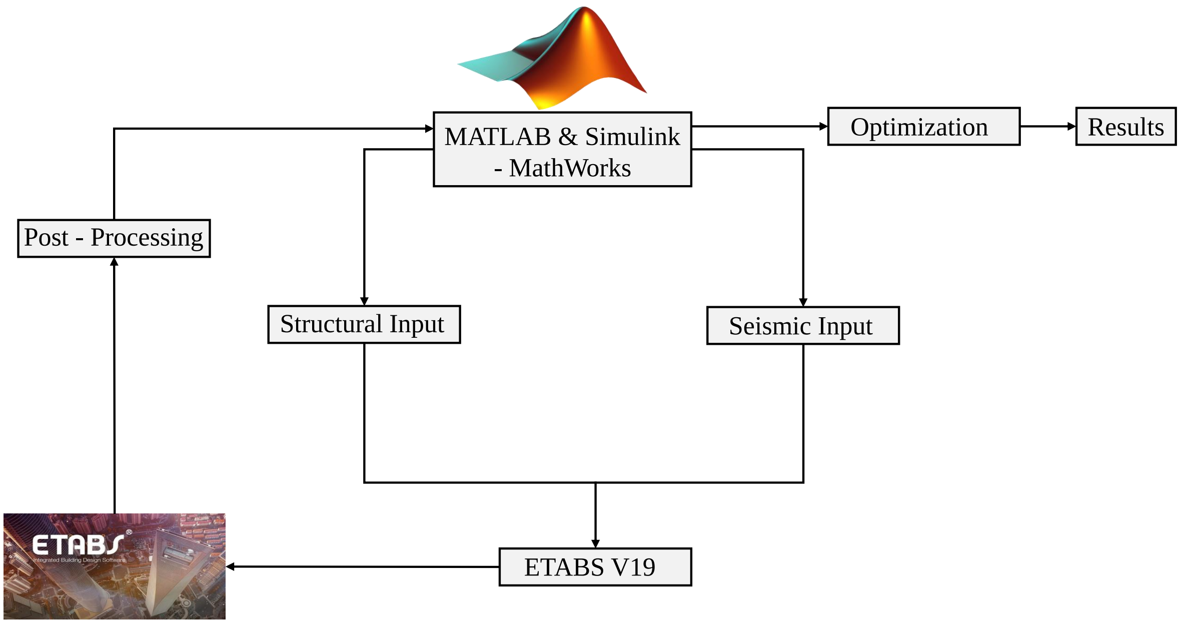

Figure 7.9: Flowchart for optimization using batch mode analysis between MATLAB and ETABS

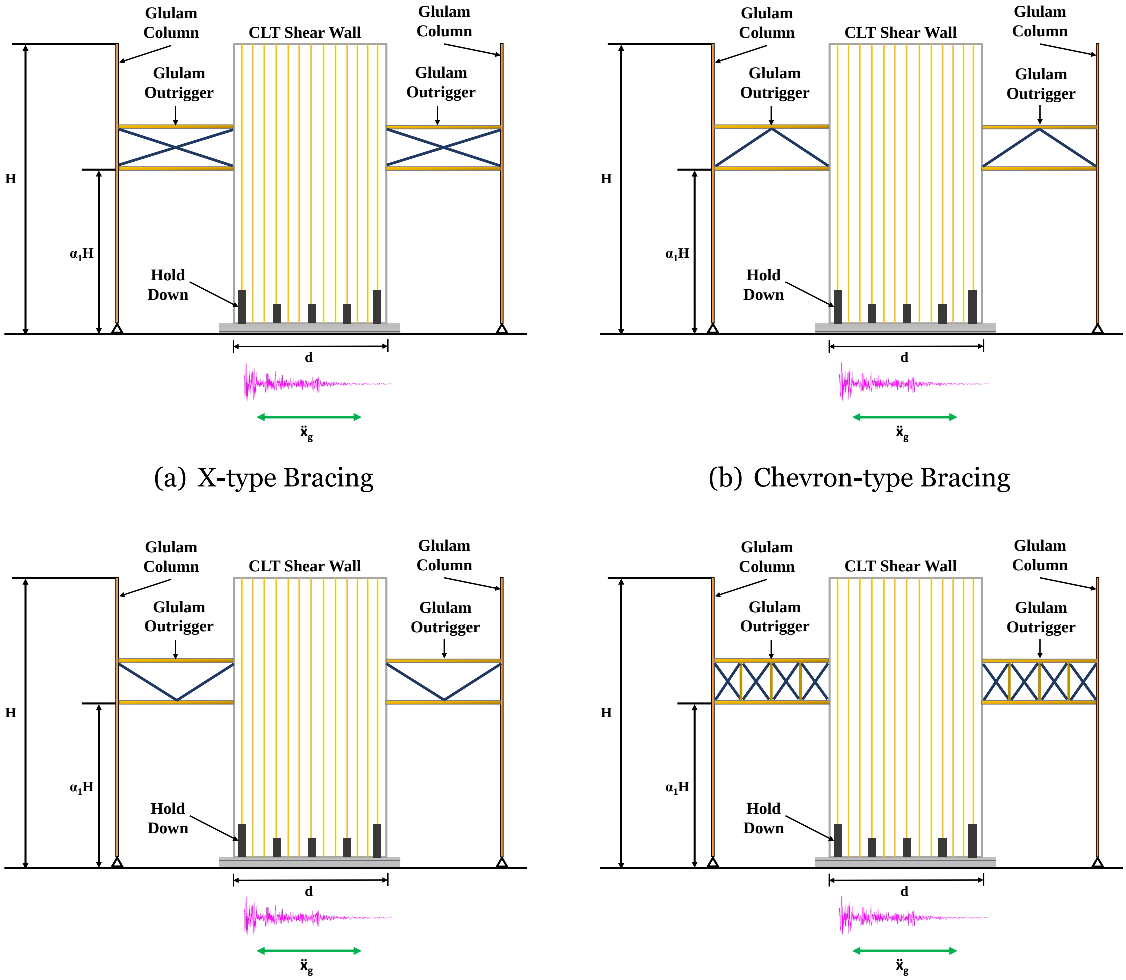

(a) X-type Bracing

(b) Chevron-type Bracing

(c) V-type Bracing

(d) X-type Bracing with Truss

Figure 7.10: Different configuration of undamped outrigger with bracing

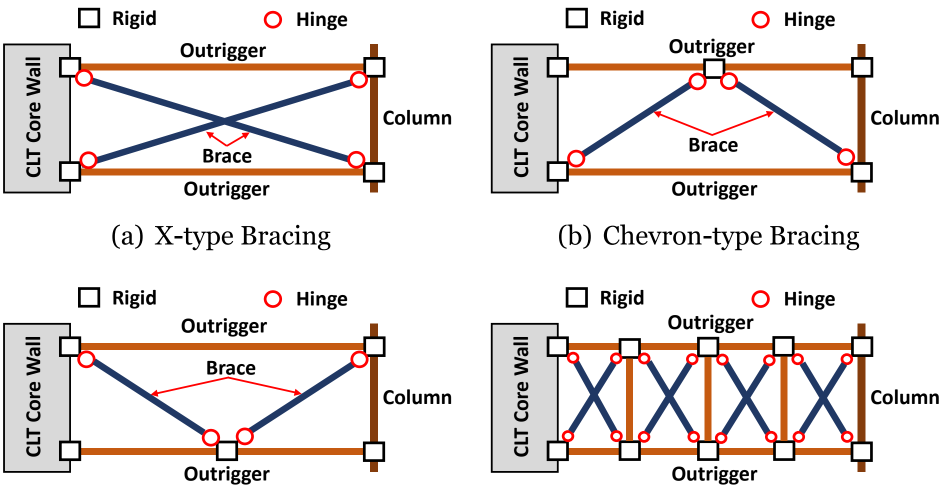

(a) X-type Bracing

(b) Chevron-type Bracing

(c) V-type Bracing

(d) X-type Bracing with Truss

Figure 7.11: Connection details between core, column, outrigger and truss elements

Table 7.4: Maximum member forces and bending moment of various configuration of outrigger-truss structure for 20-storey building

Member	Force	Configuration				
		Outrigger Beam	X-Bracing	Chevron Bracing	V-Bracing	Truss
Beam	Shear Force (kN)	120	120	92	118	41
	Moment (kNm)	140	128	114	122	63
Column	Axial Force(C) (kN)	3650	3403	3378	3387	3286
	Axial Force(T) (kN)	215	370	375	400	437
	Shear Force (kN)	49	58	47	45	66
	Moment (kNm)	157	96	89	94	106
Bracing	Axial Force(C) (kN)	-	760	960	904	577
	Axial Force(T) (kN)	-	730	840	815	478
Core	Axial Force (kN)	7910	7818	7811	7917	7853
	Moment (kNm)	375	338	200	323	199

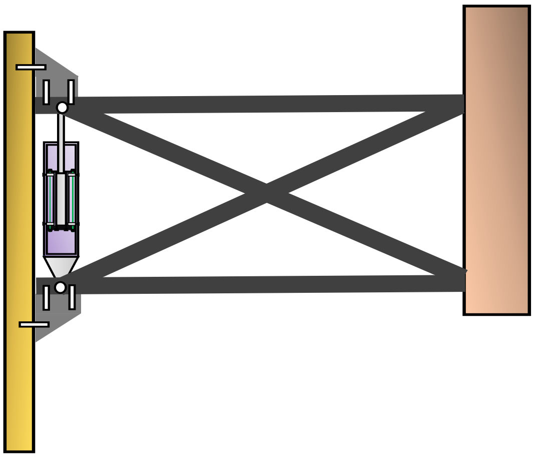

(a) X-type Bracing

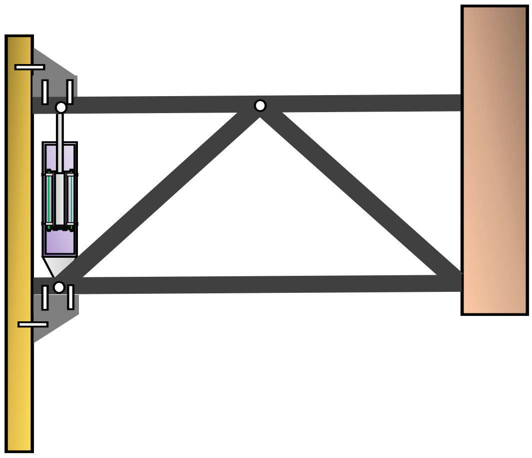

(b) Chevron-type Bracing

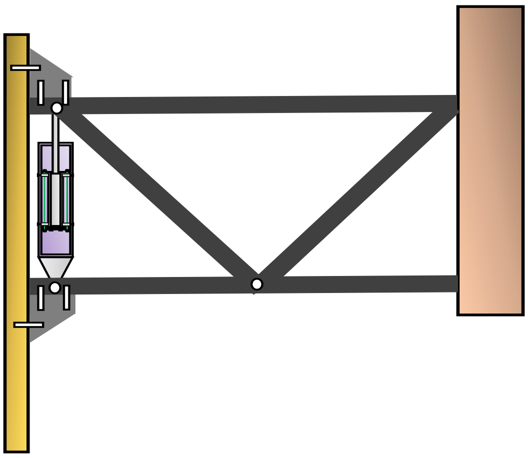

(c) V-type Bracing

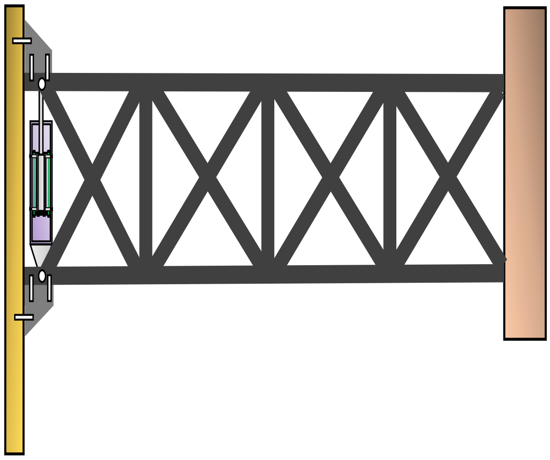

(d) Outrigger Truss

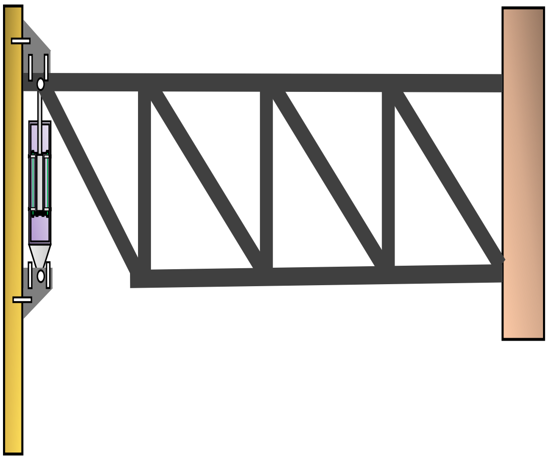

(e) Outrigger Truss

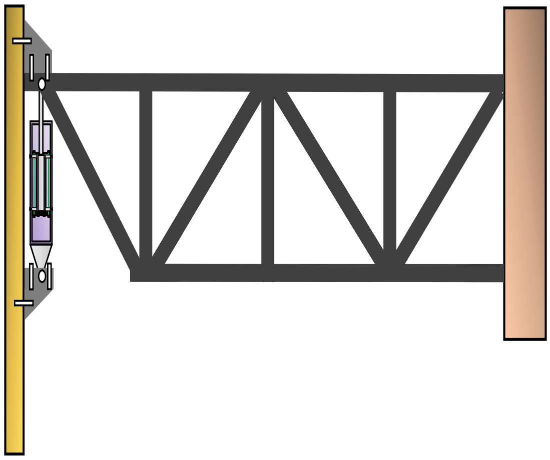

(f) Outrigger Truss

Figure 7.12: Different configuration of outrigger-truss with SMA damper

Chapter 8

Conclusion and Future Work

8.1 Conclusion

This report, theoretically investigates the optimal performance of SMA-based outriggers for the timber structures for mitigating the earthquake-induced vibration. A reduced-order model of the proposed system is developed using Lagrange's approach to study the optimal performance of the system. An ensemble of ground motions are selected based on Vancouver, BC spectrum. Conclusion from Chapter 7 are listed below:

- The numerical results presented in this study clearly show the effectiveness of SMA-based outrigger due to the hysteretic behavior of SMA which enhances the energy absorption capability. It can able to reduce the peak and rms of the inter-storey drift and acceleration of all floors significantly compared to the undamped outrigger system.
- For optimal performance, the location of the outriggers and tuning parameters of SMA are estimated using multi-objective optimization.

8.2 Future Work

In terms of future work, there are many paths to follow:

- The multi-objective optimization of the proposed control system is performed on a reduced-order model of timber building. The works can be further extended for detailed finite element model. For that case, the adopted MOO algorithms will not be useful as multiple of times of computation of model responses are needed which increases computational time. To bypass this, surrogate assisted MOO algorithm will be useful.

- The optimization is carried out by considering uncertainty in ground motions. It is known that timber is composite material whose material property may change. For this case, material uncertainty should be considered while performing optimization, which may yield more realistic results.
- This study does not assess the reliability of the connection between structural members.
- In this report, an overview of outrigger - truss system is introduced considering different configuration of truss system. The exact optimal configuration of truss system should be investigated by using topology optimization where optimal requirement of materials can be estimated considering system uncertainty such as material, geometry uncertainties etc.

Appendix A

Details of Gravity Load Design

A.1 Design details for 10-storey building

The plan dimension is 32.92 × 32.61 m (i.e. 108 × 107 ft), shown in Fig. 3.1. The core of the building is placed symmetrically at centre of the building. The each storey height is 2.95 m (i.e. 9 ft - 8 inch) except the first storey whose height is 3.81 m (i.e. 12 ft - 6 inch) from the ground level. The building is assumed to be located at Vancouver (City Hall), Canada. For this specific site, the parameters related to snow load are taken from National Building Code of Canada (2015). The gravity loads acted on the building are provided in Chapter 3.

A.1.1 Column design

The force in columns are obtained from the ETABS model. Due to pin connection, the axial loads are dominant in the columns, thus bending moment in the columns are less. The design values for column are obtained from ETABS model which are given below:

Table A.1: Maximum design loads in column at first storey

V_f (kN)	$M_{f,x}$ (kN-m)	$M_{f,y}$ (kN-m)	$M_{f,tor}$ (kN-m)	$N_{f,comp}$ (kN)	$N_{f,ten}$ (kN)
88	120	69	0.24	2274	70

Material properties:	
Grade for glulam column is selected as Douglas Fir-Larch 16c-E. The properties of this grade of timber are (Table 7.3 of CSA O86-14) given by	
Modulus of elasticity (E)	: 12400 MPa
Strength in compression parallel to grain (f_c)	: 30.2 MPa
Strength in tension parallel to grain at gross section (f_{tg})	: 15.3 MPa
Strength in bending (f_b)	: 14.0 MPa
Longitudinal shear (f_v)	: 2.0 MPa
Cross-sectional properties:	
Consider, the cross section of D.Fir-L 16c-E glulam column : 315 mm × 1026 mm.	
Area of the column (A = bd)	: 315 × 1026 = 323190 mm^2
Moment of inertia (I)	: $\begin{cases} I_x = \frac{bd^3}{12} = 28.35 \times 10^9\ mm^4 \\ I_y = \frac{b^3d}{12} = 2.67 \times 10^9\ mm^4 \end{cases}$
Section modulus (S)	: $\begin{cases} S_x = \frac{bd^2}{6} = 5.52 \times 10^7\ mm^3 \\ S_y = \frac{b^2d}{6} = 1.69 \times 10^7\ mm^3 \end{cases}$
Design against compression loads:	
Unbraced length of column (L)	: 3.81 m
As the column is pinned supported at both ends,	
Effective length factor (K_e)	: 1.0 (from Table A.6.5.6.1 of CSA O86-14)
Effective length (L_e = K_eL)	: 3.81 m
Slenderness ratio (C_c)	: 3.81/0.315 = 12.09 $<$ 50
According to CSA O86-14 (Cl. 7.5.8.4.2), the factored compressive resistance parallel to grain, $P_r = \phi F_c A K_{Zcg} K_C$.	
ϕ	: 0.8
f_c	: 30.2 MPa
K_D	: 1.0 (from Table 5.3.2.2 of CSA O86-14)
K_H	: 1.0 (Cl. 7.4.2.2 of CSA O86-14)
K_{Sc}	: 1.0 for dry service condition (from Table 7.4.2 of CSA O86-14)
K_{SE}	: 1.0 for dry service condition (from Table 7.4.2 of CSA O86-14)

K_T	: 1.0
$F_c = f_c(K_D K_H K_{Sc} K_T)$	: 30.2 MPa
Z (Volume = Lbd)	: 3.81 $\times$ 0.315 $\times$ 1.026 = 1.2314 m^3
K_{Zcg} (min$\{$0.68 $(Z)^{-0.13}$,1$\}$)	: 0.68 $\times(1.2314)^{-0.13}$ = 0.66

From Cl. 7.5.8.5 of CSA O86-14, the slenderness factor K_C is given by,

$$K_C = \left[1.0 + \frac{F_c K_{Zcg} C_c^3}{35(0.87E) K_{SE} K_T}\right]^{-1} = \left[1.0 + \frac{30.2 \times 0.66 \times 12.09^3}{35 \times (0.87 \times 12400) \times 1.0 \times 1.0}\right]^{-1} = 0.91$$

Therefore, factored compressive resistance is,

$$P_r = 0.8 \times 30.2 \times 323190 \times 0.66 \times 0.91 = 4725.28 \text{ KN} > 2274 \text{ KN(Table A.1)}$$

Design against tensile loads:

According to CSA O86-14 (Cl. 7.5.11), the maximum factored tensile force,

$$T_r = \phi F_{tg} A_g$$

ϕ	: 0.9
f_{tg}	: 15.3 MPa
$F_{tg} = f_{tg}(K_D K_H K_{Sc} K_T)$	: 15.3 MPa
A_g = A	: 323190 mm^2

Therefore, the factored tensile resistance is,

$$T_r = 0.9 \times 15.3 \times 323190 = 4450.33 \text{ kN} > 70 \text{ kN(Table A.1)}$$

Design against bending moment:

According to CSA O86-14 (Cl. 7.5.6.5.1), the factored bending moment resistance, M_r shall be taken as the minimum of M_{r1} or M_{r2}, as follows

$$M_{r1} = \phi F_b S K_X K_{Zbg}$$

$$M_{r2} = \phi F_b S K_X K_L$$

<u>X-X axis:</u>

Φ	: 0.9
$F_b = f_b(K_D K_H K_{Sb} K_T)$	: 14.0 MPa
$S = S_x$	: 5.52×10^7 mm^3

K_X = Curvature factor = 1.0 (Cl. 7.5.6.5.2 of CSA O86-14)

K_{Zbg} = $\left(\frac{130}{b}\right)^{0.1}\left(\frac{610}{d}\right)^{0.1}\left(\frac{9100}{L}\right)^{0.1}$ = $\left(\frac{130}{315}\right)^{0.1}\left(\frac{610}{1026}\right)^{0.1}\left(\frac{9100}{3810}\right)^{0.1}$ = 0.95

C_B (=$\sqrt{L_e d/b^2}$)	: $\sqrt{1.92 * 3810 * 1026/315^2}$ = 8.7 < 10
K_L	: 1.0

The factored moment is,

$$M_{r1} = 0.9 \times 14.0 \times 5.52 \times 10^7 \times 1.0 \times 0.95 = 660.74 \text{ kN-m}$$

$$M_{r2} = 0.9 \times 14.0 \times 5.52 \times 10^7 \times 1.0 \times 1 = 695.52 \text{ kN-m}$$

Factored bending moment resistance (M_r) = 660.74 kN-m $>$ 120 kN-m (Table A.1)

<table>
<tr><td colspan="2"><u>Y-Y axis:</u></td></tr>
<tr><td>Φ</td><td>: 0.9</td></tr>
<tr><td>$F_b = f_b(K_D K_H K_{Sb} K_T)$</td><td>: 14.0 MPa</td></tr>
<tr><td>$S = S_y$</td><td>: 1.69×10^7 mm^3</td></tr>
<tr><td colspan="2">K_X = Curvature factor = 1.0 (Cl. 7.5.6.5.2 of CSA O86-14)</td></tr>
<tr><td colspan="2">K_{Zbg} = $\left(\frac{130}{b}\right)^{0.1}\left(\frac{610}{d}\right)^{0.1}\left(\frac{9100}{L}\right)^{0.1}$ = $\left(\frac{130}{315}\right)^{0.1}\left(\frac{610}{1026}\right)^{0.1}\left(\frac{9100}{3810}\right)^{0.1}$ = 0.95</td></tr>
<tr><td>C_B (=$\sqrt{L_e d/b^2}$)</td><td>: $\sqrt{1.92 * 3810 * 1026/315^2}$ = 8.7 $<$ 10</td></tr>
<tr><td>K_L</td><td>: 1.0</td></tr>
<tr><td colspan="2">The factored moment is,
$$M_{r1} = 0.9 \times 14.0 \times 1.69 \times 10^7 \times 1.0 \times 0.95 = 202.30 \text{ kN-m}$$
$$M_{r2} = 0.9 \times 14.0 \times 1.69 \times 10^7 \times 1.0 \times 1 = 212.94 \text{ kN-m}$$
Factored bending moment resistance (M_r) = 202.30 kN-m $>$ 69 kN-m (Table A.1)</td></tr>
<tr><td colspan="2">Design against combined bending moment and axial load:</td></tr>
<tr><td colspan="2">Members subject to combined bending and compressive or tensile axial loads shall be designed to satisfy the appropriate interaction equation,
$$\left(\frac{P_f}{P_r}\right)^2 + \frac{M_f}{M_r}\left[\frac{1}{1-\frac{P_f}{P_E}}\right] \leq 1$$
$$\frac{T_f}{T_r} + \frac{M_f}{M_r} \leq 1$$</td></tr>
<tr><td>P_f (Compressive load)</td><td>: 2274 kN</td></tr>
<tr><td>P_r (Compressive resistance)</td><td>: 4725.28 kN</td></tr>
<tr><td>M_f (Factored bending moment)</td><td>: $\begin{cases} M_{f,x} = 120 \text{ KN-m} \\ M_{f,y} = 69 \text{ KN-m} \end{cases}$</td></tr>
<tr><td>M_r (Factored bending moment resistance)</td><td>: $\begin{cases} M_{r,x} = 660.74 \text{ KN-m} \\ M_{r,y} = 202.30 \text{ KN-m} \end{cases}$</td></tr>
<tr><td>T_f (Tensile load)</td><td>: 70 KN</td></tr>
<tr><td>T_r (Tensile resistance)</td><td>: 4450.33 KN</td></tr>
<tr><td colspan="2">P_E = Euler buckling load in the plane of the applied moment,
$$\begin{cases} P_{E,x} = \frac{\pi^2 E_{05} K_{SE} K_T I_x}{L_e^2} = 2.08 \times 10^8 \text{ kN} \\ P_{E,y} = \frac{\pi^2 E_{05} K_{SE} K_T I_y}{L_e^2} = 1.96 \times 10^7 \text{ kN} \end{cases}$$
$$\left(\frac{P_f}{P_r}\right)^2 + \frac{M_{f,x}}{M_{r,x}}\left[\frac{1}{1-\frac{P_f}{P_{E,x}}}\right] + \frac{M_{f,y}}{M_{r,y}}\left[\frac{1}{1-\frac{P_f}{P_{E,y}}}\right]$$
$$= \left(\frac{2274}{4725.28}\right)^2 + \frac{120}{660.74}\left[\frac{1}{1-\frac{2274}{2.08\times10^8}}\right] + \frac{69}{202.30}\left[\frac{1}{1-\frac{2274}{1.96\times10^7}}\right] = 0.75 < 1.0$$</td></tr>
</table>

$\frac{T_f}{T_r} + \frac{M_{f,x}}{M_{r,x}} = \frac{70}{4450.33} + \frac{120}{660.74} = 0.20 < 1.0$ $\frac{T_f}{T_r} + \frac{M_{f,y}}{M_{r,y}} = \frac{70}{4450.33} + \frac{69}{202.30} = 0.36 < 1.0$
Design against shear:
According to CSA O86-14 (Cl. 7.5.7.2), the factored shear resistance, V_r is given by $V_r = \phi F_v \frac{2A_g}{3}$ ϕ : 0.9 $F_v = f_v(K_D K_H K_{Sv} K_T)$: 2.0 MPa A_g = A : 323190 mm^2 The factored resistance is, $V_r = 0.9 \times 2.0 \times \frac{2\times323190}{3} = 387.83$ kN > 88 kN
Final cross-section:
Finally, cross-section of D.Fir-L 16c-E glulam column : **315 mm** $\times$ **1026 mm**.

A.1.2 Beam design

The force in beams are obtained from the ETABS model. The design values for beam are given below:

Table A.2: Maximum design loads in beams

V_f (kN)	M_f (kN-m)
32	64

Material properties:
Grade for glulam column is selected as Douglas Fir-Larch 24f-E. The properties of this grade of timber are (Table 7.3 of CSA O86-14) given by Modulus of elasticity (E) : 12800 MPa Strength in bending (f_b) : 30.6 MPa Longitudinal shear (f_v) : 2.0 MPa
Cross-sectional properties:
Consider, the cross section of D.Fir-L 24f-E glulam beam : 175 mm $\times$ 304 mm Area of the column (A = bd) : 175 $\times$ 304 = 53200 mm^2 Moment of inertia (I) : $\begin{cases} I_x = \frac{bd^3}{12} = 409710933\, mm^4 \\ I_y = \frac{b^3d}{12} = 135770833\, mm^4 \end{cases}$ Section modulus (S) : $\begin{cases} S_x = \frac{bd^2}{6} = 2695467\, mm^3 \\ S_y = \frac{b^2d}{6} = 1551667\, mm^3 \end{cases}$

Design against bending moment:
According to CSA O86-14 (Cl. 7.5.6.5.1), the factored bending moment resistance, M_r shall be taken as the minimum of M_{r1} or M_{r2}, as follows $$M_{r1} = \phi F_b S K_X K_{Zbg}$$ $$M_{r2} = \phi F_b S K_X K_L$$ Φ : 0.9 $F_b = f_b(K_D K_H K_{Sb} K_T)$: 30.6 MPa S : 2695467 mm^3 K_X = Curvature factor = 1.0 (Cl. 7.5.6.5.2 of CSA O86-14) K_{Zbg} = $\left(\frac{130}{b}\right)^{0.1}\left(\frac{610}{d}\right)^{0.1}\left(\frac{9100}{L}\right)^{0.1}$ = $\left(\frac{130}{175}\right)^{0.1}\left(\frac{610}{304}\right)^{0.1}\left(\frac{9100}{8839.2}\right)^{0.1}$ = 1.04 C_B (=$\sqrt{L_e d/b^2}$) : $\sqrt{1.92 \times 8839.2 \times 304/175^2}$ = 12.98 $>$ 10 C_K (= $\sqrt{0.97 E K_{SE} K_T/F_b}$) : 20.14 $> C_B$ K_L (=1 - (1/3) $\times$ $(C_B/C_K)^4$) : 0.94 The factored moment is, $$M_{r1} = 0.9 \times 30.6 \times 2695467 \times 1.0 \times 1.04 = 77.20 \text{ KN-m}$$ $$M_{r2} = 0.9 \times 30.6 \times 2695467 \times 1.0 \times 0.94 = 69.78 \text{ KN-m}$$ Factored bending moment resistance (M_r) = 69.78 kN-m $>$ 64.0 kN-m (Table A.2)
Design against shear:
Volume of the section (Z) = $A \times L_{Beam}$ = 0.175 $\times$ 0.304 $\times$ 8.839 = 0.47 $m^3 <$ 2.0 m^3 So, according to CSA O86-14 (Cl. 7.5.7.2), the factored shear resistance, V_r is given by $$V_r = \phi F_v \frac{2A_g}{3}$$ ϕ : 0.9 $F_v = f_v(K_D K_H K_{Sv} K_T)$: 2.0 MPa A_g = A : 53200 mm^2 The factored resistance is, $$V_r = 0.9 \times 2.0 \times \frac{2 \times 53200}{3} = 63.84 \text{ KN} > 32 \text{ KN (From Table A.2)}$$
Final cross-section:
Finally, cross-section of D.Fir-L 24f-E glulam beam : **175 mm** $\times$ **304 mm**.

A.1.3 CLT core wall design

The forces in cross laminated timber (CLT) core wall are obtained from the ETABS model which are given below:

Table A.3: Maximum design loads in core wall for walls in X-Direction

V_f (kN)	$M_{f,x}$ (kN-m)	$M_{f,y}$ (kN-m)	$M_{f,tor}$ (kN-m)	$N_{f,comp}$ (kN)	$N_{f,ten}$ (kN)
1442	238	12629	54	4142	2223

Table A.4: Maximum design loads in core wall for walls in Y-Direction

V_f (kN)	$M_{f,x}$ (kN-m)	$M_{f,y}$ (kN-m)	$M_{f,tor}$ (kN-m)	$N_{f,comp}$ (kN)	$N_{f,ten}$ (kN)
809	150	8856	43	3465	2517

Material properties:

Stress grade for CLT wall is selected as E1. The properties of this grade of CLT are,

Property	Longitudinal layer	Transverse layer
f_b	28.2 MPa	7.0 MPa
E	11700 MPa	9000 MPa
f_t	15.4 MPa	3.2 MPa
f_c	19.3 MPa	9.0 MPa
f_s	0.5 MPa	0.5 MPa
f_{cp}	5.3 MPa	5.3 MPa

Design for CLT walls in X-direction:

Cross-section details:

Consider, 7 layers of CLT of each panel thickness of 35 mm (i.e. 4 longitudinal layers and 3 transverse layers)

Total thickness of wall (h) = 7 × 35 = 245 mm

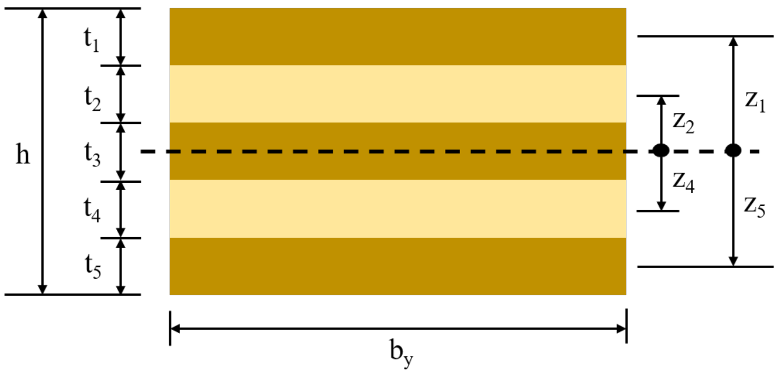

The effective bending stiffness of the panel for the major axis strength axis is given by

$$(EI)_{eff,y} = \sum_{i=1}^{n} E_i \cdot b_y \cdot \frac{t_i^3}{12} + \sum_{i=1}^{n} E_i \cdot b_y \cdot t_i \cdot z_i^2$$

b_y = Width of the panel for the major strength axis = 8839.2 mm

E_i =Modulus of elasticity of laminations in the i-th layer

= 11700 MPa, for laminations in the longitudinal layers

= 9000 MPa, for laminations in the transverse layers

n = Number of layers in the panel = 7

t_i = Thickness of laminations in the i-th layer = 35 mm

z_i = Distance between the center point of the i-th layer and the neutral axis

So, the effective bending stiffness is,

$$
\begin{aligned}
(EI)_{eff,y} = 8839.2 \times \tfrac{(35)^3}{12} \times (4 \times 11700 + 3 \times 9000)+ \\
11700 \times 8839.2 \times 35 \times \left\{ \left(\tfrac{245}{2} - \tfrac{35}{2} \right)^2 + \left(\tfrac{245}{2} - 35 - 35 - \tfrac{35}{2} \right)^2 \right\} \times 2+ \\
9000 \times 8839.2 \times 35 \times \left\{ \left(\tfrac{245}{2} - 35 - \tfrac{35}{2} \right)^2 \right\} \times 2 \\
= 81.29 \times 10^{12} \text{ N-mm}^2
\end{aligned}
$$

Design against compressive loads:

The effective thickness, effective cross-sectional area and the effective out-of-plane moment of inertia are obtained as,

$h_{eff} (= \sum_{i=1}^{(n+1)/2} t_{2n-1})$: $4 \times 35 = 140$ mm

$A_{eff} (= b \cdot h_{eff})$: $8839.2 \times 140 = 1237488$ mm^2

$I_{eff,y} (= \frac{b_y h_{eff}^3}{3})$: $\frac{8839.2 \times 140^3}{12} = 2.02 \times 10^9$ mm^4

The effective radius of gyration, r_{eff} is given by

$$r_{eff} = \sqrt{\frac{I_{eff}}{A_{eff}}} = \sqrt{\frac{2.02 \times 10^9}{1237488}} = 40$$

The slenderness ratio (C_c), the size factor for compression (K_{zc}), the slenderness factor for compression K_c are estimated as

$$C_c = \frac{L_e}{\sqrt{12} r_{eff}} = \frac{3810}{\sqrt{12} \times 40} = 27.21 < 43$$

$$K_{zc} = 6.3 \big(2\sqrt{3} r_{eff} L\big)^{-0.13} = 6.3 \big(2\sqrt{3} \times 40 \times 3810\big)^{-0.13} = 1.13 < 1.3$$

$$K_c = \left[1 + \frac{F_c K_{zc} C_c^3}{35 E_{05} K_{SE} K_T}\right]^{-1} = \left[1 + \frac{f_c (K_D K_H K_{Sc} K_T) K_{zc} C_c^3}{35 E_{05} K_{SE} K_T}\right]^{-1} = \left[1 + \frac{19.3 \times 1 \times 1.13 \times 27.21^3}{35 \times 0.87 \times 11700 \times 1}\right]^{-1} = 0.45$$

Therefore, the factored compressive resistance is,

$$P_r = \phi F_c A_{eff} K_{zc} K_c = 0.8 \times 19.3 \times 1237488 \times 1.13 \times 0.45 = 9683 \text{ kN} > 4142 \text{ kN}$$

Design against bending moment:

The section modulus in the major direction $S_{eff,y}$ is,

$$S_{eff,y} = \frac{(EI)_{eff,y}}{E_1} \cdot \frac{2}{h} = \frac{81.29 \times 10^{12}}{11700} \times \frac{2}{245} = 5.67 \times 10^7 \text{ mm}^3$$

Therefore, the bending resistance is,

$$M_{r,y} = \phi F_b S_{eff,y} K_{rb,y} = 0.9 \times 28.2 \times 5.67 \times 10^7 \times 0.85 = 1224 \text{ kN-m} > 238 \text{ kN-m}$$

Design against combination of axial and bending loads:

CLT panels subject to combined out-of-plane bending and compressive axial load shall be designed to satisfy the interaction equation which is given as

$$\frac{P_f}{P_r} + \frac{M_f}{M_r} \left[\frac{1}{1 - \frac{P_f}{P_{E,v}}} \right] \leq 1$$

The Euler buckling load is given by

$$P_E = \frac{\pi^2 E_{05} I_{eff}}{(K_e L)^2} = \frac{\pi^2 \times 0.87 \times 11700 \times 2.02 \times 10^9}{(3810)^2} = 1.4 \times 10^7 \text{ N}$$

Euler buckling load in the plane of the applied bending moment adjusted for shear deformation is given by

$$P_{E,v} = \frac{P_E}{1+\frac{\kappa P_E}{(GA)_{eff}}} = \frac{1.4\times10^7}{1+\frac{1\times1.4\times10^7}{2.32\times10^9}} = 1.39 \times 10^7 \text{ N}$$

$$\frac{4142}{9683} + \frac{238}{1224}\left[\frac{1}{1-\frac{8182}{1.39\times10^7}}\right] = 0.62 < 1.0$$

Final thickness:

Finally, **245 mm** of thickness of CLT core wall is provided in X direction.

Design for CLT walls in Y-direction:

Cross-section details:

Consider, 5 layers of CLT of each panel thickness of 35 mm (i.e. 3 longitudinal layers and 2 transverse layers)

Total thickness of wall (h) = 5 × 35 = 175 mm

The effective bending stiffness of the panel for the major axis strength axis is given by

$$(EI)_{eff,y} = \sum_{i=1}^{n} E_i \cdot b_y \cdot \frac{t_i^3}{12} + \sum_{i=1}^{n} E_i \cdot b_y \cdot t_i \cdot z_i^2 = 60.54 \times 10^{12} \text{N-mm}^2$$

Design against compressive loads:

The effective thickness, effective cross-sectional area and the effective out-of-plane moment of inertia are obtained as,

$h_{eff}(= \sum_{i=1}^{(n+1)/2} t_{2n-1})$	$: 3 \times 35 = 105$ mm
$A_{eff}(= b \cdot h_{eff})$	$: 14630.4 \times 105 = 1536192$ mm^2
$I_{eff,y}(= \frac{b_y h_{eff}^3}{3})$	$: \frac{14630.4\times105^3}{12} = 1.41 \times 10^9$ mm^4

The effective radius of gyration, r_{eff} is given by

$$r_{eff} = \sqrt{\frac{I_{eff}}{A_{eff}}} = \sqrt{\frac{1.41\times10^9}{1536192}} = 30$$

The slenderness ratio (C_c), the size factor for compression (K_{zc}), the slenderness factor for compression K_c are estimated as

$$C_c = \frac{L_e}{\sqrt{12} r_{eff}} = \frac{3810}{\sqrt{12}\times30} = 36.29 < 43$$

$$K_{zc} = 6.3\big(2\sqrt{3} r_{eff} L\big)^{-0.13} = 6.3\big(2\sqrt{3} \times 40 \times 3810\big)^{-0.13} = 1.18 < 1.3$$

$$K_c = \left[1 + \frac{F_c K_{zc} C_c^3}{35 E_{05} K_{SE} K_T}\right]^{-1} = \left[1 + \frac{f_c(K_D K_H K_{Sc} K_T) K_{zc} C_c^3}{35 E_{05} K_{SE} K_T}\right]^{-1} = \left[1 + \frac{19.3\times1\times1.18\times36.29^3}{35\times0.87\times11700\times1}\right]^{-1} = 0.25$$

Therefore, the factored compressive resistance is,

$$P_r = \phi F_c A_{eff} K_{zc} K_c = 0.8 \times 19.3 \times 1536192 \times 1.18 \times 0.25 = 6900.60 \text{ kN} > 3465 \text{ kN}$$

Design against bending moment:
The section modulus in the major direction $S_{eff,y}$ is, $$S_{eff,y} = \frac{(EI)_{eff,y}}{E_1} \cdot \frac{2}{h} = \frac{81.29 \times 10^{12}}{11700} \times \frac{2}{175} = 5.91 \times 10^7 \text{ mm}^3$$ Therefore, the bending resistance is, $$M_{r,y} = \phi F_b S_{eff,y} K_{rb,y} = 0.9 \times 28.2 \times 5.91 \times 10^7 \times 0.85 = 1276 \text{ kN-m} > 150 \text{ kN-m}$$
Design against combination of axial and bending loads:
CLT panels subject to combined out-of-plane bending and compressive axial load shall be designed to satisfy the interaction equation which is given as $$\frac{P_f}{P_r} + \frac{M_f}{M_r}\left[\frac{1}{1-\frac{P_f}{P_{E,v}}}\right] \leq 1$$ The Euler buckling load is given by $$P_E = \frac{\pi^2 E_{05} I_{eff}}{(K_e L)^2} = \frac{\pi^2 \times 0.87 \times 11700 \times 3.35 \times 10^9}{(3810)^2} = 1.37 \times 10^7 \text{ N}$$ Euler buckling load in the plane of the applied bending moment adjusted for shear deformation is given by $$P_{E,v} = \frac{P_E}{1+\frac{\kappa P_E}{(GA)_{eff}}} = \frac{1.37 \times 10^7}{1+\frac{1 \times 1.37 \times 10^7}{3.83 \times 10^9}} = 1.36 \times 10^7 \text{ N}$$ $$\frac{3465}{6900.60} + \frac{150}{1276}\left[\frac{1}{1-\frac{3465}{1.36 \times 10^7}}\right] = 0.62 < 1.0$$
Final thickness:
Finally, **175 mm** of thickness of CLT core wall is provided in Y direction.

A.2 Design details for 15-storey building

A.2.1 Column design

The force in columns are obtained from the ETABS model. Due to pin connection, the axial loads are dominant in the columns, thus bending moment in the columns are less. The design values for column are obtained from ETABS model which are given below:

Table A.5: Maximum design loads in column at first storey

V_f (kN)	$M_{f,x}$ (kN-m)	$M_{f,y}$ (kN-m)	$M_{f,tor}$ (kN-m)	$N_{f,comp}$ (kN)	$N_{f,ten}$ (kN)
85	116	81	0.26	3207	140

Material properties:	
Grade for glulam column is selected as Douglas Fir-Larch 16c-E. The properties of this grade of timber are (Table 7.3 of CSA O86-14) given by	
Modulus of elasticity (E)	: 12400 MPa
Strength in compression parallel to grain (f_c)	: 30.2 MPa
Strength in tension parallel to grain at gross section (f_{tg})	: 15.3 MPa
Strength in bending (f_b)	: 14.0 MPa
Longitudinal shear (f_v)	: 2.0 MPa
Cross-sectional properties:	
Consider, the cross section of D.Fir-L 16c-E glulam column : 315 mm × 1064 mm.	
Area of the column (A = bd)	: 315 × 1064 = 335160 mm^2
Moment of inertia (I)	: $\begin{cases} I_x = \frac{bd^3}{12} = 31.61 \times 10^9\ mm^4 \\ I_y = \frac{b^3d}{12} = 2.77 \times 10^9\ mm^4 \end{cases}$
Section modulus (S)	: $\begin{cases} S_x = \frac{bd^2}{6} = 5.94 \times 10^7\ mm^3 \\ S_y = \frac{b^2d}{6} = 1.76 \times 10^7\ mm^3 \end{cases}$
Design against compression loads:	
Unbraced length of column (L)	: 3.81 m
As the column is pinned supported at both ends,	
Effective length factor (K_e)	: 1.0 (from Table A.6.5.6.1 of CSA O86-14)
Effective length (L_e = K_eL)	: 3.81 m
Slenderness ratio (C_c)	: 3.81/0.315 = 12.09 $<$ 50
According to CSA O86-14 (Cl. 7.5.8.4.2), the factored compressive resistance parallel to grain, $P_r = \phi F_c A K_{Zcg} K_C$.	
ϕ	: 0.8
f_c	: 30.2 MPa
K_D	: 1.0 (from Table 5.3.2.2 of CSA O86-14)
K_H	: 1.0 (Cl. 7.4.2.2 of CSA O86-14)
K_{Sc}	: 1.0 for dry service condition (from Table 7.4.2 of CSA O86-14)
K_{SE}	: 1.0 for dry service condition (from Table 7.4.2 of CSA O86-14)

K_T	: 1.0
$F_c = f_c(K_D K_H K_{Sc} K_T)$	: 30.2 MPa
Z (Volume = Lbd)	: 3.81 $\times$ 0.315 $\times$ 1.064 = 1.277 m^3
K_{Zcg} (min$\{$0.68 $(Z)^{-0.13}$,1$\}$)	: 0.68 $\times (1.277)^{-0.13}$ = 0.66

From Cl. 7.5.8.5 of CSA O86-14, the slenderness factor K_C is given by,

$$K_C = \left[1.0 + \frac{F_c K_{Zcg} C_c^3}{35(0.87E) K_{SE} K_T}\right]^{-1} = \left[1.0 + \frac{30.2 \times 0.66 \times 12.09^3}{35 \times (0.87 \times 12400) \times 1.0 \times 1.0}\right]^{-1} = 0.91$$

Therefore, factored compressive resistance is,

$$P_r = 0.8 \times 30.2 \times 335160 \times 0.66 \times 0.91 = 4879.15 \text{ KN} > 3207 \text{ KN(Table A.5)}$$

Design against tensile loads:

According to CSA O86-14 (Cl. 7.5.11), the maximum factored tensile force ,

$$T_r = \phi F_{tg} A_g$$

ϕ	: 0.9
f_{tg}	: 15.3 MPa
$F_{tg} = f_{tg}(K_D K_H K_{Sc} K_T)$	: 15.3 MPa
A_g = A	: 335160 mm^2

Therefore, the factored tensile resistance is,

$$T_r = 0.9 \times 15.3 \times 335160 = 4615.15 \text{ kN} > 140 \text{ kN(Table A.5)}$$

Design against bending moment:

According to CSA O86-14 (Cl. 7.5.6.5.1), the factored bending moment resistance, M_r shall be taken as the minimum of M_{r1} or M_{r2}, as follows

$$M_{r1} = \phi F_b S K_X K_{Zbg}$$

$$M_{r2} = \phi F_b S K_X K_L$$

X-X axis:

Φ	: 0.9
$F_b = f_b(K_D K_H K_{Sb} K_T)$	: 14.0 MPa
$S = S_x$	: 5.94×10^7 mm^3

K_X = Curvature factor = 1.0 (Cl. 7.5.6.5.2 of CSA O86-14)

K_{Zbg} = $\left(\frac{130}{b}\right)^{0.1}\left(\frac{610}{d}\right)^{0.1}\left(\frac{9100}{L}\right)^{0.1}$ = $\left(\frac{130}{315}\right)^{0.1}\left(\frac{610}{1064}\right)^{0.1}\left(\frac{9100}{3810}\right)^{0.1}$ = 0.94

C_B (=$\sqrt{L_e d/b^2}$)	: $\sqrt{1.92 * 3810 * 1064/315^2}$ = 8.86 $<$ 10
K_L	: 1.0

The factored moment is,

$$M_{r1} = 0.9 \times 14.0 \times 5.94 \times 10^7 \times 1.0 \times 0.94 = 703.53 \text{ kN-m}$$

$$M_{r2} = 0.9 \times 14.0 \times 5.94 \times 10^7 \times 1.0 \times 1 = 748.44 \text{ kN-m}$$

Factored bending moment resistance (M_r) = 703.53 kN-m $>$ 116 kN-m (Table A.5)

Y-Y axis:	
Φ	: 0.9
$F_b = f_b(K_D K_H K_{Sb} K_T)$	: 14.0 MPa
$S = S_y$	: 1.76×10^7 mm^3

K_X = Curvature factor = 1.0 (Cl. 7.5.6.5.2 of CSA O86-14)

$K_{Zbg} = \left(\frac{130}{b}\right)^{0.1}\left(\frac{610}{d}\right)^{0.1}\left(\frac{9100}{L}\right)^{0.1} = \left(\frac{130}{315}\right)^{0.1}\left(\frac{610}{1064}\right)^{0.1}\left(\frac{9100}{3810}\right)^{0.1} = 0.94$

C_B (=$\sqrt{L_e d/b^2}$)	: $\sqrt{1.92 * 3810 * 1064/315^2} = 8.86 < 10$
K_L	: 1.0

The factored moment is,

$$M_{r1} = 0.9 \times 14.0 \times 1.76 \times 10^7 \times 1.0 \times 0.94 = 209.41 \text{ kN-m}$$

$$M_{r2} = 0.9 \times 14.0 \times 1.76 \times 10^7 \times 1.0 \times 1 = 223 \text{ kN-m}$$

Factored bending moment resistance (M_r) = 209.41 kN-m > 81 kN-m (Table A.5)

Design against combined bending moment and axial load:

Members subject to combined bending and compressive or tensile axial loads shall be designed to satisfy the appropriate interaction equation,

$$\left(\frac{P_f}{P_r}\right)^2 + \frac{M_f}{M_r}\left[\frac{1}{1-\frac{P_f}{P_E}}\right] \leq 1$$

$$\frac{T_f}{T_r} + \frac{M_f}{M_r} \leq 1$$

P_f (Compressive load)	: 3207 kN
P_r (Compressive resistance)	: 4879.15 kN
M_f (Factored bending moment)	: $\begin{cases} M_{f,x} = 116 \text{ KN-m} \\ M_{f,y} = 81 \text{ KN-m} \end{cases}$
M_r (Factored bending moment resistance)	: $\begin{cases} M_{r,x} = 703.53 \text{ KN-m} \\ M_{r,y} = 209.41 \text{ KN-m} \end{cases}$
T_f (Tensile load)	: 140 KN
T_r (Tensile resistance)	: 4615.15 KN

P_E = Euler buckling load in the plane of the applied moment,

$$\begin{cases} P_{E,x} = \frac{\pi^2 E_{05} K_{SE} K_T I_x}{L_e^2} = 2.32 \times 10^8 \text{ kN} \\ P_{E,y} = \frac{\pi^2 E_{05} K_{SE} K_T I_y}{L_e^2} = 2.03 \times 10^7 \text{ kN} \end{cases}$$

$$\left(\frac{P_f}{P_r}\right)^2 + \frac{M_{f,x}}{M_{r,x}}\left[\frac{1}{1-\frac{P_f}{P_{E,x}}}\right] + \frac{M_{f,y}}{M_{r,y}}\left[\frac{1}{1-\frac{P_f}{P_{E,y}}}\right]$$

$$= \left(\frac{3207}{4879.15}\right)^2 + \frac{116}{703.53}\left[\frac{1}{1-\frac{3207}{2.32\times10^8}}\right] + \frac{81}{209.41}\left[\frac{1}{1-\frac{3207}{2.03\times10^7}}\right] = 0.98 < 1.0$$

$\frac{T_f}{T_r} + \frac{M_{f,x}}{M_{r,x}} = \frac{140}{4615.15} + \frac{116}{703.53} = 0.19 < 1.0$ $\frac{T_f}{T_r} + \frac{M_{f,y}}{M_{r,y}} = \frac{140}{4615.15} + \frac{81}{209.41} = 0.42 < 1.0$
Design against shear:
According to CSA O86-14 (Cl. 7.5.7.2), the factored shear resistance, V_r is given by $V_r = \phi F_v \frac{2A_g}{3}$ ϕ : 0.9 $F_v = f_v(K_D K_H K_{Sv} K_T)$: 2.0 MPa A_g = A : 335160 mm^2 The factored resistance is, $V_r = 0.9 \times 2.0 \times \frac{2\times335160}{3} = 402.19$ kN > 85 kN
Final cross-section:
Finally, cross-section of D.Fir-L 16c-E glulam column : **315 mm** $\times$ **1064 mm**.

A.2.2 Beam design

The force in beams are obtained from the ETABS model. The design values for beam are given below:

Table A.6: Maximum design loads in beams

V_f (kN)	M_f (kN-m)
32	64

Material properties:
Grade for glulam column is selected as Douglas Fir-Larch 24f-E. The properties of this grade of timber are (Table 7.3 of CSA O86-14) given by Modulus of elasticity (E) : 12800 MPa Strength in bending (f_b) : 30.6 MPa Longitudinal shear (f_v) : 2.0 MPa
Cross-sectional properties:
Consider, the cross section of D.Fir-L 24f-E glulam beam : 175 mm $\times$ 304 mm Area of the column (A = bd) : 175 $\times$ 304 = 53200 mm^2 Moment of inertia (I) : $\begin{cases} I_x = \frac{bd^3}{12} = 409710933\ mm^4 \\ I_y = \frac{b^3d}{12} = 135770833\ mm^4 \end{cases}$ Section modulus (S) : $\begin{cases} S_x = \frac{bd^2}{6} = 2695467\ mm^3 \\ S_y = \frac{b^2d}{6} = 1551667\ mm^3 \end{cases}$

Design against bending moment:	
According to CSA O86-14 (Cl. 7.5.6.5.1), the factored bending moment resistance, M_r shall be taken as the minimum of M_{r1} or M_{r2}, as follows	
$$M_{r1} = \phi F_b S K_X K_{Zbg}$$ $$M_{r2} = \phi F_b S K_X K_L$$	
Φ	: 0.9
$F_b = f_b(K_D K_H K_{Sb} K_T)$	: 30.6 MPa
S	: 2695467 mm^3
K_X = Curvature factor = 1.0 (Cl. 7.5.6.5.2 of CSA O86-14)	
K_{Zbg} = $\left(\frac{130}{b}\right)^{0.1}\left(\frac{610}{d}\right)^{0.1}\left(\frac{9100}{L}\right)^{0.1}$ = $\left(\frac{130}{175}\right)^{0.1}\left(\frac{610}{304}\right)^{0.1}\left(\frac{9100}{8839.2}\right)^{0.1}$ = 1.04	
C_B (=$\sqrt{L_e d/b^2}$)	: $\sqrt{1.92 \times 8839.2 \times 304/175^2}$ = 12.98 $>$ 10
C_K (= $\sqrt{0.97 E K_{SE} K_T/F_b}$)	: 20.14 $> C_B$
K_L (=1 - (1/3) $\times$ $(C_B/C_K)^4$)	: 0.94
The factored moment is,	
$$M_{r1} = 0.9 \times 30.6 \times 2695467 \times 1.0 \times 1.04 = 77.20 \text{ KN-m}$$ $$M_{r2} = 0.9 \times 30.6 \times 2695467 \times 1.0 \times 0.94 = 69.78 \text{ KN-m}$$	
Factored bending moment resistance (M_r) = 69.78 kN-m $>$ 64.0 kN-m (Table A.6)	
Design against shear:	
Volume of the section (Z) = $A \times L_{Beam}$ = 0.175 $\times$ 0.304 $\times$ 8.839 = 0.47 m^3 $<$ 2.0 m^3	
So, according to CSA O86-14 (Cl. 7.5.7.2), the factored shear resistance, V_r is given by	
$$V_r = \phi F_v \frac{2A_g}{3}$$	
ϕ	: 0.9
$F_v = f_v(K_D K_H K_{Sv} K_T)$	: 2.0 MPa
A_g = A	: 53200 mm^2
The factored resistance is,	
$$V_r = 0.9 \times 2.0 \times \frac{2 \times 53200}{3} = 63.84 \text{ KN} > 32 \text{ KN (From Table A.6)}$$	
Final cross-section:	
Finally, cross-section of D.Fir-L 24f-E glulam beam : **175 mm** $\times$ **304 mm**.	

A.2.3 CLT core wall design

The forces in cross laminated timber (CLT) core wall are obtained from the ETABS model which are given below:

Table A.7: Maximum design loads in core wall for walls in X-Direction

V_f (kN)	$M_{f,x}$ (kN-m)	$M_{f,y}$ (kN-m)	$M_{f,tor}$ (kN-m)	$N_{f,comp}$ (kN)	$N_{f,ten}$ (kN)
1610	242	16165	55	6440	3467

Table A.8: Maximum design loads in core wall for walls in Y-Direction

V_f (kN)	$M_{f,x}$ (kN-m)	$M_{f,y}$ (kN-m)	$M_{f,tor}$ (kN-m)	$N_{f,comp}$ (kN)	$N_{f,ten}$ (kN)
881	169	10465	48	4885	3488

Material properties:

Stress grade for CLT wall is selected as E1. The properties of this grade of CLT are,

Property	Longitudinal layer	Transverse layer
f_b	28.2 MPa	7.0 MPa
E	11700 MPa	9000 MPa
f_t	15.4 MPa	3.2 MPa
f_c	19.3 MPa	9.0 MPa
f_s	0.5 MPa	0.5 MPa
f_{cp}	5.3 MPa	5.3 MPa

Design for CLT walls in X-direction:

Cross-section details:

Consider, 7 layers of CLT of each panel thickness of 35 mm (i.e. 4 longitudinal layers and 3 transverse layers)

Total thickness of wall (h) = 7 $\times$ 35 = 245 mm

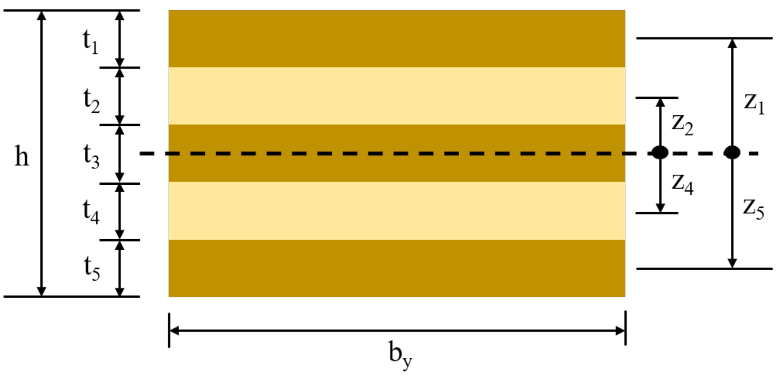

The effective bending stiffness of the panel for the major axis strength axis is given by

$$(EI)_{eff,y} = \sum_{i=1}^{n} E_i \cdot b_y \cdot \frac{t_i^3}{12} + \sum_{i=1}^{n} E_i \cdot b_y \cdot t_i \cdot z_i^2$$

b_y = Width of the panel for the major strength axis = 8839.2 mm

E_i =Modulus of elasticity of laminations in the i-th layer

= 11700 MPa, for laminations in the longitudinal layers

= 9000 MPa, for laminations in the transverse layers

n = Number of layers in the panel = 7

t_i = Thickness of laminations in the i-th layer = 35 mm

z_i = Distance between the center point of the i-th layer and the neutral axis

So, the effective bending stiffness is,

$$(EI)_{eff,y} = 8839.2 \times \frac{(35)^3}{12} \times (4 \times 11700 + 3 \times 9000) + 11700 \times 8839.2 \times 35 \times \left\{\left(\frac{245}{2} - \frac{35}{2}\right)^2 + \left(\frac{245}{2} - 35 - 35 - \frac{35}{2}\right)^2\right\} \times 2 + 9000 \times 8839.2 \times 35 \times \left\{\left(\frac{245}{2} - 35 - \frac{35}{2}\right)^2\right\} \times 2 = 81.29 \times 10^{12} \text{ N-mm}^2$$

Design against compressive loads:

The effective thickness, effective cross-sectional area and the effective out-of-plane moment of inertia are obtained as,

$h_{eff}(= \sum_{i=1}^{(n+1)/2} t_{2n-1})$: $4 \times 35 = 140$ mm

$A_{eff}(= b \cdot h_{eff})$: $8839.2 \times 140 = 1237488$ mm^2

$I_{eff,y}(= \frac{b_y h_{eff}^3}{3})$: $\frac{8839.2 \times 140^3}{12} = 2.02 \times 10^9$ mm^4

The effective radius of gyration, r_{eff} is given by

$$r_{eff} = \sqrt{\frac{I_{eff}}{A_{eff}}} = \sqrt{\frac{2.02 \times 10^9}{1237488}} = 40$$

The slenderness ratio (C_c), the size factor for compression (K_{zc}), the slenderness factor for compression K_c are estimated as

$$C_c = \frac{L_e}{\sqrt{12} r_{eff}} = \frac{3810}{\sqrt{12 \times 40}} = 27.21 < 43$$

$$K_{zc} = 6.3\big(2\sqrt{3} r_{eff} L\big)^{-0.13} = 6.3\big(2\sqrt{3} \times 40 \times 3810\big)^{-0.13} = 1.13 < 1.3$$

$$K_c = \left[1 + \frac{F_c K_{zc} C_c^3}{35 E_{05} K_{SE} K_T}\right]^{-1} = \left[1 + \frac{f_c (K_D K_H K_{Sc} K_T) K_{zc} C_c^3}{35 E_{05} K_{SE} K_T}\right]^{-1} = \left[1 + \frac{19.3 \times 1 \times 1.13 \times 27.21^3}{35 \times 0.87 \times 11700 \times 1}\right]^{-1} = 0.45$$

Therefore, the factored compressive resistance is,

$$P_r = \phi F_c A_{eff} K_{zc} K_c = 0.8 \times 19.3 \times 1237488 \times 1.13 \times 0.45 = 9683 \text{ kN} > 6440 \text{ kN}$$

Design against bending moment:

The section modulus in the major direction $S_{eff,y}$ is,

$$S_{eff,y} = \frac{(EI)_{eff,y}}{E_1} \cdot \frac{2}{h} = \frac{81.29 \times 10^{12}}{11700} \times \frac{2}{245} = 5.67 \times 10^7 \text{ mm}^3$$

Therefore, the bending resistance is,

$$M_{r,y} = \phi F_b S_{eff,y} K_{rb,y} = 0.9 \times 28.2 \times 5.67 \times 10^7 \times 0.85 = 1224 \text{ kN-m} > 242 \text{ kN-m}$$

Design against combination of axial and bending loads:

CLT panels subject to combined out-of-plane bending and compressive axial load shall be designed to satisfy the interaction equation which is given as

$$\frac{P_f}{P_r} + \frac{M_f}{M_r}\left[\frac{1}{1 - \frac{P_f}{P_{E,v}}}\right] \leq 1$$

The Euler buckling load is given by

$$P_E = \frac{\pi^2 E_{05} I_{eff}}{(K_e L)^2} = \frac{\pi^2 \times 0.87 \times 11700 \times 2.02 \times 10^9}{(3810)^2} = 1.4 \times 10^7 \text{ N}$$ Euler buckling load in the plane of the applied bending moment adjusted for shear deformation is given by $$P_{E,v} = \frac{P_E}{1+\frac{\kappa P_E}{(GA)_{eff}}} = \frac{1.4\times10^7}{1+\frac{1\times1.4\times10^7}{2.32\times10^9}} = 1.39 \times 10^7 \text{ N}$$ $$\frac{6440}{9683} + \frac{242}{1224}\left[\frac{1}{1-\frac{6440}{1.39\times10^7}}\right] = 0.86 < 1.0$$
Final thickness:
Finally, **245 mm** of thickness of CLT core wall is provided in X direction.
Design for CLT walls in Y-direction:
Cross-section details:
Consider, 5 layers of CLT of each panel thickness of 35 mm (i.e. 3 longitudinal layers and 2 transverse layers) Total thickness of wall (h) = 5 × 35 = 175 mm The effective bending stiffness of the panel for the major axis strength axis is given by $$(EI)_{eff,y} = \sum_{i=1}^{n} E_i \cdot b_y \cdot \frac{t_i^3}{12} + \sum_{i=1}^{n} E_i \cdot b_y \cdot t_i \cdot z_i^2 = 60.54 \times 10^{12} \text{N-mm}^2$$
Design against compressive loads:
The effective thickness, effective cross-sectional area and the effective out-of-plane moment of inertia are obtained as, $h_{eff}(=\sum_{i=1}^{(n+1)/2} t_{2n-1})$: $3 \times 35 = 105$ mm $A_{eff}(= b \cdot h_{eff})$: $14630.4 \times 105 = 1536192$ mm^2 $I_{eff,y}(=\frac{b_y h_{eff}^3}{3})$: $\frac{14630.4\times105^3}{12} = 1.41 \times 10^9$ mm^4 The effective radius of gyration, r_{eff} is given by $$r_{eff} = \sqrt{\frac{I_{eff}}{A_{eff}}} = \sqrt{\frac{1.41\times10^9}{1536192}} = 30$$ The slenderness ratio (C_c), the size factor for compression (K_{zc}), the slenderness factor for compression K_c are estimated as $$C_c = \frac{L_e}{\sqrt{12} r_{eff}} = \frac{3810}{\sqrt{12}\times30} = 36.29 < 43$$ $$K_{zc} = 6.3\big(2\sqrt{3} r_{eff} L\big)^{-0.13} = 6.3\big(2\sqrt{3}\times 40 \times 3810\big)^{-0.13} = 1.18 < 1.3$$ $$K_c = \left[1 + \frac{F_c K_{zc} C_c^3}{35 E_{05} K_{SE} K_T}\right]^{-1} = \left[1 + \frac{f_c(K_D K_H K_{Sc} K_T) K_{zc} C_c^3}{35 E_{05} K_{SE} K_T}\right]^{-1} = \left[1 + \frac{19.3\times1\times1.18\times36.29^3}{35\times0.87\times11700\times1}\right]^{-1} = 0.25$$ Therefore, the factored compressive resistance is, $$P_r = \phi F_c A_{eff} K_{zc} K_c = 0.8 \times 19.3 \times 1536192 \times 1.18 \times 0.25 = 6900.60 \text{ kN} > 4885 \text{ kN}$$

Design against bending moment:
The section modulus in the major direction $S_{eff,y}$ is, $$S_{eff,y} = \frac{(EI)_{eff,y}}{E_1} \cdot \frac{2}{h} = \frac{81.29\times10^{12}}{11700} \times \frac{2}{175} = 5.91 \times 10^7 \text{ mm}^3$$ Therefore, the bending resistance is, $$M_{r,y} = \phi F_b S_{eff,y} K_{rb,y} = 0.9 \times 28.2 \times 5.91 \times 10^7 \times 0.85 = 1276 \text{ kN-m} > 169 \text{ kN-m}$$
Design against combination of axial and bending loads:
CLT panels subject to combined out-of-plane bending and compressive axial load shall be designed to satisfy the interaction equation which is given as $$\frac{P_f}{P_r} + \frac{M_f}{M_r}\left[\frac{1}{1-\frac{P_f}{P_{E,v}}}\right] \leq 1$$ The Euler buckling load is given by $$P_E = \frac{\pi^2 E_{05} I_{eff}}{(K_e L)^2} = \frac{\pi^2\times0.87\times11700\times3.35\times10^9}{(3810)^2} = 1.37 \times 10^7 \text{ N}$$ Euler buckling load in the plane of the applied bending moment adjusted for shear deformation is given by $$P_{E,v} = \frac{P_E}{1+\frac{\kappa P_E}{(GA)_{eff}}} = \frac{1.37\times10^7}{1+\frac{1\times1.37\times10^7}{3.83\times10^9}} = 1.36 \times 10^7 \text{ N}$$ $$\frac{4885}{6900.60} + \frac{169}{1276}\left[\frac{1}{1-\frac{4885}{1.36\times10^7}}\right] = 0.84 < 1.0$$
Final thickness:
Finally, **175 mm** of thickness of CLT core wall is provided in Y direction.

Appendix B

MATLAB - ETABS Interaction Code

```
clc;
clear all;
%% This code calculates the natural frequency of the outrigger system where different models are created for different locations of outrigger
%% Full path to the model (Change as per directory in system where model is saved)
ModelDirectory = 'C:\Users\Sourav\Desktop\Tall Structure Etabs';

for ii = 1 : 20 %% 1 : 20 represents outrigger location from 1-st to 20-th storey
    ii
    SysMat.IND    = ii;
    [omega] = Call_ETABS(ModelDirectory,SysMat);
    Omega(ii,:) = omega;
end
figure
plot(1:1:20, Omega)
```

%%

The above code is the main file where a function file is called 'Call ETABS.m' for different locations of outriggers. The function file is given below. %%

```
function [omega] = Call_ETABS(ModelDirectory,SysMat)

IND = SysMat.IND;
```

```
AttachToInstance = false();
SpecifyPath = false();
%% Specify the path where ETABS is installed
ProgramPath = 'C:\Program Files\Computers and Structures....
              \ETABS 18\ETABS.exe';
APIDLLPath = 'C:\Program Files\Computers and Structures.....
             \ETABS 18\ETABSv1.dll';

%% Call the models
if IND == 1
    ModelName = '1_Outrigger.EDB';
    ModelPath = strcat(ModelDirectory, filesep, ModelName);

elseif IND == 2
    ModelName = '2_Outrigger.EDB';
    ModelPath = strcat(ModelDirectory, filesep, ModelName);

elseif IND == 3
    ModelName = '3_Outrigger.EDB';
    ModelPath = strcat(ModelDirectory, filesep, ModelName);

elseif IND == 4
    ModelName = '4_Outrigger.EDB';
    ModelPath = strcat(ModelDirectory, filesep, ModelName);

elseif IND == 5
    ModelName = '5_Outrigger.EDB';
    ModelPath = strcat(ModelDirectory, filesep, ModelName);

elseif IND == 6
    ModelName = '6_Outrigger.EDB';
    ModelPath = strcat(ModelDirectory, filesep, ModelName);

elseif IND == 7
```

```
    ModelName = '7_Outrigger.EDB';
    ModelPath = strcat(ModelDirectory, filesep, ModelName);

elseif IND == 8
    ModelName = '8_Outrigger.EDB';
    ModelPath = strcat(ModelDirectory, filesep, ModelName);

elseif IND == 9
    ModelName = '9_Outrigger.EDB';
    ModelPath = strcat(ModelDirectory, filesep, ModelName);

elseif IND == 10
    ModelName = '10_Outrigger.EDB';
    ModelPath = strcat(ModelDirectory, filesep, ModelName);

elseif IND == 11
    ModelName = '11_Outrigger.EDB';
    ModelPath = strcat(ModelDirectory, filesep, ModelName);

elseif IND == 12
    ModelName = '12_Outrigger.EDB';
    ModelPath = strcat(ModelDirectory, filesep, ModelName);

elseif IND == 13
    ModelName = '13_Outrigger.EDB';
    ModelPath = strcat(ModelDirectory, filesep, ModelName);

elseif IND == 14
    ModelName = '14_Outrigger.EDB';
    ModelPath = strcat(ModelDirectory, filesep, ModelName);

elseif IND == 15
    ModelName = '15_Outrigger.EDB';
    ModelPath = strcat(ModelDirectory, filesep, ModelName);
```

```
elseif IND == 16
    ModelName = '16_Outrigger.EDB';
    ModelPath = strcat(ModelDirectory, filesep, ModelName);

elseif IND == 17
    ModelName = '17_Outrigger.EDB';
    ModelPath = strcat(ModelDirectory, filesep, ModelName);

elseif IND == 18
    ModelName = '18_Outrigger.EDB';
    ModelPath = strcat(ModelDirectory, filesep, ModelName);

elseif IND == 19
    ModelName = '19_Outrigger.EDB';
    ModelPath = strcat(ModelDirectory, filesep, ModelName);

elseif IND == 20
    ModelName = '20_Outrigger.EDB';
    ModelPath = strcat(ModelDirectory, filesep, ModelName);
end

%% Create API helper object
a = NET.addAssembly(APIDLLPath);
helper = ETABSv1.Helper;
helper = NET.explicitCast(helper,'ETABSv1.cHelper');

if AttachToInstance
        %% Attach to a running instance of ETABS
        ETABSObject = helper.GetObject('CSI.ETABS.API.ETABSObject');
        ETABSObject = NET.explicitCast(ETABSObject,'ETABSv1.cOAPI');
else
  if SpecifyPath
  %% Create an instance of the ETABS object from the specified path
  ETABSObject = helper.CreateObject(ProgramPath);
```

```
  else
  %% Create an instance of ETABS object from latest installed ETABS
  ETABSObject = helper.CreateObjectProgID('CSI.ETABS.API.ETABSObject');
  end
  ETABSObject = NET.explicitCast(ETABSObject,'ETABSv1.cOAPI');

   %% Start ETABS application
   ETABSObject.ApplicationStart;
end
helper = 0;

%% Create SapModel object
SapModel = NET.explicitCast(ETABSObject.SapModel,'ETABSv1.cSapModel');

%% Initialize model
ret = SapModel.InitializeNewModel;

%% Create new blank model
File = NET.explicitCast(SapModel.File,'ETABSv1.cFile');
ret =  File.OpenFile(ModelPath);

%% Run the ETABS model
Analyze = NET.explicitCast(SapModel.Analyze,'ETABSv1.cAnalyze');
ret = Analyze.RunAnalysis();

%% Exract the results

if IND == 1
    [AA]  = fopen('1_Outrigger.LOG');
    Fr1   = fread(AA);
    s     = char(Fr1');
    fclose(AA);

elseif IND == 2
```

```
    [AA]   = fopen('2_Outrigger.LOG');
    Fr1    = fread(AA);
    s      = char(Fr1');
    fclose(AA);

elseif IND == 3
    [AA]   = fopen('3_Outrigger.LOG');
    Fr1    = fread(AA);
    s      = char(Fr1');
    fclose(AA);

elseif IND == 4
    [AA]   = fopen('4_Outrigger.LOG');
    Fr1    = fread(AA);
    s      = char(Fr1');
    fclose(AA);

elseif IND == 5
    [AA]   = fopen('5_Outrigger.LOG');
    Fr1    = fread(AA);
    s      = char(Fr1');
    fclose(AA);

elseif IND == 6
    [AA]   = fopen('6_Outrigger.LOG');
    Fr1    = fread(AA);
    s      = char(Fr1');
    fclose(AA);

elseif IND == 7
    [AA]   = fopen('7_Outrigger.LOG');
    Fr1    = fread(AA);
    s      = char(Fr1');
    fclose(AA);
```

```
elseif IND == 8
    [AA]    = fopen('8_Outrigger.LOG');
    Fr1     = fread(AA);
    s       = char(Fr1');
    fclose(AA);

elseif IND == 9
    [AA]    = fopen('9_Outrigger.LOG');
    Fr1     = fread(AA);
    s       = char(Fr1');
    fclose(AA);

elseif IND == 10
    [AA]    = fopen('10_Outrigger.LOG');
    Fr1     = fread(AA);
    s       = char(Fr1');
    fclose(AA);

elseif IND == 11
    [AA]    = fopen('11_Outrigger.LOG');
    Fr1     = fread(AA);
    s       = char(Fr1');
    fclose(AA);

elseif IND == 12
    [AA]    = fopen('12_Outrigger.LOG');
    Fr1     = fread(AA);
    s       = char(Fr1');
    fclose(AA);

elseif IND == 13
    [AA]    = fopen('13_Outrigger.LOG');
    Fr1     = fread(AA);
```

```
    s       = char(Fr1');
    fclose(AA);

elseif IND == 14
    [AA]    = fopen('14_Outrigger.LOG');
    Fr1     = fread(AA);
    s       = char(Fr1');
    fclose(AA);

elseif IND == 15
    [AA]    = fopen('15_Outrigger.LOG');
    Fr1     = fread(AA);
    s       = char(Fr1');
    fclose(AA);

elseif IND == 16
    [AA]    = fopen('16_Outrigger.LOG');
    Fr1     = fread(AA);
    s       = char(Fr1');
    fclose(AA);

elseif IND == 17
    [AA]    = fopen('17_Outrigger.LOG');
    Fr1     = fread(AA);
    s       = char(Fr1');
    fclose(AA);

elseif IND == 18
    [AA]    = fopen('18_Outrigger.LOG');
    Fr1     = fread(AA);
    s       = char(Fr1');
    fclose(AA);

elseif IND == 19
```

```
    [AA]    = fopen('19_Outrigger.LOG');
    Fr1     = fread(AA);
    s       = char(Fr1');
    fclose(AA);

elseif IND == 20
    [AA]    = fopen('20_Outrigger.LOG');
    Fr1     = fread(AA);
    s       = char(Fr1');
    fclose(AA);
end

word1Location = strfind(s, 'NUMBER OF EIGEN MODES FOUND');
word2Location = strfind(s, 'NUMBER OF ITERATIONS PERFORMED');
TextLine      = s(word1Location:word2Location-1);
Number_Modes  = str2double(TextLine(54:end));
Frq = zeros(Number_Modes-1,1);

for ii = 1:Number_Modes-1
    if ii == Number_Modes
    word1Location = strfind(s, ['Found mode ' num2str(ii)]);
    word2Location = strfind(s, 'NUMBER OF EIGEN MODES FOUND');
    elseif ii < 9
    word1Location = strfind(s, ['Found mode ' num2str(ii)]);
    word2Location = strfind(s, ['Found mode ' num2str(ii+1)]);
    elseif ii == 9
    word1Location = strfind(s, ['Found mode ' num2str(ii)]);
    word2Location = strfind(s, ['Found mode ' num2str(ii+1)]);
    elseif (ii>9) && (ii~=Number_Modes)
    word1Location = strfind(s, ['Found mode ' num2str(ii)]);
    word2Location = strfind(s, ['Found mode ' num2str(ii+1)]);
    end
    Mode = s(word1Location:word2Location-1);
    word1Location = strfind(Mode, 'f=');
```

```
    word2Location = strfind(Mode, ', T= ');
    Fre  = Mode(word1Location:word2Location-1);
    Freq = str2double(Fre(3:14));
    Frq(ii,:) = Freq;
end
omega = 2*pi.*Frq;
%% Save model File.OpenFile
File.Save([ModelPath,'.EDB']);
%% Close ETABS Model
ETABSObject.ApplicationExit(false());
end
```

References

Aghlara, R. and Tahir, M. M. (2018). A passive metallic damper with replaceable steel bar components for earthquake protection of structures. *Engineering Structures*, 159:185–197.

Al-Saif, K. A., Aldakkan, K. A., and Foda, M. A. (2011). Modified liquid column damper for vibration control of structures. *International Journal of Mechanical Sciences*, 53(7):505–512.

Alhan, C. and Gavin, H. (2004). A parametric study of linear and non-linear passively damped seismic isolation systems for buildings. *Engineering Structures*, 26(4):485–497.

Araki, Y., Shrestha, K. C., Maekawa, N., Koetaka, Y., Omori, T., and Kainuma, R. (2016). Shaking table tests of steel frame with superelastic Cu–Al–Mn SMA tension braces. *Earthquake Engineering & Structural Dynamics*, 45(2):297–314.

Asai, T., Chang, C.-M., Phillips, B. M., and Spencer Jr, B. F. (2013). Real-time hybrid simulation of a smart outrigger damping system for high-rise buildings. *Engineering Structures*, 57:177–188.

Asai, T. and Watanabe, Y. (2017). Outrigger tuned inertial mass electromagnetic transducers for high-rise buildings subject to long period earthquakes. *Engineering Structures*, 153:404–410.

Atkinson, G. M. and Goda, K. (2011). Effects of seismicity models and new ground-motion prediction equations on seismic hazard assessment for four Canadian cities. *Bulletin of the Seismological Society of America*, 101(1):176–189.

Balendra, T., Wang, C. M., and Cheong, H. F. (1995). Effectiveness of tuned liquid column dampers for vibration control of towers. *Engineering Structures*, 17(9):668–675.

Bezabeh, M. A., Bitsuamlak, G. T., and Tesfamariam, S. (2021a). Nonlinear dynamic response of single-degree-of-freedom systems subjected to along-wind loads. I: Parametric study. *Journal of Structural Engineering*, 147(11):04021177.

Bezabeh, M. A., Bitsuamlak, G. T., and Tesfamariam, S. (2021b). Nonlinear dynamic response of single-degree-of-freedom systems subjected to along-wind loads. II: Implications for structural reliability. *Journal of Structural Engineering*, 147(11):04021178.

Boellaard, B. (2012). Design of an Outrigger Structure for Tall Timber Buildings. Master's thesis, Eindhoven University of Technology, Eindhoven, the Netherlands.

Chakraborty, S. and Roy, B. K. (2011). Reliability based optimum design of tuned mass damper in seismic vibration control of structures with bounded uncertain parameters. *Probabilistic Engineering Mechanics*, 26(2):215–221.

Chang, C. C. and Gu, M. (1999). Suppression of vortex-excited vibration of tall buildings using tuned liquid dampers. *Journal of Wind Engineering and Industrial Aerodynamics*, 83(1-3):225–237.

Chang, C.-M., Wang, Z., Spencer Jr, B. F., and Chen, Z. (2013). Semi-active damped outriggers for seismic protection of high-rise buildings. *Smart Structures and Systems*, 11(5):435–451.

Chen, J.-L. and Georgakis, C. T. (2015). Spherical tuned liquid damper for vibration control in wind turbines. *Journal of Vibration and Control*, 21(10):1875–1885.

Chen, Y., McFarland, D. M., Wang, Z., Spencer Jr, B. F., and Bergman, L. A. (2010). Analysis of tall buildings with damped outriggers. *Journal of Structural Engineering*, 136(11):1435–1443.

Cho, S.-W., Jung, H.-J., and Lee, I.-W. (2005). Smart passive system based on magnetorheological damper. *Smart Materials and Structures*, 14(4):707.

Christopoulos, C. and Montgomery, M. (2013). Viscoelastic coupling dampers (VCDs) for enhanced wind and seismic performance of high-rise buildings. *Earthquake Engineering & Structural Dynamics*, 42(15):2217–2233.

CSA (2014). *CSA O86-14: Engineering Design in Wood*. Canadian Standards Association, Mississauga, Canada.

Dao, N. D., Nguyen-Van, H., Nguyen, T. H., and Chung, A. B. (2020). A new statistical equation for predicting nonlinear time history displacement of seismic isolation systems. *Structures*, 24:177–190.

Das, S. and Choudhury, S. (2017). Seismic response control by tuned liquid dampers for low-rise RC frame buildings. *Australian Journal of Structural Engineering*, 18(2):135–145.

Das, S., Sajeer, M. M., and Chakraborty, A. (2019). Vibration control of horizontal axis offshore wind turbine blade using SMA stiffener. *Smart Materials and Structures*, 28(9):095025.

Das, S. and Tesfamariam, S. (2020). Optimization of SMA based damped outrigger structure under uncertainty. *Engineering Structures*, 222:111074.

Das, S., Chakraborty, S., Chen, Y., and Tesfamariam, S. (2020). Robust design optimization for SMA based nonlinear energy sink with negative stiffness and friction. *Soil Dynamics and Earthquake Engineering*, 140:106466.

Das, S., Chakraborty, S., Chen, Y., and Tesfamariam, S. (2021). Robust design optimization for SMA based nonlinear energy sink with negative stiffness and friction. *Soil Dynamics and Earthquake Engineering*, 140:106466.

De Domenico, D., Deastra, P., Ricciardi, G., Sims, N. D., and Wagg, D. J. (2019). Novel fluid inerter based tuned mass dampers for optimised structural control of base-isolated buildings. *Journal of the Franklin Institute*, 356(14):7626–7649.

Deb, K., Pratap, A., Agarwal, S., and Meyarivan, T. (2002). A fast and elitist multiobjective genetic algorithm: NSGA-II. *IEEE Transactions on Evolutionary Computation*, 6(2):182–197.

Deng, K., Pan, P., Lam, A., and Xue, Y. (2014). A simplified model for analysis of high-rise buildings equipped with hysteresis damped outriggers. *The Structural Design of Tall and Special Buildings*, 23(15):1158–1170.

Dolce, M., Cardone, D., and Marnetto, R. (2000). Implementation and testing of passive control devices based on shape memory alloys. *Earthquake Engineering & Structural Dynamics*, 29(7):945–968.

Eatherton, M. R., Fahnestock, L. A., and Miller, D. J. (2014). Computational study of self-centering buckling-restrained braced frame seismic performance. *Earthquake Engineering & Structural Dynamics*, 43(13):1897–1914.

Ebrahimi, B., Khamesee, M. B., and Golnaraghi, F. (2009). A novel eddy current damper: theory and experiment. *Journal of Physics D: Applied Physics*, 42(7):075001.

Fan, F.-G., Ahmadi, G., Mostaghel, N., and Tadjbakhsh, I. G. (1991). Performance analysis of aseismic base isolation systems for a multi-story building. *Soil Dynamics and Earthquake Engineering*, 10(3):152–171.

Fang, C. J., Tan, P., Chang, C. M., and Zhou, F. L. (2015). A general solution for performance evaluation of a tall building with multiple damped and undamped outriggers. *The Structural Design of Tall and Special Buildings*, 24(12):797–820.

Fediw, A. A., Isyumov, N., and Vickery, B. J. (1995). Performance of a tuned sloshing water damper. *Journal of Wind Engineering and Industrial Aerodynamics*, 57(2-3):237–247.

Fujii, K., Tamura, Y., Sato, T., and Wakahara, T. (1990). Wind-induced vibration of tower and practical applications of tuned sloshing damper. *Journal of Wind Engineering and Industrial Aerodynamics*, 33(1-2):263–272.

Fujino, Y., Sun, L., Pacheco, B. M., and Chaiseri, P. (1992). Tuned liquid damper (TLD) for suppressing horizontal motion of structures. *Journal of Engineering Mechanics*, 118(10):2017–2030.

Gao, H., Kwok, K. C. S., and Samali, B. (1997). Optimization of tuned liquid column dampers. *Engineering Structures*, 19(6):476–486.

Garrido, H., Curadelli, O., and Ambrosini, D. (2019). Resettable-inertance inerter: A semiactive control device for energy absorption. *Structural Control and Health Monitoring*, 26(11):e2415.

Ghodke, S. and Jangid, R. S. (2016). Equivalent linear elastic-viscous model of shape memory alloy for isolated structures. *Advances in Engineering Software*, 99:1–8.

Goda, K. (2019). Nationwide earthquake risk model for wood-frame houses in canada. *Frontiers in Built Environment*, 5:128.

Graesser, E. J. and Cozzarelli, F. A. (1991). Shape-memory alloys as new materials for aseismic isolation. *Journal of Engineering Mechanics*, 117(11):2590–2608.

Graesser, E. J. and Cozzarelli, F. A. (1994). A proposed three-dimensional constitutive model for shape memory alloys. *Journal of Intelligent Material Systems and Structures*, 5(1):78–89.

Guo, S., Yang, S., and Pan, C. (2006). Dynamic modeling of magnetorheological damper behaviors. *Journal of Intelligent Material Systems and Structures*, 17(1):3–14.

Gur, S., Roy, K., and Mishra, S. K. (2015). Tuned liquid column ball damper for seismic vibration control. *Structural Control and Health Monitoring*, 22(11):1325–1342.

Halchuk, S., Allen, T. I., Adams, J., and Rogers, G. C. (2014). Fifth Generation Seismic Hazard Model Input Files as Proposed to Produce Values for the 2015 National Building Code of Canada. Technical report, Geological Survey of Canada Open File.

Han, Y.-L., Li, Q. S., Li, A.-Q., Leung, A. Y. T., and Lin, P.-H. (2003). Structural vibration control by shape memory alloy damper. *Earthquake Engineering & Structural Dynamics*, 32(3):483–494.

Hejazi, F., Shoaei, M. D., Tousi, A., and Jaafar, M. S. (2016). Analytical model for viscous wall dampers. *Computer-Aided Civil and Infrastructure Engineering*, 31(5):381–399.

Hoang, N., Fujino, Y., and Warnitchai, P. (2008). Optimal tuned mass damper for seismic applications and practical design formulas. *Engineering Structures*, 30(3):707–715.

Hoenderkamp, J. C. D. (2008). Second outrigger at optimum location on high-rise shear wall. *The structural Design of Tall and Special Buildings*, 17(3):619–634.

Huang, H. and Chang, W.-S. (2018). Application of pre-stressed SMA-based tuned mass damper to a timber floor system. *Engineering Structures*, 167:143–150.

Ikeda, Y. (2009). Active and semi-active vibration control of buildings in Japan—Practical applications and verification. *Structural Control and Health Monitoring*, 16(7-8):703–723.

Jangid, R. S. and Kelly, J. M. (2001). Base isolation for near-fault motions. *Earthquake Engineering & Structural Dynamics*, 30(5):691–707.

Jangid, R. S. (2010). Stochastic response of building frames isolated by lead–rubber bearings. *Structural Control and Health Monitoring*, 17(1):1–22.

Javidialesaadi, A. and Wierschem, N. E. (2019). An inerter-enhanced nonlinear energy sink. *Mechanical Systems and Signal Processing*, 129:449–454.

Jia, Y., Li, L., Wang, C., Lu, Z., and Zhang, R. (2019). A novel shape memory alloy damping inerter for vibration mitigation. *Smart Materials and Structures*, 28(11):115002.

Karacabeyli, E. and Gagnon, S. (2019). *Canadian CLT Handbook, 2019 Edition*. FPInnovations, Pointe-Claire, QC, Canada.

Kaynia, A. M., Veneziano, D., and Biggs, J. M. (1981). Seismic effectiveness of tuned mass dampers. *Journal of the Structural Division*, 107(8):1465–1484.

Khaloo, A., Maghsoudi-Barmi, A., and Moeini, M. E. (2020). Numerical parametric investigation of hysteretic behavior of steel-reinforced elastomeric bearings under large shear deformation. *Structures*, 26:456–470.

Kim, H.-S. and Kang, J.-W. (2017). Smart outrigger damper system for response reduction of tall buildings subjected to wind and seismic excitations. *International Journal of Steel Structures*, 17(4):1263–1272.

Konar, T. and Ghosh, A. D. (2021). Flow damping devices in tuned liquid damper for structural vibration control: A review. *Archives of Computational Methods in Engineering*, 28:2195–2207.

Kourakis, I. (2007). Structural Systems and Tuned Mass Dampers of Super-Tall Buildings: Case Study of Taipei 101. Master's thesis, Massachusetts Institute of Technology.

Lago, A., Trabucco, D., and Wood, A. (2018). *Damping Technologies for Tall Buildings: Theory, Design Guidance and Case Studies*. Butterworth-Heinemann.

Lee, D. and Taylor, D. P. (2001). Viscous damper development and future trends. *The Structural Design of Tall Buildings*, 10(5):311–320.

Lee, J., Bang, M., and Kim, J.-Y. (2008). An analytical model for high-rise wall-frame structures with outriggers. *The Structural Design of Tall and Special Buildings*, 17(4):839–851.

Li, C., Liang, M., Wang, Y., and Dong, Y. (2012a). Vibration suppression using two-terminal flywheel. Part I: Modeling and characterization. *Journal of Vibration and Control*, 18(8):1096–1105.

Li, C., Liang, M., Wang, Y., and Dong, Y. (2012b). Vibration suppression using two-terminal flywheel. Part II: application to vehicle passive suspension. *Journal of Vibration and Control*, 18(9):1353–1365.

Li, C., Chang, K., Cao, L., and Huang, Y. (2021). Performance of a nonlinear hybrid base isolation system under the ground motions. *Soil Dynamics and Earthquake Engineering*, 143:106589.

Li, H., Mao, C.-X., and Ou, J.-P. (2008). Experimental and theoretical study on two types of shape memory alloy devices. *Earthquake Engineering & Structural Dynamics*, 37(3):407–426.

Li, H.-N., Yi, T.-H., Jing, Q.-Y., Huo, L.-S., and Wang, G.-X. (2012c). Wind-induced vibration control of Dalian International Trade Mansion by tuned liquid dampers. *Mathematical Problems in Engineering*, 2012:1–21.

Lian, J., Zhao, Y., Lian, C., Wang, H., Dong, X., Jiang, Q., Zhou, H., and Jiang, J. (2018). Application of an eddy current-tuned mass damper to vibration mitigation of offshore wind turbines. *Energies*, 11(12):3319.

Lin, P.-C., Takeuchi, T., and Matsui, R. (2018). Seismic performance evaluation of single damped-outrigger system incorporating buckling-restrained braces. *Earthquake Engineering & Structural Dynamics*, 47(12):2343–2365.

Lin, P.-C., Takeuchi, T., and Matsui, R. (2019). Optimal design of multiple damped-outrigger system incorporating buckling-restrained braces. *Engineering Structures*, 194:441–457.

Lin, P. Y., Roschke, P. N., and Loh, C. H. (2007). Hybrid base-isolation with magnetorheological damper and fuzzy control. *Structural Control and Health Monitoring*, 14(3):384–405.

Liu, M., Zhou, P., and Li, H. (2018). Novel self-centering negative stiffness damper based on combination of shape memory alloy and prepressed springs. *Journal of Aerospace Engineering*, 31(6):04018100.

Liu, W. and Lui, E. M. (2020). Mathematical modeling and parametric study of magnetic negative stiffness dampers. *Advances in Structural Engineering*, 23(8):1702–1714.

Lu, X., Zhou, Y., and Yan, F. (2008). Shaking table test and numerical analysis of rc frames with viscous wall dampers. *Journal of Structural Engineering*, 134(1):64–76.

Lu, X., Liao, W., Cui, Y., Jiang, Q., and Zhu, Y. (2019). Development of a novel sacrificial-energy dissipation outrigger system for tall buildings. *Earthquake Engineering & Structural Dynamics*, 48(15):1661–1677.

Malekinejad, M. and Rahgozar, R. (2013). An analytical approach to free vibration analysis of multi-outrigger–belt truss-reinforced tall buildings. *The Structural Design of Tall and Special Buildings*, 22(4):382–398.

Matsagar, V. A. and Jangid, R. S. (2004). Influence of isolator characteristics on the response of base-isolated structures. *Engineering Structures*, 26(12):1735–1749.

Meirovitch, L. (1980). *Computational Methods in Structural Dynamics*, volume 5. Springer Science & Business Media.

Mirafzal, S. H., Khorasani, A. M., and Ghasemi, A. H. (2016). Optimizing time delay feedback for active vibration control of a cantilever beam using a genetic algorithm. *Journal of Vibration and Control*, 22(19):4047–4061.

Moehle, J. B., Jayaram, Y., Jones, N., Rahnama, P., Shome, M., Tuna, N., Wallace, Z., and Yang, J. (2011). Case studies of the seismic performance of tall buildings designed by alternative means: Task 12 report for the tall buildings initiative. Technical report, PEER Report.

Morales-Beltran, M., Turan, G., Yildirim, U., and Paul, J. (2018). Distribution of strong earthquake input energy in tall buildings equipped with damped outriggers. *The Structural Design of Tall and Special Buildings*, 27(8):e1463.

Mualla, I. H. and Belev, B. (2002). Performance of steel frames with a new friction damper device under earthquake excitation. *Engineering Structures*, 24(3):365–371.

NBC (2015). *National Building Code of Canada, 2015*. National Research Council Canada, Ottawa, Canada.

Ozbulut, O. E. and Hurlebaus, S. (2011). Optimal design of superelastic-friction base isolators for seismic protection of highway bridges against near-field earthquakes. *Earthquake Engineering & Structural Dynamics*, 40(3):273–291.

Ozbulut, O. E. and Hurlebaus, S. (2012). Application of an SMA-based hybrid control device to 20-story nonlinear benchmark building. *Earthquake Engineering & Structural Dynamics*, 41(13):1831–1843.

Pant, D. R., Montgomery, M., and Christopoulos, C. (2019). Full-scale testing of a viscoelastic coupling damper for high-rise building applications and comparative evaluation of different numerical models. *Journal of Structural Engineering*, 145(2):04018242.

Papageorgiou, C., Houghton, N. E., and Smith, M. C. (2009). Experimental testing and analysis of inerter devices. *Journal of Dynamic Systems, Measurement, and Control*, 131(1):011001.

Piersol, A. G. and Paez, T. L. (2010). *Harris' Shock and Vibration Handbook*. Mcgraw-Hill.

Popovski, M. and Gavric, I. (2016). Performance of a 2-story CLT house subjected to lateral loads. *Journal of Structural Engineering*, 142(4):E4015006.

Qiu, C. and Zhu, S. (2017). Shake table test and numerical study of self-centering steel frame with SMA braces. *Earthquake Engineering & Structural Dynamics*, 46(1):117–137.

Ramage, M., Foster, R., Smith, S., Flanagan, K., and Bakker, R. (2017). Super tall timber: Design research for the next generation of natural structure. *The Journal of Architecture*, 22(1):104–122.

Saito, T., Shiba, K., and Tamura, K. (2001). Vibration control characteristics of a hybrid mass damper system installed in tall buildings. *Earthquake Engineering & Structural Dynamics*, 30(11):1677–1696.

Shankar, K. and Balendra, T. (2002). Application of the energy flow method to vibration control of buildings with multiple tuned liquid dampers. *Journal of Wind Engineering and Industrial Aerodynamics*, 90(12-15):1893–1906.

Shi, X. and Zhu, S. (2015). Magnetic negative stiffness dampers. *Smart Materials and Structures*, 24(7):072002.

Sinou, J. J. and Chomette, B. (2021). Active vibration control and stability analysis of a time-delay system subjected to friction-induced vibration. *Journal of Sound and Vibration*, 500:116013.

Smith, M. C. (2002). Synthesis of mechanical networks: the inerter. *IEEE Transactions on automatic control*, 47(10):1648–1662.

Smith, R. J. and Willford, M. R. (2007). The damped outrigger concept for tall buildings. *The Structural Design of Tall and Special Buildings*, 16(4):501–517.

Smith, S. B. and Salim, I. (1981). Parameter study of outrigger-braced tall building structures. *Journal of the Structural Division*, 107(10):2001–2014.

Smith, S. B. and Salim, I. (1983). Formulae for optimum drift resistance of outrigger braced tall building structures. *Computers & Structures*, 17(1):45–50.

Smith, S. B. and Coull, A. (1991). *Tall Building Structures: Analysis and Design*. Wiley-Interscience.

Sodano, H. A., Bae, J.-S., Inman, D. J., and Belvin, W. K. (2005). Concept and model of eddy current damper for vibration suppression of a beam. *Journal of Sound and Vibration*, 288(4-5):1177–1196.

Sun, L. M., Fujino, Y., Pacheco, B. M., and Chaiseri, P. (1992). Modelling of tuned liquid damper (TLD). *Journal of Wind Engineering and Industrial Aerodynamics*, 43(1-3):1883–1894.

Tan, P., Fang, C., and Zhou, F. (2014). Dynamic characteristics of a novel damped outrigger system. *Earthquake Engineering and Engineering Vibration*, 13(2):293–304.

Tanaka, K., Nishimura, F., and Tobushi, H. (1995). Transformation start lines in TiNi and Fe-based shape memory alloys after incomplete transformations induced by mechanical and/or thermal loads. *Mechanics of Materials*, 19(4):271–280.

Taranath, B. S. (2016). *Structural Analysis and Design of Tall Buildings: Steel and Composite Construction*. CRC press.

Tesfamariam, S., Stiemer, S. F., Bezabeh, M., Goertz, C., Popovski, M., and Goda,

K. (2015). *Force Based Design Guideline for Timber-Steel Hybrid Structures: Steel Moment Resisting Frames with CLT Infill Walls*. UBC Faculty Research and Publications. http://dx.doi.org/10.14288/1.0223405.

Tesfamariam, S., Bezabeh, M., Skandalos, K., Martinez, E., Dires, S., Bitsuamlak, G., and Goda, K. (2019). *Wind and Earthquake Design Framework for Tall Wood-Concrete Hybrid System*. UBC Faculty Research and Publications. http://dx.doi.org/10.14288/1.0380777.

Tesfamariam, S., Skandalos, K., and Teweldebrhan, B. (2021a). *Design of Tall-Coupled-Wall Timber Building: Energy Dissipating Coupling Beams*. UBC Faculty Research and Publications. https://dx.doi.org/10.14288/1.0403817.

Tesfamariam, S., Skandalos, K., Goda, K., Bezabeh, M. A., Bitsuamlak, G., and Popovski, M. (2021b). Quantifying the ductility-related force modification factor for 10-Story timber–RC hybrid building using FEMA P695 procedure and considering the 2015 NBC seismic sazard. *Journal of Structural Engineering*, 147(5):04021052.

Tsai, C. S. and Lee, H. H. (1993). Applications of viscoelastic dampers to high-rise buildings. *Journal of Structural Engineering*, 119(4):1222–1233.

Tso, M. H., Yuan, J., and Wong, W. O. (2013). Design and experimental study of a hybrid vibration absorber for global vibration control. *Engineering Structures*, 56:1058–1069.

Wakahara, T., Ohyama, T., and Fujii, K. (1992). Suppression of wind-induced vibration of a tall building using tuned liquid damper. *Journal of Wind Engineering and Industrial Aerodynamics*, 43(1-3):1895–1906.

Wang, B. and Zhu, S. (2018). Superelastic SMA U-shaped dampers with self-centering functions. *Smart Materials and Structures*, 27(5):055003.

Wang, J. Y., Ni, Y. Q., Ko, J. M., and Spencer Jr, B. F. (2005). Magneto-rheological tuned liquid column dampers (MR-TLCDs) for vibration mitigation of tall buildings: modelling and analysis of open-loop control. *Computers & Structures*, 83(25-26):2023–2034.

Welt, F. and Modi, V. (1992a). Vibration damping through liquid sloshing, Part 1: A nonlinear analysis. *Journal of Vibration and Acoustics*, 114(1):10–16.

Welt, F. and Modi, V. (1992b). Vibration damping through liquid sloshing, Part 2: Experimental results. *Journal of Vibration and Acoustics*, 114(1):17–23.

Werner, F. and Richter, K. (2007). Wooden building products in comparative LCA. *The International Journal of Life Cycle Assessment*, 12(7):470–479.

Wu, J.-C., Shih, M.-H., Lin, Y.-Y., and Shen, Y.-C. (2005). Design guidelines for tuned liquid column damper for structures responding to wind. *Engineering Structures*, 27(13):1893–1905.

Xie, L., Ban, X., Xue, S., Ikago, K., Kang, J., and Tang, H. (2019). Theoretical study on a cable-bracing inerter system for seismic mitigation. *Applied Sciences*, 9(19):1–17.

Yalla, S. K. and Kareem, A. (2000). Optimum absorber parameters for tuned liquid column dampers. *Journal of Structural Engineering*, 126(8):906–915.

Yang, D.-H., Shin, J.-H., Lee, H., Kim, S.-K., and Kwak, M. K. (2017). Active vibration control of structure by active mass damper and multi-modal negative acceleration feedback control algorithm. *Journal of Sound and Vibration*, 392:18–30.

Zeidabadi, N. A., Mirtalae, K., and Mobasher, B. (2004). Optimized use of the outrigger system to stiffen the coupled shear walls in tall buildings. *The Structural Design of Tall and Special Buildings*, 13(1):9–27.

Zhao, Z., Chen, Q., Zhang, R., Pan, C., and Jiang, Y. (2019a). Optimal design of an inerter isolation system considering the soil condition. *Engineering Structures*, 196:109324.

Zhao, Z., Zhang, R., and Lu, Z. (2019b). A particle inerter system for structural seismic response mitigation. *Journal of the Franklin Institute*, 356(14):7669–7688.

Zhou, Y. and Li, H. (2014). Analysis of a high-rise steel structure with viscous damped outriggers. *The Structural Design of Tall and Special Buildings*, 23(13):963–979.

Zhou, Y., Zhang, C., and Lu, X. (2017). Seismic performance of a damping outrigger system for tall buildings. *Structural Control and Health Monitoring*, 24(1):e1864.

Zhu, Y. L. (1995). Inner force analysis of frame–core structure with horizontal outrigger belts. *Journal of Building Structures*, 10(1995):10–15.